LIMITATIONS OF REYNOLDS AVERAGING IN FORCED SKEWED TURBULENT MIXING LAYER

by

Atsushi Yamauchi

A Thesis Submitted to the Faculty of the

DEPARTMENT OF AEROSPACE AND MECHANICAL ENGINEERING

In Partial Fulfillment of the Requirements

For the Degree of

MASTER OF SCIENCE

In the Graduate College

THE UNIVERSITY OF ARIZONA

2019

THE UNIVERSITY OF ARIZONA
GRADUATE COLLEGE

As members of the Master's Committee, we certify that we have read the thesis prepared by Atsushi Yamauchi, titled "Limitations of Reynolds Averaging in Forced Skewed Turbulent Mixing Layer" and recommend that it be accepted as fulfilling the dissertation requirement for the Master's Degree.

Dr. Israel Wygnanski — Date: 12/13/2019

Dr. Jesse Little — Date: 12/13/2019

Dr. Anatoli Tumin — Date: 12/13/2019

Final approval and acceptance of this thesis is contingent upon the candidate's submission of the final copies of the thesis to the Graduate College.

I hereby certify that I have read this thesis prepared under my direction and recommend that it be accepted as fulfilling the Master's requirement.

Dr. Israel Wygnanski — Date: 12/13/2019
Master's Thesis Committee Chair
Department of Aerospace and Mechanical Engineering

ACKNOWLEDGMENT

First and foremost, I would like to thank my research advisor, Dr. Israel Wygnanski, for his technical guidance and support. When I looked for my instructor two years ago, he kindly agreed to the request, and words cannot describe how grateful I am. I would like to thank Dr. Jesse Little and Dr. Anatoli Tumin for being on my committee. I also wish to thank Dr. Lutz Taubert for his advice on experimental design and measurement system. It is not too much to say that I have learned from him how to install the setup, how to acquire the experimental data, and how to process the data. I want to thank Dr. Emile Suehiro for working before I took over his project and helping me get introduced to the project when I had first joined the AeroLab. I would like to thank Harshad Kalyankar for advising me not only about research but also about the culture in Tucson to enrich my life. I would like to thank Stephen Tang for his dedication when checking my thesis. Without his support, I would not have been able to complete my thesis. I would like to thank Ashish Singh and Mark Agate for helping me start PIV acquisition. I would also like to acknowledge all other past and current members of the AeroLab and TFCL for assisting me through all the experiments and discussion. I would like to acknowledge the members of the AME machine shop, particularly Dale Drew and Joe Hartley, for machining components of the experimental setup such as a wing test model and a perforated metal sheet. I am also deeply grateful to the AME staff members, particularly Jini Kandyil and Dr. Cho Lik Chan, for assisting me every step of the way, especially for the initial master's degree program.

Lastly, I would like to thank my family for their continuous physical and mental support every day. I cannot stay in health without their supports.

TABLE OF CONTENTS

LIST OF FIGURES

NOMENCLATURE

Roman Letters

A = fliperon forcing amplitude

F = frequency of excitation

P_1 = energy extracted from mean

P_2 = mean random shear production

P_3 = energy transfer to random

R = dimensionless velocity ratio

Re = Reynolds number

St = Strouhal number

U = streamwise velocity component

U_1 = velocity of low speed stream

U_2 = velocity of high speed stream

V = vertical velocity component

x = streamwise coordinate

$x\text{-}x_{TE}$ = streamwise distance from the trailing edge

x_s = distance where the saturation occurs

y = vertical coordinate

z = spanwise coordinate

Greek Letters

α_i = spatial growth rate

δ = vorticity thickness

θ = momentum thickness

Λ = swept back angle

λ = wavelength of excitation

φ = phase of oscillation

ω = vorticity

Superscripts

‘ = total turbulent intensity

Subscripts

c = coherent fluctuating component

r = random fluctuating component

TE = trailing edge

ABSTRACT

An experimental investigation aimed at studying the three-dimensional character of a turbulent mixing layer created downstream of a swept-back wing that served as a splitter plate and a screen that reduced the velocity in the test section on the lower side of the wing has been undertaken. The sweptback of the wing and the screen was 45^{o}.The potential for the controllability of this flow was also evaluated by using spanwise uniform periodic excitation in order to assess the sensitivity of the flow to oblique imposed perturbations.

The previous experiment (Suehiro (2017)) using splitter plate with the trailing edge having a "Λ" shape showed the complicated pattern of interacting waves emanating from both sides of the "Λ" notch. In order to investigate only one-sided effect which is simpler because of the absence of these interferences, the skewed swept-back wing was used for this research. Mean velocities measured by an array of pitot tubes, instantaneous velocities measured by PIV, and the hotwire data for spectrum analysis were taken to analyze the mixing layer.

The velocity profiles with forcing frequency of 50Hz attained self-similarities whereas that with forcing frequency of 75Hz was distorted and they were not self-similar. Traditionally the center of the mixing layer is arbitrarily defined as the location where the velocity is the average of the two streams. Forcing the mixing layer at a frequency of 50Hz generated only minor distortions to the sinusoidal oscillation of the mixing layer center while forcing 75Hz distorted the center much more.

The mixing layer with forcing frequency of 75Hz where the amplitude of the oscillations was 1.5mm was too amplified. As a result of the excessive amplification, there were two regimes. The flow experienced those regimes in time and in space. That is why a single scale length scale such as the vorticity thickness or the momentum thickness cannot be used to scale width of the turbulent mixing layer at all times and locations.

1. INTRODUCTION

With the ever-growing proliferation of aerospace technology, researchers around the globe recognize the significance of understanding turbulent mixed layer flow that play a vital role to many engineering applications ranging from propulsions to aerodynamics. One such example is the application of turbulent mixing flow on the design of Chevron nozzles, whereby these saw-tooth designs on nozzle lips (shown in Figure 1.1(a)) reduce the amount of noise generated by aircraft turbofan engine. Such noise reduction is achieved as the saw-tooth ridges create a pair of counter-rotating vortices that encourage mixing between both hot jet from nozzle and cold air from turbofan. In addition, many fifth-generation fighter aircrafts are designed with stealth capabilities and reduced aerodynamic drag which require all of its weaponry be stored in an internal weapons bay. These weapons such as missiles will then be deployed with the bay doors open for less than a second and hydraulic arms would push the weapon clear of the aircraft. Unfortunately, when these bay doors open, an intense shear flow is created due to unsteady complex flow of air inside the weapon bay cavity that consequently lead to issues with deploying weapons from internal bay. In order to reduce the fighter's vulnerability to detection and enhance its aerodynamic performance, bay doors are designed with saw-toothed designs on both front and rear edges that remained flushed with the rest of the fuselage when bay doors are closed (shown in Figure 1.1(b)). Moreover, when bay doors are opened these saw-tooth petals assist in energy diffusion by creating vortices to further stabilize airflow inside the weapon bay cavity. This allows the fighter capable of deploying its internal weapons while performing dogfighting maneuvers. From the aforementioned examples, one can conclude that a thorough understanding of turbulent mixing layer flow has endless applications to many technological challenges faced in the field of aerospace engineering.

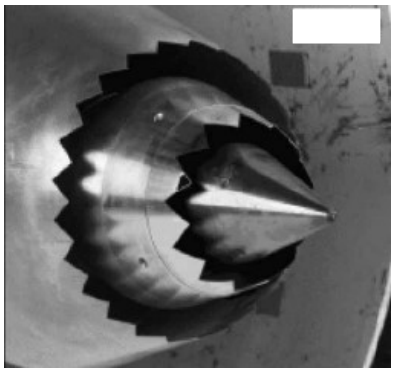

(a)

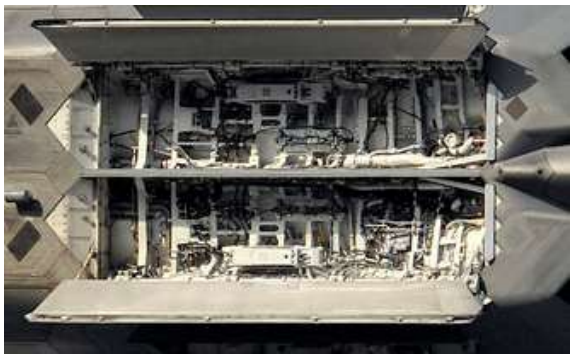

(b)

Figure 1. 1: Applications of the mixing layer (a) Chevron nozzles [1] (b) Weapon bay of F-22 (cavity flow) [2]

A mixing layer flow can be defined simply as the merging of two separate streams of fluid either with different velocities or densities respectively. Many experimental investigations focus on understanding three-dimensional shear flow to pave new advancements on aerodynamic designs. One such research focused on "Λ" notch design which serve as the fundamental block for Chevron nozzles. However, "Λ" notch has a unique geometrical feature its swept trailing edges in conjunction with the notch. Such feature leads to two oblique waves generated at the trailing edge which interact with each other in a nonlinear fashion. These nonlinear interaction effects are complex as the mixing layer generated by "Λ" notch contains a combination of both phase and antiphase oscillations. As such, it is difficult to implement any form of control mechanism on the "Λ" notch and leverage the stability characteristics of mixing layer flow for new aerospace applications. This leads to the focus of this research, which is to better understand and develop active control mechanisms that enable control of turbulent mixing layer flow for optimizing various aerospace designs. For this experimentation, a swept back wing was chosen as the fundamental block due to its geometrical simplicity and does not have complex nonlinear interactions to be considered unlike the "Λ" notch. In addition, spanwise periodic excitation will be used to introduce small perturbations at the origin of the flow through the addition of a flaperon on the trailing edge. By experimenting with various excitation frequencies and amplitudes, these results can expose the natural instabilities inherent within the flow configuration. Proper understanding of the turbulent mixing layer flow enables development of new aerodynamic control mechanisms.

2. BACKGROUND AND PRELIMINARY STUDIES

2.1 The plane mixing layer (two-dimensional unforced mixing layer)

When two streams of fluid flow over a solid surface with different densities or velocities and merge at the trailing edge, the resulting fluid phenomenon is called a mixing layer. Kelvin-Helmholtz instability influences the development of mean flow downstream, generating vortices downstream of the trailing edge of the flat plate. In the mixing layer, the momentum thickness, θ, was found to spread linearly at a rate depending on the velocity ratio between the two streams, U_1/U_2, as a function of streamwise distance. The spread rate of the plane mixing layer increases with the decreasing velocity ratio. This implies that the behavior of the perturbation is controlled solely by the velocities of the two streams (Figure 2.1).

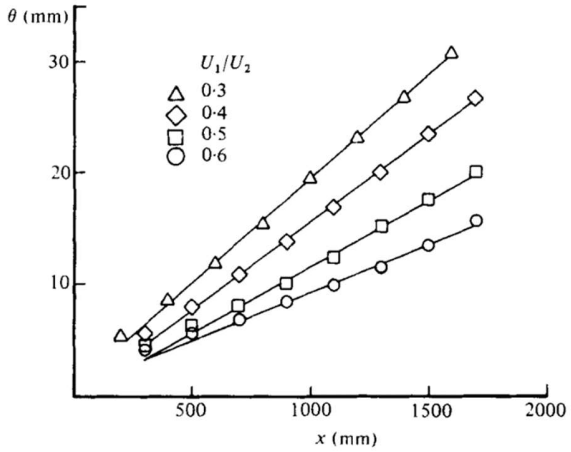

Figure 2.1: Momentum thickness for the unforced mixing layer [3]

In addition, both mean-velocity profiles and turbulent fluctuations of the mixing layer flow downstream indicate a self-preserving flow [3]. This further implies the flow achieves equilibrium and is independent of Reynolds number. The unique Re independence property is shown when all important parameters of the flow becomes similar when nondimensionalized by either a velocity or length scale. Traditionally, the velocity scale used in this research is simply the difference between both stream velocities, $U_2 - U_1$. Moreover, both local momentum thickness, θ and local vorticity thickness, δ_ω are suitable candidates as length scale. However, for analysis on the mixing layer close to trailing edge the vorticity thickness proves to be a better choice. This is due to the presence of a wake that dissipates further downstream.

$$\theta = \int_{-\infty}^{\infty} \frac{u - U_1}{U_2 - U_1}\left[1 - \frac{u - U_1}{U_2 - U_1}\right] dy \qquad 2.1$$

$$\delta_\omega = \frac{U_2 - U_1}{\left(\frac{\partial u}{\partial y}\right)_{max}} \qquad 2.2$$

Flow visualizations reveal [5] that structure of both higher and lower Reynolds number remained the same with smaller eddies present within the mixing layer as the only difference (Figure 2.2). This suggests that a large coherent structure dominates the flow within the mixing regardless of the Reynolds number. In other words, the structure within the mixing layer was governed by an inviscid process.

(a)

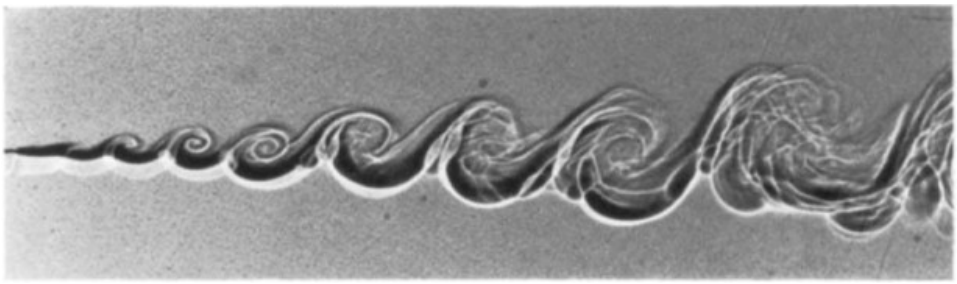

(b)

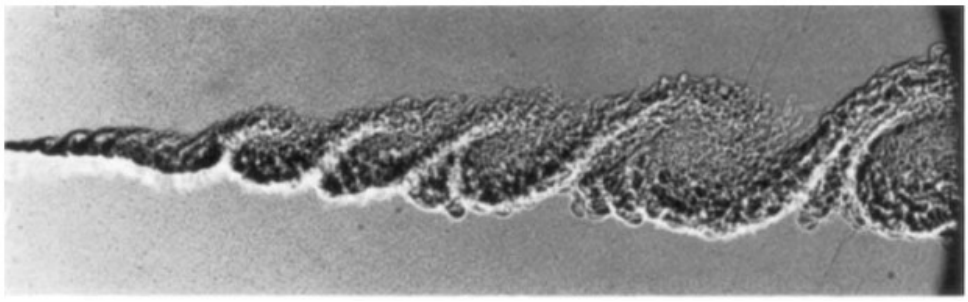

Figure 2.2: Flow visualization by spark shadow [5] (a) $Re \sim 4 \times 5$ (b) $Re \sim 8 \times 10$

2.2 Controlling the Flow via Inflow Conditions

Active flow control is used to manipulate the unaltered flow to one with desired characteristics. In a turbulent mixing layer, the goal is to further enhance mixing of two streams at different velocities. This research is heavily used in the design of various aerospace structures reducing noise production and modeling coherent structures. The turbulent motion typically depends on manipulating either inflow or boundary conditions such as the boundary layer

thickness. Control of mixing layer flow is based on the manipulation of coherent structures that are synonymous with instability modes. Thus, understanding the stability mechanisms of large primary structures is important to achieving such control of the mixing layer.

Manipulating the flow at the trailing edge, an area where the flow is likely to be affected, may highlight the downstream large stream structures' stability characteristics and nonlinear interactions. In order to fully utilize the advantages of the stability characteristics used to control turbulent flow, it is crucial to understand the mechanisms that govern the structures of the flow.

2.3 Two-dimensional forced mixing layers

The controlled sinusoidal oscillation along the entire trailing edge has been used to generate small perturbations at a given frequency. The oscillation merely triggers an instability to enhance its periodicity throughout the flow allowing one to extract information on coherent structure properties through phase-locked measurements. Even if the amplitude of excitation is so small where it does not affect both mean flow and initial energy of the fluctuations, it triggers instabilities and influences the development of mixing layer further downstream.

Flow visualization is able to better manifest the effects oscillation on eddy size, the inclination angle of eddy, and convective wavelength. Comparing Smoke images between the case of forcing at f=40Hz and f=80Hz (Figure 2.3), the development of vortex structures is amplified larger with downstream distance at f=40Hz than at f=80Hz because the forcing frequency is doubling. The other remarkable difference is that incoherent vortices reveal a closer region at f=80Hz than at f=40Hz. This is because saturation point moves upstream to remain the constant saturation Strouhal number, St_s which is a function of the excitation frequency, f, the distance from the excitation location, x_s, and the convection velocity, U_c. When the growth of the mixing layer becomes saturated, vortices amplification will stop and the flow starts decaying.

$$St_s = \frac{f x_s}{U_c} = 2.4 \qquad 2.3$$

$$U_c = \frac{U_2 + U_1}{2} \qquad 2.4$$

(a)

(b)

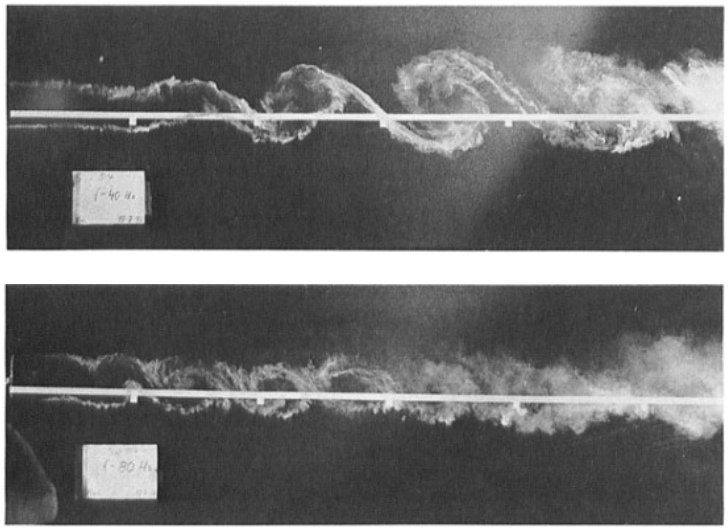

Figure 2.3: Two-dimensional mixing layer smoke image U_1/U_2=0.4 U_2=15m/s [7] (a) f=40Hz (b) f=80Hz

Linear inviscid stability was used to study the spatial evolution of small disturbances in two-dimensional shear layers because turbulent free shear flows are weakly dependent on viscous effects. In addition, it was found that the linear inviscid stability shows that the amplification rate, $-\alpha_i$, varies with the Strouhal number. Note that the Strouhal number, fx_s/U_c, is changed from the one used by Oster and Wygnanski (1978). In addition, it is also a function of the convection velocity of the large eddy, $U_c = (U_2 + U_1)/2$, excitation frequency, f, and the local momentum thickness, θ. When the Strouhal number is based on the local momentum thickness, it represents a non-dimensionalized momentum thickness by the convection wavelength. Experimental spatial growth rates are compared with Michalke's (1965) inviscid stability theory and found to match well with the calculated spatial growth rate (Figure 2.4). The experimental data shows the neutral stability starts from the location at around St=0.07, which is very close to the maximum spatial amplitude predicted by inviscid linear stability of St=0.08. Thus, the initial growth rate and the saturated point has a dependency on the Strouhal number. It was found that the behavior of the large coherent structures governs the mixing layer near the trailing edge when matching the theory used by the inviscid process and experimental data.

$$St = \frac{f\theta}{U_c} = \frac{\theta}{\lambda_x} \qquad 2.5$$

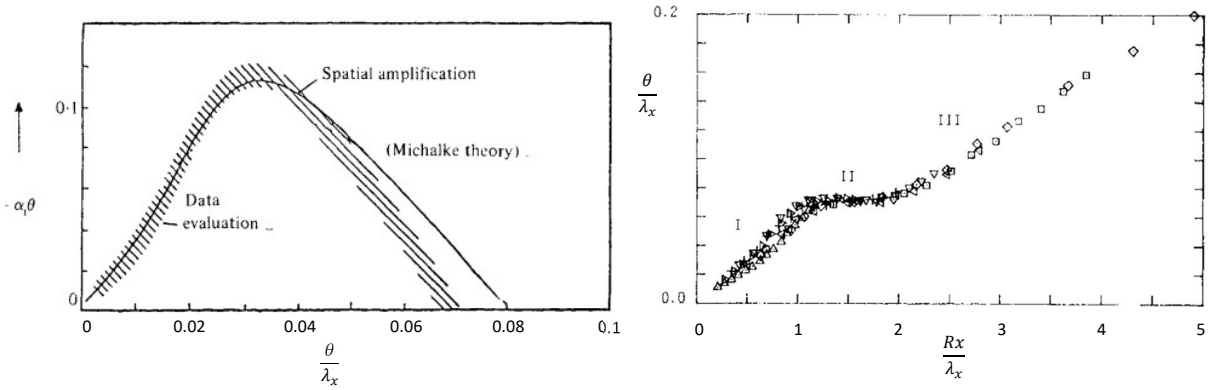

Figure 2.4: Growth rates of the forced mixing layer (a) normalized amplification rates from linear inviscid stability theory [3] (b) growth regions within the forced mixing layer [4] (reproduced from Oster & Wygnanski (1982) and Wygnanski & Petersen (1987))

The convection wavelength based Strouhal number can be written with respect to a normalized streamwise distance, Rx/λ_x, where $R = (U_2 - U_1)/(U_2 + U_1)$. R is the ratio between the vorticity of a large spanwise eddy and the frequency of its occurrence. Note that the large spanwise eddy is related to the rotation and that the frequency of its occurrence is related to the advection velocity of said eddy. The initial growth rate of the forced mixing layer is larger than that of the unforced case in Region I ($0 < Rx/\lambda_x < 1$). The growth of the mixing layer stops in Region II ($1 < Rx/\lambda_x < 2$), indicating a region of neutral stability. In said region, the large spanwise eddies comes to its highest amplitude and starts to decay. The mixing layer resumes its growth at a linear rate which is similar as the unforced case in Region III ($2 < Rx/\lambda_x$). The dominance of large spanwise rolls (Wygnanski et al. 1979, Browand & Ho 1983) indicating that most of the momentum transfer in Regions I and II can be accounted for by assuming that the flow is two-dimensional.

The simplified momentum equation in the x-direction (Eq 2.6) shows the dominant balance for turbulent shear flows between the convection terms and the Reynolds stress terms on the left and right, respectively [9]. When the mean flow is steady and two dimensional, the derivatives with respect to z disappear and $-\partial\overline{u'v'}/\partial y$ is the dominant Reynolds stress component because ∂/∂x term is much smaller than $\partial/\partial y$ term according to the boundary layer approximation. The transfer of momentum from the mean flow to the turbulent flow that results in the generation of spanwise vortices is caused by the mean shear, producing the dominant $-\overline{u'v'}$ term. Thus, the mixing layer's change in size depends on the momentum transfer between

the mean flow and turbulent fluctuations. Note that said fluctuations correspond to the inclination angle of the vortices and the sign of the Reynolds stress, $-\overline{u'v'}$.

$$\bar{U}\frac{\partial \bar{U}}{\partial x}+\bar{V}\frac{\partial \bar{U}}{\partial y}+\bar{W}\frac{\partial \bar{U}}{\partial z}=-\frac{\partial \overline{u'^2}}{\partial x}-\frac{\partial \overline{u'v'}}{\partial y}-\frac{\partial \overline{u'w'}}{\partial z} \qquad 2.6$$

Oscillations at very small amplitudes tend to increase spreading rate of the flow by enhancing the amplification of eddies in the Region I more than in Region III. These oscillations accelerate the rate of amplification of coherent eddies. This corresponds to positive Reynolds stress ($-\overline{uv}>0$).

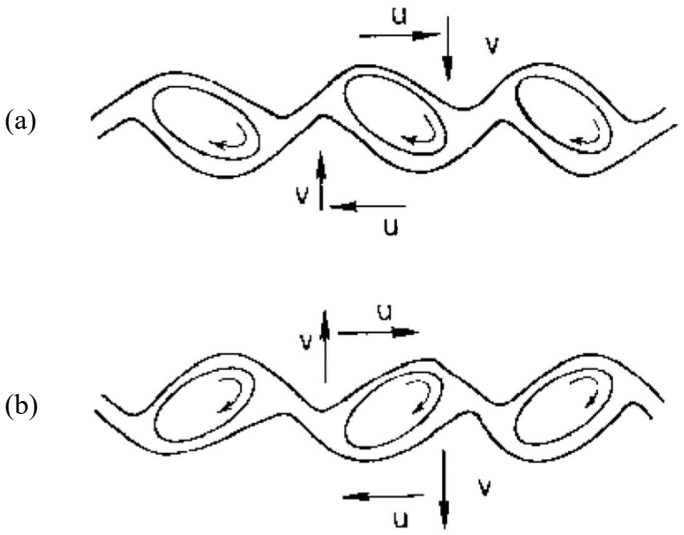

Figure 2.5: The behavior of the vortex [19] (a) Region I (b) Region II

In Region II, the large coherent eddies decay and the inclination angles of the large eddies are reversed compared with Region I. The vortices continue to amplify until it reaches the point of neutral stability to the imposed oscillation where the vortices are oriented vertically with no favorable tilt, and $-\overline{uv}=0$ as it enters Region II. The Reynolds stress in Region II changes sign, indicating that energy is extracted from the turbulent to the mean.

For the further downstream in Region III, the suppression of vortex interaction results in the inhibition of the lateral growth of the shear layer, the generation of negative Reynolds stresses, and hence the extraction of energy from the turbulence to the mean motion and namely a redistribution of the turbulent energy. The structure of a significant subharmonic frequency was not seen. The eddies in Region III which are larger than the eddies associated with the excitation frequency become dominant and are not locked in-phase to the imposed oscillation. This implies

that these eddies are incoherent structures and are responsible for the resumed growth of the shear layer [6].

2.4 The forced mixing layer created from a jagged partition

As shown in previous research, small perturbations are generated at the trailing edge which enhances spanwise vortices. In Figure 2.6, flow visualization unveils the presence of streamwise vortices. The origins of these streamwise vortices were explained by Bernal and Roshko (1986). Large distorted spanwise vortex weaves between adjacent spanwise vortices and constantly changing the orientation of eddies spanwise, which results in both spanwise and streamwise vortices (Figure 2.6).

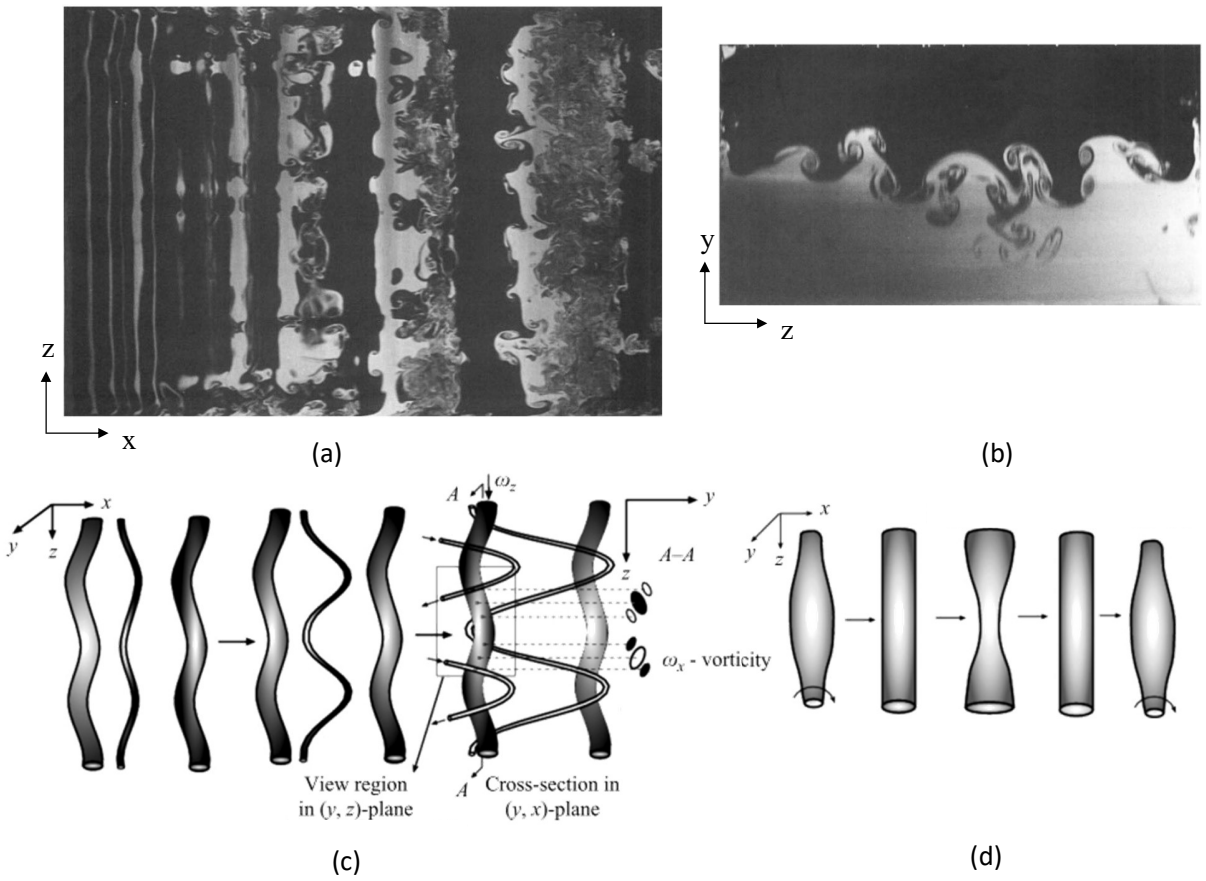

Figure 2.6: Development of spanwise and streamwise vortices [12] [13] [14] (a) Flow visualization of spanwise vortices in the x-z direction (b) Flow visualization of streamwise

vortices in the x-y plane (c) Bending instability (d) Bulging instability

Since the focus on the mixing layer has shifted to the interaction between large spanwise vortices and the streamwise vortices, Kit (2007) investigated the effect of the combination of the spanwise and streamwise vortices on the mean flow and the turbulent flow. Two fliperon were used to manipulate the excitation using controlled sinusoidal signals in his experiment (Figure 2.7). They were both hinged at the trailing edge. One was a triangular 'chevron' shape, called three-dimensional fliperon. The other had a constant chord which created uniform excitation along the span, called two-dimensional fliperon.

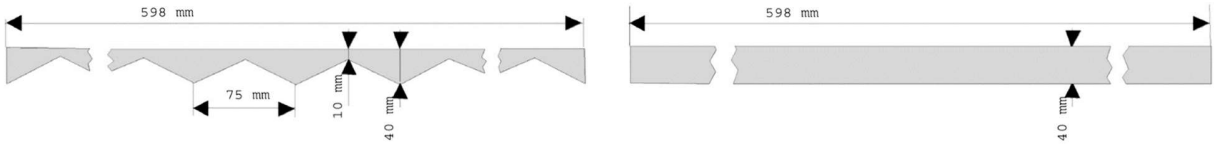

(a) (b)

Figure 2.7: Schematic diagram of (a) three-dimensional fliperon (b) two-dimensional fliperon

The experiment revealed the profile of the mean local center y05 of the mixing layer which was defined as the location where the mean velocity was equal to the average of U_1 and U_2 (Figure 2.8) and the profile of the momentum thickness.

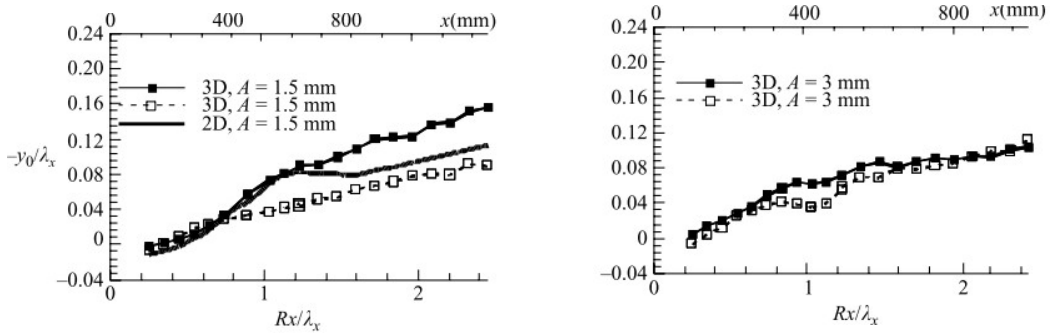

(a) (b)

Figure 2.8: Center of a mixing layer distribution (a) A=1.5mm (b) A=3mm

The center of mixing layer downstream for both notch and cusp of 3D fliperon with an oscillation at A=1.5mm are found on the low-speed stream until $Rx/\lambda_x \approx 0.7$. Beyond this location, the center of mixing layer generated by notch shifted upward vertically compared to center location of mixing layer by cusp. This means that the bending of spanwise vorticities became increasingly significant until $Rx/\lambda_x \approx 1.8$. The bending stopped increasing at $Rx/\lambda_x \approx$

1.8 and center location of the mixing layer moved to low-speed stream at the same rate as 2D fliperon while $Rx/\lambda_x > 1.8$.

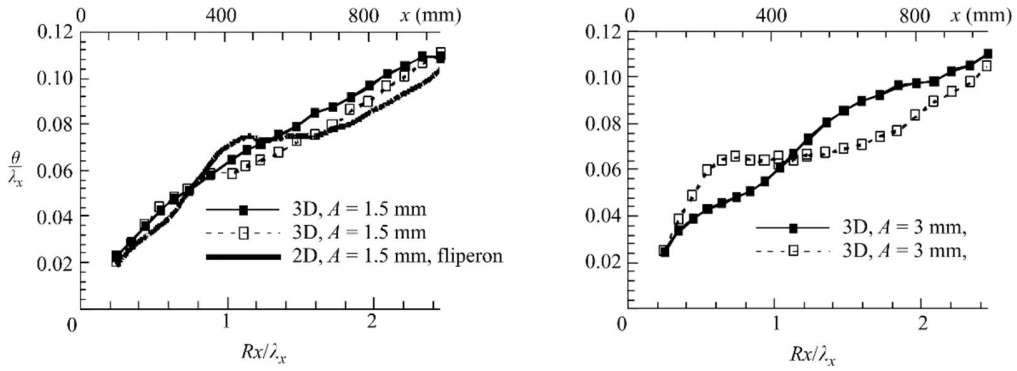

Figure 2.9: Normalized momentum thickness downstream of a chevron fliperon (a) A=1.5mm (b) A=3.0mm

The momentum thickness increases linearly for 3D fliperon with oscillation at A=1.5mm, whereas for 2D fliperon with oscillation at A=1.5mm increased in a nonlinear fashion. Furthermore, mixing layer flow generated from the cusp has its growth rate saturated at approximately $St \approx 0.065$ and $Rx/\lambda_x \approx 0.6$. Whereas the saturation point for the two-dimensional mixing layer is typically at $St \approx 0.07$ and $Rx/\lambda_x \approx 0.7$ as shown in section 2.3. On the other hand, the growth rate of mixing layer flow from the notch constantly varies in a nonlinear fashion. Although the center location of mixing layer downstream for both notch and cusp are the same, its corresponding thickness of mixing layer flow was differs significantly. This could be interpreted as proof of large bulging eddies. Three-dimensional excitations on chevron fliperon enhances K-H instability and modulate ensuing eddies along the span. This led to the development of streamwise vorticities resulting in bending and bulging. There should be an interaction between spanwise rolls and streamwise vortex tubes. However, this result included complicated factors as the flow was affected by multiple edges of notches or cusps.

2.5 The mixing layer created downstream of a "Λ" notch

Zakharin (2009) investigated the effects of a splitter plate mixing layer flow which contains one notch of a chevron ("Λ" notch, Fig 2.10) that represents a single component for

various aerodynamic designs containing multiple chevron petals. According to his research, which showed that the mixing layer distorts throughout the span. The flow was deflected towards the high speed stream at center of test section (z = 0 mm) and to low speed stream for flow located at outboard (z = 150 mm) (Figure 2.10).

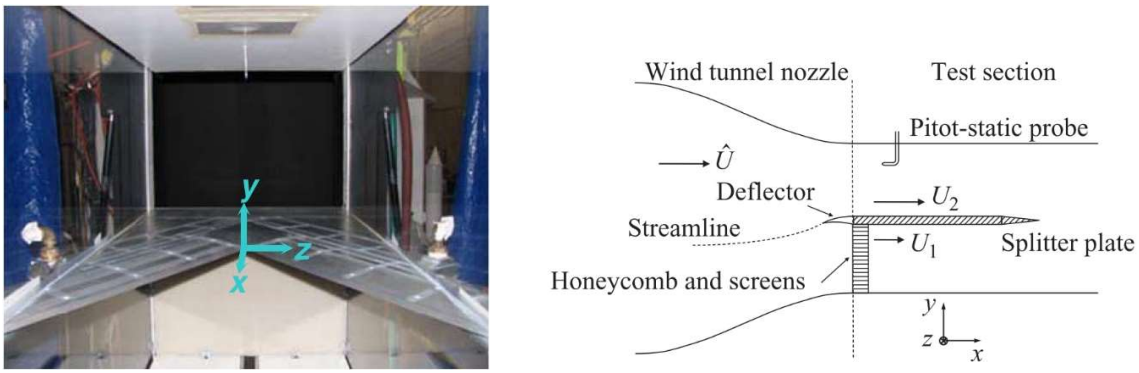

/

(a) (b)

Figure 2.10: Wind tunnel test section using a "Λ" notch splitter plate (a) the front view of wind tunnel photo (b) schematic cross-section view

Kelvin-Helmholtz vortices are not the only reason that affects a downstream motion and deflect the center location of mixing layer towards the low-speed stream. This result seems to be consistent with the Kit's results (2007) of the mixing layer downstream of the notch. This fact and smoke visualization suggest that there are two counter-rotating streamwise vortices.

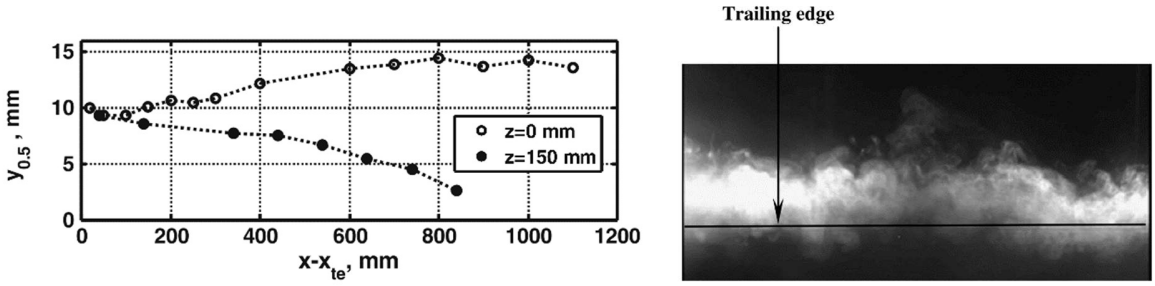

(a) (b)

Figure 2.11: Distortion of the mixing layer (a) center of a mixing layer distribution (b) smoke picture in the crossflow plane taken at $x - x_{TE} = 750mm$

Suehiro (2017) investigated the effects of various-combination conditions of the oscillation at the trailing edge of the "Λ" notch which is the same configuration as the Zakharin's

experiment. The same splitter plate and test section have been used as the Zakharin's experiment. Roughly speaking, in order to understand the effect of the Λ-shaped trailing edge furthermore, Suehiro applied four conditions; unforced, oscillation at a single side ($z/\lambda_z < 0$), both sides simultaneously in phase, and both sides simultaneously in antiphase.

Initially vertical vortices, ω_y, which are induced by velocity profile in the x-z plane, were stretched and tilted by mean shear and Kelvin Helmholtz vortices to be converted into ω_x. These counter-rotating vortices generate an upwash at downstream of the notch and a downwash at the outboard (Figure 2.12). This mechanism was consistent with the Kit's experiment (Figure 2.11).

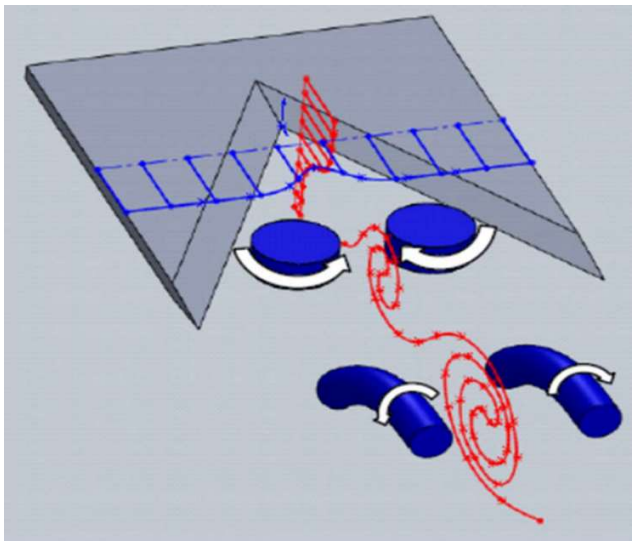

Figure 2.12: Processing of counter-rotating vortices starting from ω_y to ω_x

The width of the unforced mixing layer parallel to the trailing edge remains within the region of $-0.3 < z/\lambda_z < 0$. This turbulent mixing layer appears to agree with the boundary independence principle which is suggested by Wygnanski et al. (2011). Thus, the turbulent flow can be decomposed into two components: a nondivergent component parallel to the trailing edge (Figure 2.13b) and a divergent component normal to the trailing edge (Figure 2.14b). Furthermore, Suehiro had shown that the disturbances originating from one side of the notch do not penetrate too deeply into the other side or are too weak to affect the mean flow on the opposite side. This was seen in the momentum thickness profile for every forced case in the planes parallel to the trailing edge at the outboard locations $z/\lambda_z < -0.15$ (Figure 2.13b) and the momentum thickness profile for unforced and single-side forced cases in the planes normal to the

trailing edge on the opposite side downstream of the outboard locations $z/\lambda_z > 0.1$ (Figure 2.14b).

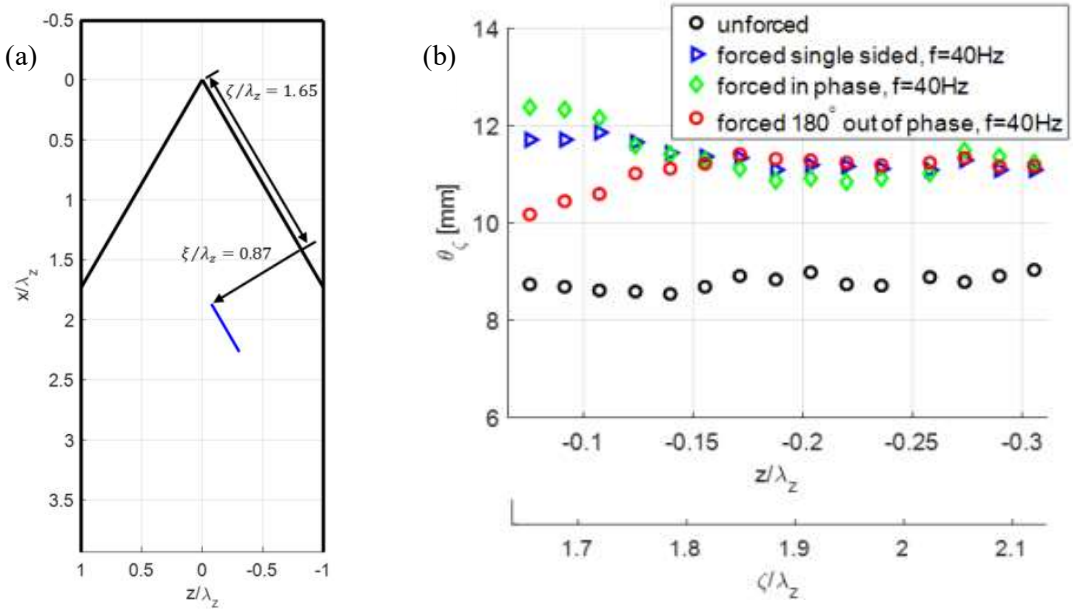

Figure 2.13: Width of the mixing layer in the direction parallel to the trailing edge at $\xi/\lambda_z = 0.87$

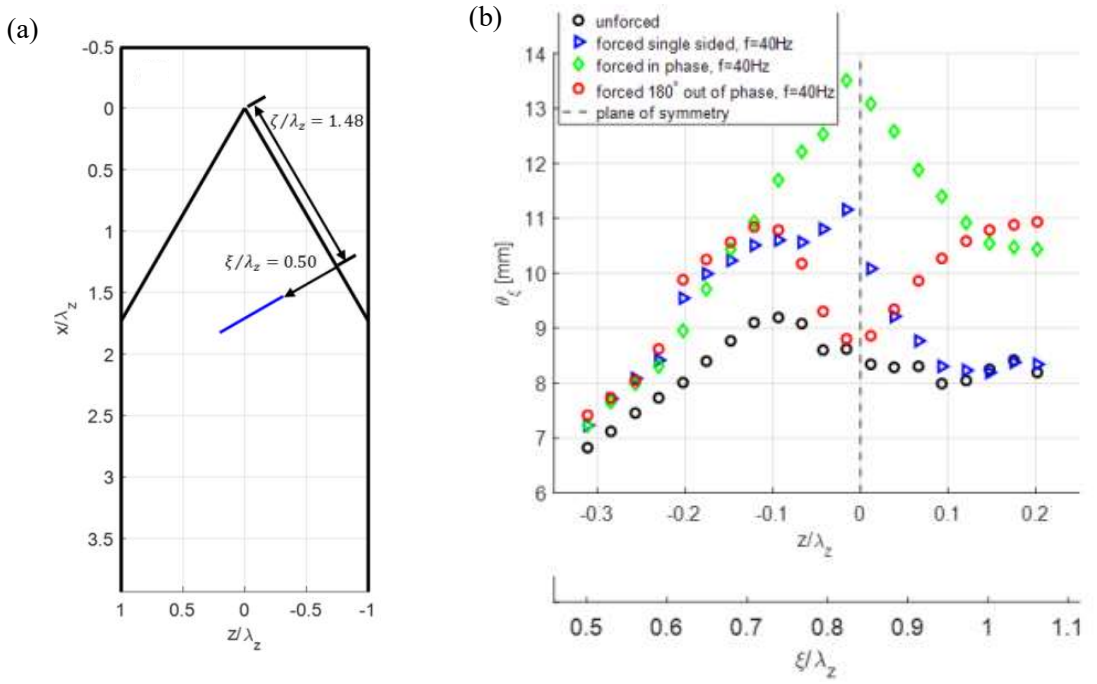

Figure 2.14:Width of the mixing layer in the direction normal to the trailing edge at $\zeta/\lambda_z = 1.48$

The interaction between oblique waves in phase emanating from both sides near the notch center creates a constructive interference. On the other hand, the interaction of oblique waves emanating from both sides in antiphase creates destructive interference near the notch center. There were the nonlinear interactions not only near the notch center, but also opposite effects at the outboard locations (Figure 2.15). This trend can be seen at around z/λ_z=-0.2 in Figure 2.13b and 2.14b as the momentum thickness with the forcing in phase is slightly lower than that of in antiphase and single-sided forcing.

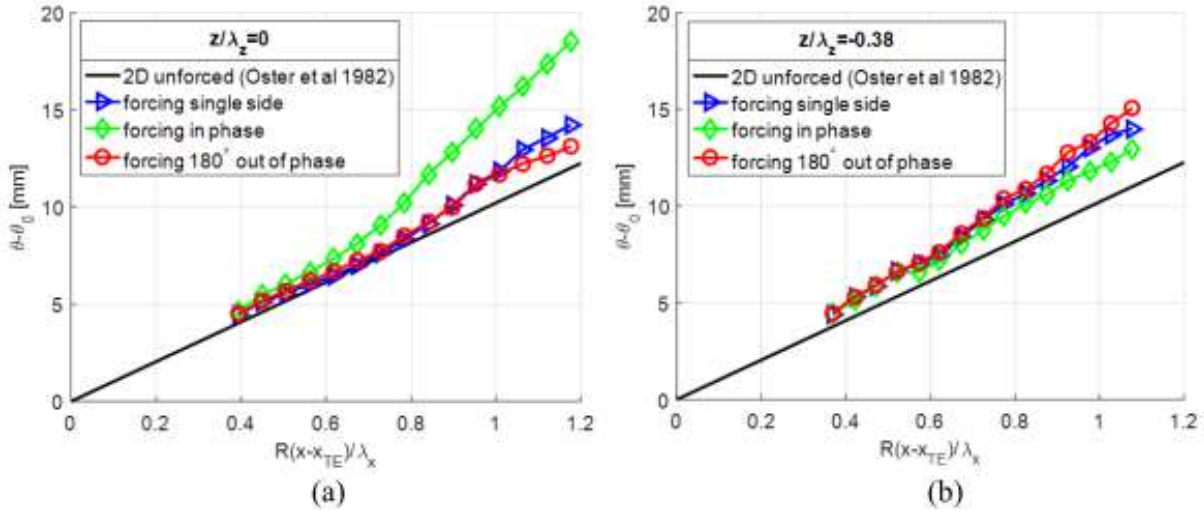

Figure 2.15: Effects of in-phase and 180° out of phase wave interaction on the growth rate, f=20Hz (a) $z/\lambda_z = 0$ (b) $z/\lambda_z = -0.38$

This leads to a conclusion where studying mixing layer flow generated by a single chevron petal is insufficient to obtain a thorough understanding of turbulent mixing layer flow. In Suehiro's case, the three-dimensional mixing layer contains two-sided effect which leads to nonlinear complicated phase interference. Thus, in order to understand the fundamentals of a mixing layer flow, a research is conducted to study just on one-sided effect. The simpler configuration is, the simpler flow becomes. In addition, the swept-back wing for the wind test model is used to make the initial momentum thickness at the trailing edge uniform. This paper examines the behavior of the flow downstream of the swept-back wing.

3. EXPERIMENTAL SETUP & METHODOLOGY

3.1 Description of the Current Experimental Setup

3.1.1 Wind Tunnel

For this research, experiments were conducted in a closed-circuit wind tunnel from the University of Arizona's Aerodynamic Laboratory. In the test section (Fig 3.1) with the help of a sweptback wing, a mixing layer flow is formed through the separation of provided constant airflow into separate airflows with different velocities which will merge at trailing edge of the wing. A perforated metal sheet will be installed between the lower wing and walls of the wind tunnel that serves to control the velocity ratio between both airflows. The two distinct streams have different velocities with one stream flow (named U_2) that travels above the sweptback wing, while the second stream flow (named U_1) travels below the wing and pass through the perforated metal sheet. Recalling basic understanding on flow across an airfoil, a deduction can be made where streamflow U_2 have a greater flow speed compared to streamflow U_1. Adjustments will be further made to the type of perforated metal sheet used to achieve the desired velocity ratio between both airflows. In addition, pressure measurement devices such as static pitot tube was used to check both mean velocity profile of the mixing layer and the vorticity thickness that develops with respect to distance from the trailing edge. It is important to note that checks on the vorticity thickness of the mixing flow were generated without forcing before conducting PIV (Particle Imaging Velocimetry) measurements. Also, PIV measuring equipment were installed where measurements were made parallel to the freestream which will be discussed in further detail at section 3.4.1 of this thesis. Lastly, a pair of speakers were placed right outside the test section while staying parallel to the trailing edge of wing model (Fig 3.1b). These speakers acted as oscillators that allowed the flaperon to oscillate at a specified frequency.

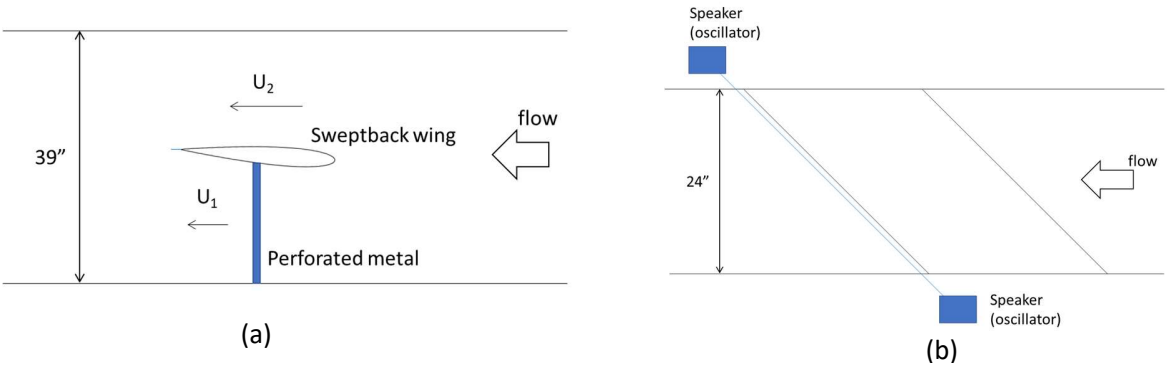

Figure 3.1: Wind Tunnel test Section (a) side view (b) top view

3.1.2 Sweptback Wing

The sweptback wing used in this research was a NACA 0009 symmetric airfoil with fixed geometry that spanned the entire width of the test section (2 ft). A rectangular flaperon was made out of piano wire and aluminum tape that was approximately 0.03-inch-thick which was then hinged onto the trailing edge with Kapton tape. For this research, a symmetric airfoil was chosen as it is suitable for a wide range of airspeeds to study the effects of a controlled oscillating flaperon. Also, the wing is installed to the test section with a sweep back angle of 45° with respect to the free stream flow as shown in Fig 3.1b. Cross section of the wing model setup is shown in Fig 3.2 along with the respective dimensions. In addition, small spanwise groove was made at 5.3 inches downstream of trailing edge that allowed the perforated metal sheet to be mounted onto the wing. The wing was installed with a negative angle of attack of 4º to keep the subsonic flow attached to the leading edge of the wing surface which ensures the initial flow to be properly separated with minimal frictional effects.

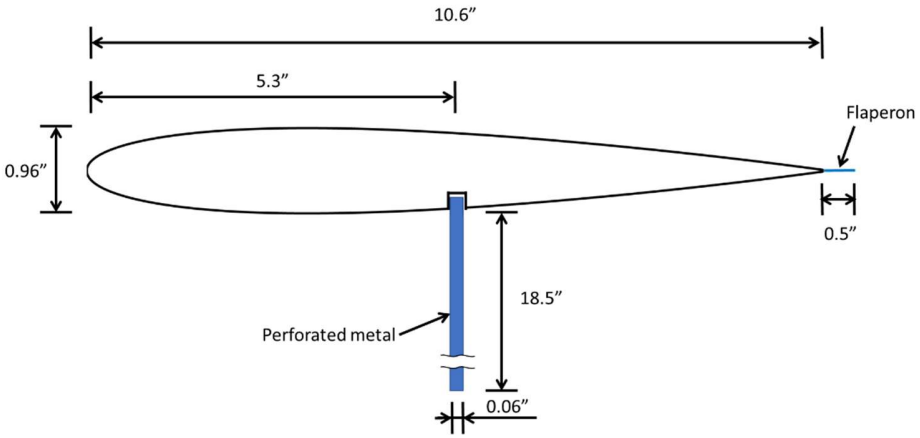

Figure 3.2: Wind test model of the swept-back wing

3.1.3 Perforated Metal Sheet

The steel perforated metal sheet used in this experiment was 0.06 inches thick with 63% open area. The holes were round with 0.156-inch diameter, spaced 0.032 inch apart and arranged in a staggered row. One of the several challenges faced during this experiment was the installation of a 0.06-inch-thick perforated metal sheet was fixed to both the wing and walls of test section. Initial attempt was a simple surface mounting of the metal sheet onto the surface of wing, however there were small gaps between both metal sheet and wing model that vary in size due to unavoidable imperfect mounting. These small gaps were further expanded as the thin metal sheet oscillates during testing which led to airflow from the tunnel nozzle to flow through these gaps resulting in a non-uniform spanwise flow. This led to modifying the metal sheet to eliminate the presence of varying small gaps. There were less gaps compared with the initial attempt. However, as the metal sheet was loosely fitted, it was still able to oscillate heavily resulting a uniform spanwise seam to expand significantly that affected the precision of the desired velocity ratio. An attempt was made to minimize the effects of metal sheet oscillating by constant manual adjustments to the sheet. Finally, the mounting end of metal sheet was to a shape of the spanwise groove, which ensured a tight fit and reduced vibrational effects to a minimum. Experimental data that were collected throughout these stages of modifications have varying degrees of precision but accurately describe the growth of mixing layer downstream. As previously mentioned, the metal sheet plays a vital role in reducing flow speed located below the wing which allowed users to control velocity ratio between both flow streams.

3.1.4 Actuation system

There were a pair of speakers, ET-132-2 (LABWORKS INC) mounted on both external sides of the wind tunnel and were aligned with the flaperon. Additional metal structuring was placed outside of the wind tunnel for the pair of speakers to be attached as well as providing room for manual adjustments in translation or rotation that properly aligned with the flaperon. These electrodynamic transducers serve as control points that help provide oscillation control signal from the amplifier directly to flaperon. On the other hand, source of the oscillation signal was generated from a PA-119 (LABWORKS INC) linear power amplifier which bifurcated and supplied the sinusoidal forcing signal to both speakers. An oscilloscope was then connected to the power amplifier which allowed user to both monitor and control forcing signals. Finally, a stroboscope was used to visually verify that flaperon had a uniform oscillation across the entire wingspan.

3.2 Coordinate System

The coordinate systems used are defined in Fig 3.3. Streamwise coordinates are shown in Fig 3.3 where the origin is located at one end of the trailing edge where the wing is attached to the wind tunnel window. The velocity components U and V correspond to the velocity components in the x and y directions respectively. It is important to note that most of streamwise measurements were taken relative to the trailing edge, $x - x_{TE}$, for a given spanwise location z.

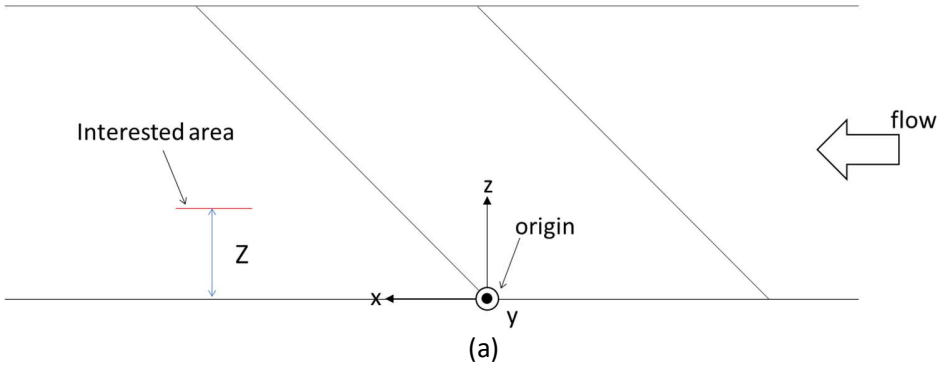

(a)

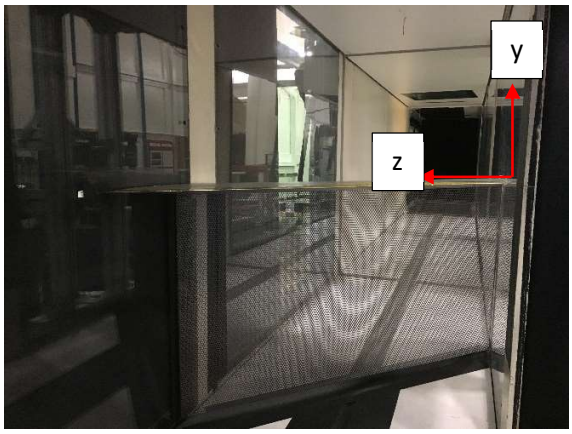

(b)

Figure 3.3: Coordinate system (a) top view (b) front view

3.3 Test Conditions

3.3.1 Velocity Ratio

A velocity ratio of $U_1/U_2 = 0.64$ was used throughout this research where the high-speed streamflow velocity was $U_2 = 15.6$ m/s while the low-speed streamflow was at U_1=10 m/s. For this research, an assumption was made where the momentum thickness equal to zero throughout entire wing and the flow at trailing edge to be laminar. Following this assumption, the Strouhal number (St) is also assumed to be 0. Strouhal number is defined as a function of excitation frequency (f), momentum thickness (θ), and convection velocity (U_c) as shown below. The convection velocity is defined as the mean of both upper and lower stream flows.

$$St = \frac{f\theta}{U_c} = \frac{\theta}{\lambda_x}$$

$$U_c = \frac{U_2 + U_1}{2}$$

Referring back to section 2.3, the regions of mixing layer growth and decay are associated with transfer of momentum from the mean flow to the turbulent flow (Eq 2.6). For this reason, the spatial growth rate is crucial as it enables users to verify the transition of turbulent mixing layer from region I to region II. As shown in Fig 2.5, when the mixing layer is in region I its momentum thickness increases, then transitions to remained neutral in region II, and continues increasing at region III due to Kelvin-Helmholtz instability. In this research, both

regions I and II were heavily focused on as these regions contain many characteristics of the mixing layer for further analysis in section 4.

3.3.2 Forcing Parameter

As PIV method could only record velocity fields within a limited area of the test section, forcing parameters must be chosen carefully in order to obtain data on the two-dimensional mixing layer's saturation point. Figure 3.4 was used as reference when choosing forcing parameters values. A common trend was noted for various forcing amplitudes whereby the momentum thickness spiked when the mixing layer reached a stagnation point. Region II was shown to be independent of varying forcing amplitudes. The forcing amplitude chosen for this research was A = 1.5 mm. The forcing frequency used in this experiment were f = 50 Hz and 75 Hz respectively. These variables limits were chosen to provide an accurate representation of the two-dimensional mixing layer traveling downstream while meeting equipment limitations. This is proven in the two-dimensional mixing layer with a forcing frequency of 50Hz and the location of the plateau seen in Region II is independent of the amplitude if the flow is properly amplified (Fig 3.4).

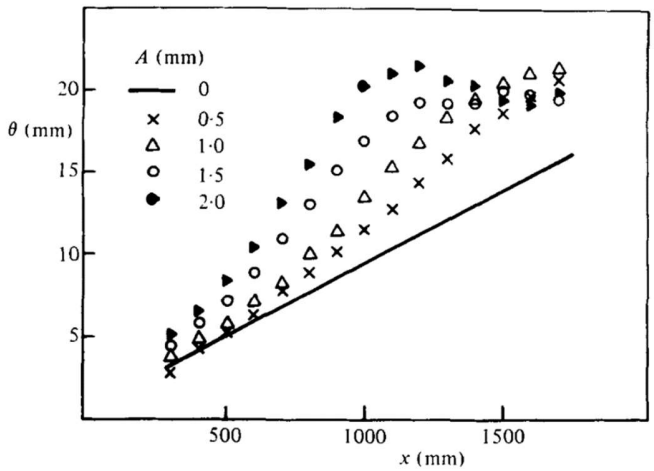

Figure 3.4: The momentum thickness profile with different amplitude [3]

3.4 Data acquisition

3.4.1 Pressure measurement system

A pitot rake was used to measure the mean velocity profile. The pitot rake was consisted of 29 simple pitot tubes and two pitot-static tubes on the top and bottom. The pitot rake traversed using motors in the x and z-direction in order to acquire pressure data along the streamwise and spanwise direction. The pitot rake also traversed in the y-direction in order to increase the spatial resolution. The data was taken every 0.125” spacing in the y-direction. A damper with two rollers top of the traverse system was designed to avoid any vibration due to vortex shedding with pressing the ceiling of the wind tunnel. The ratio of the frontal area of the traverse system to the stream cross-sectional area is approximately 4%. In low-speed wind tunnel test, the blockage effect which produces an effective change in flow speed or dynamic pressure is negligible when the blockage is less than 5% being typical [16]. Pressures were measured with a Pressure Systems 780B with two pressure scanner modules, ESP-16HD.

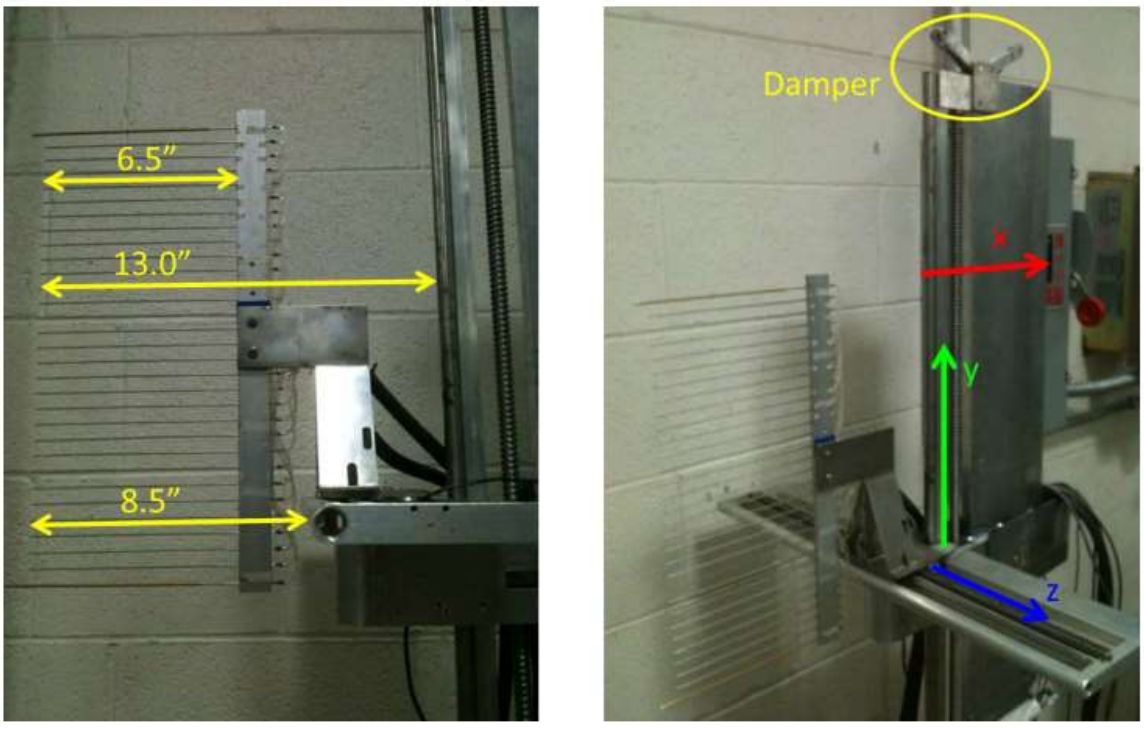

(a) (b)

Figure 3.5: Pressure measurement system [11] (a) pitot rake (b) traverse

3.4.2 Particle Image Velocimetry

Particle Image Velocimetry was used to obtain spatially resolved velocity measurements throughout the mixing layer. 2D-PIV was used to obtain the two-components of the velocity in x and y direction which were corresponded to parallel and normal to the freestream, respectively.

The laser was placed over the wind tunnel ceiling, and the laser light sheet came from the tunnel ceiling passing through the window on the ceiling. The laser calibration plate was placed within the interested area to calibrate the camera and was used to align the position of the laser. The camera, Lavision's sCMOS camera, was placed at about 90° to the interested area. Phase-locked data which were a series of 300 image pairs were captured for 8 different phase angles of the forcing frequency. Random sampling which were a series of 500 image pairs were taken and averaged. The acquisition and processing of the PIV images were done using DaVis 8.4.0 provided by Lavision. An Aerosol generator was used that generated particle (DEHS (2-Ethylhexyl sebacate) particle mean size less than 1 μm) ingested into the wind tunnel behind the test section providing uniform seeding density at the test section. These PIV data acquisitions which were taken at random frequency and phase-locked sampling will then be combined in order to investigate the effect of coherent components and the spatial evolution of these structures that occur.

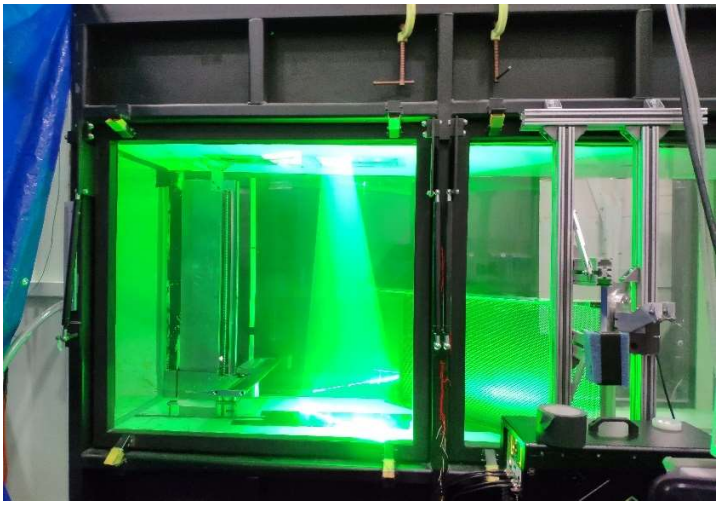

Figure 3.6: PIV setup

The uncertainty of the velocity fields can be determined by the averaged RMS uncertainty ($\sqrt{\sum U_x^2 /N}$) divided by the square root of the number of samples. This formula gives

an uncertainty value in a unit of m/s and can use to calculate the error as a percentage of the freestream velocity. The uncertainty of the PIV data can be estimated to be ±1.1%.

$$U_{\bar{x}} = \frac{\sqrt{\sum U_x^2 / N}}{\sqrt{N}}$$

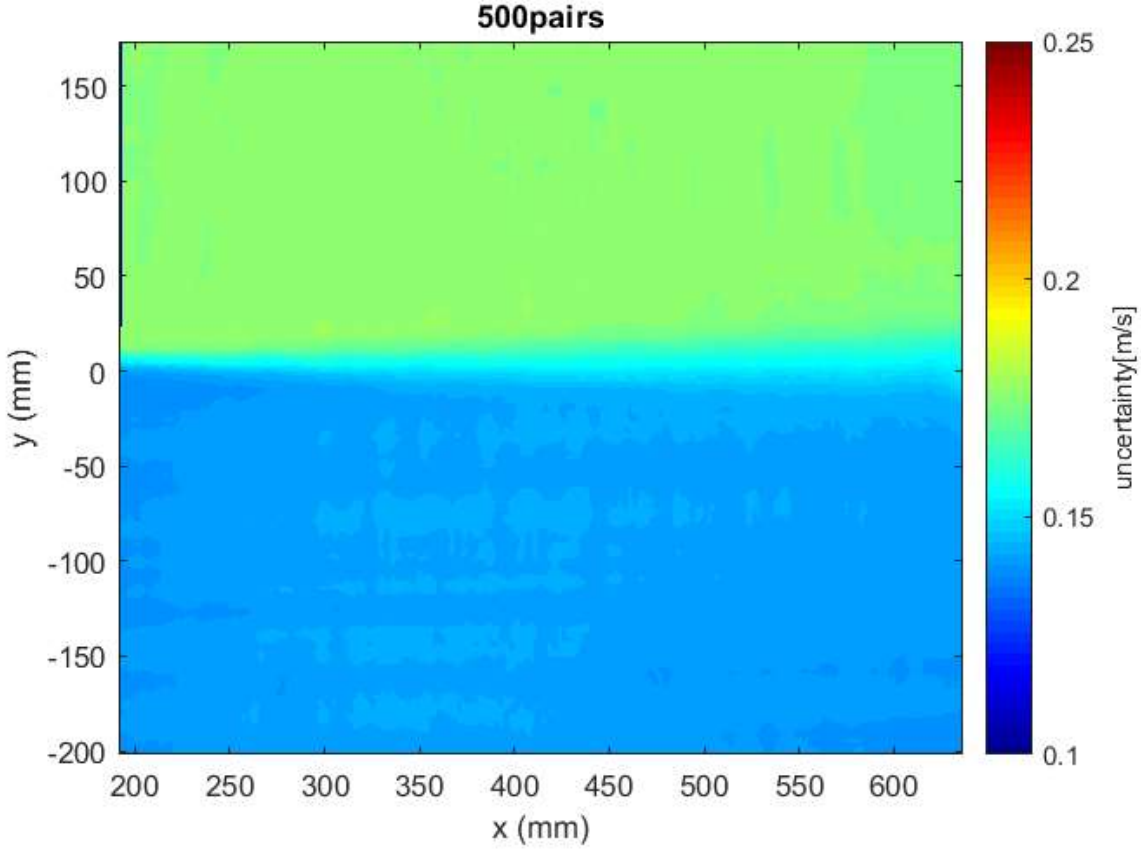

Figure 3.7: Uncertainty field

4. DISCUSSION OF EXPERIMENTAL RESULTS

The experimental results collected for this research can be separated into two categories, one was taken at a random sampling frequency while the other was collected at eight different phases of phase-locked sampling frequency that are evenly spaced apart by 45°.

4.1 Random Sampling Data

4.1.1 Vorticity Thickness Profile and Momentum Thickness Profile Without Forcing

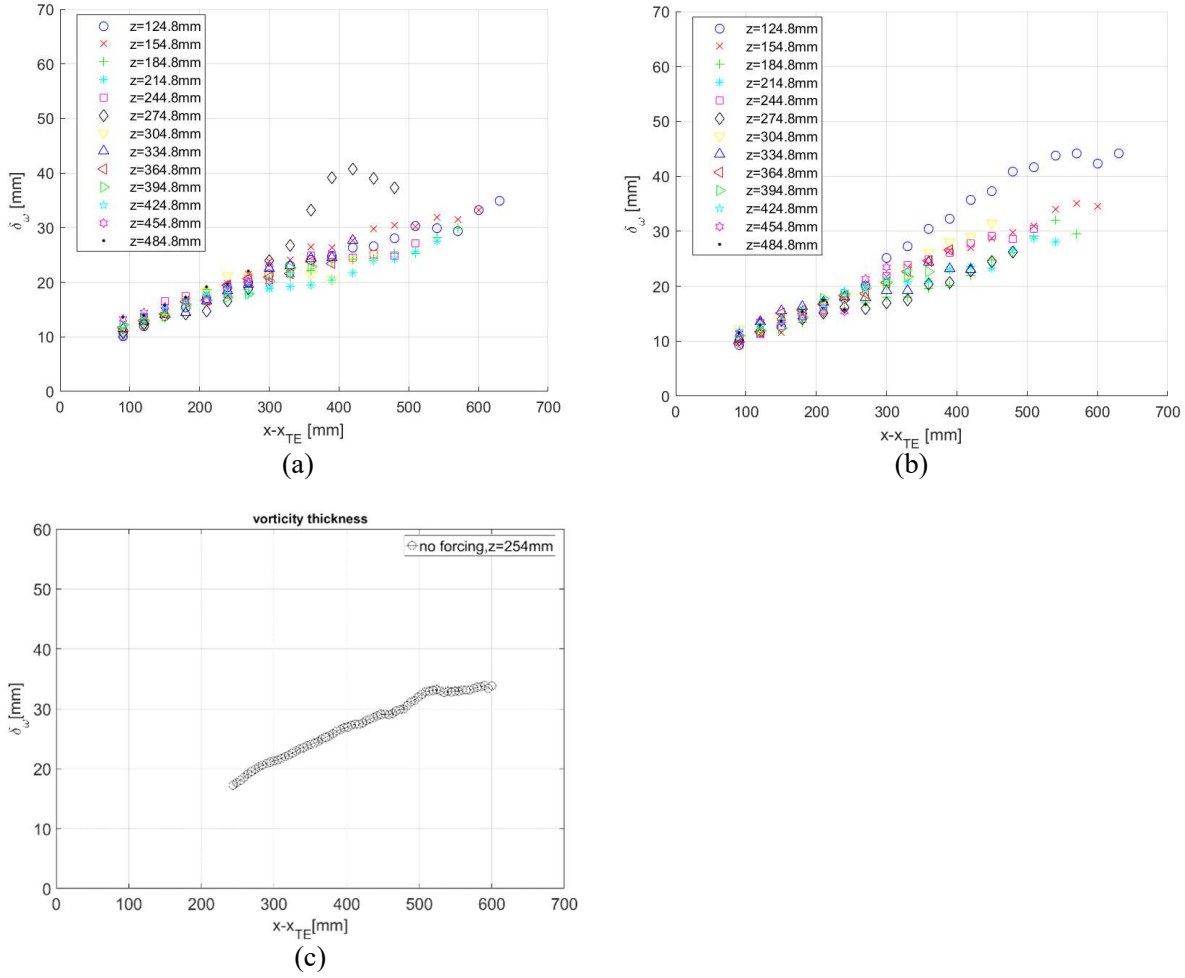

Figure 4.1: The Vorticity Thickness Distribution collected with various perforated metal sheet modifications (a) Loose fit and (b) Loose fit with Manual Alignment, and collected using PIV data (c) Tight Fit

Figure 4.1 shows the results of the vorticity thickness profile varying with respect to distance downstream from trailing edge without forcing. Figures 4.1(a) and (b) were obtained via pressure measurement system that contained plots of vorticity thickness distribution across the wingspan. While Figure 4.1(c) was collected through PIV method which only contain the vorticity thickness plot at z = 254 mm. At this stage of experimentation, the perforated metal sheet was undergoing modifications in attempt to reduce vibrational effects that affect velocity ratio control. Figures 4.1(a) and (b) were obtained at initial stages of mounting the perforated metal sheet to the wing. A large spike of vorticity thickness is present on both plots as a result of vibrational effects on the perforated metal sheet. Fortunately, both plots are still accurate in showing that vorticity thickness develops almost linearly downstream for the entire wingspan. On the other hand, Figure 4.1(c) was generated with the final modification made to mounting the perforated metal sheet. With a tight and secure mounting, the metal sheet suffered minimal vibrational effects. The result from Figure 4.1(c) also shows that vorticity thickness increases in a linear-like fashion downstream. In general, both PIV and pressure measurement system agree that without any forcing, vorticity thickness increases linearly downstream for the entire wingspan. However, both methods are unable to avoid the presence of vibrational effects on the metal sheet that affects face issues in achieving precise velocity ratio control.

4.1.2 Vorticity thickness profile and momentum thickness profile with forcing

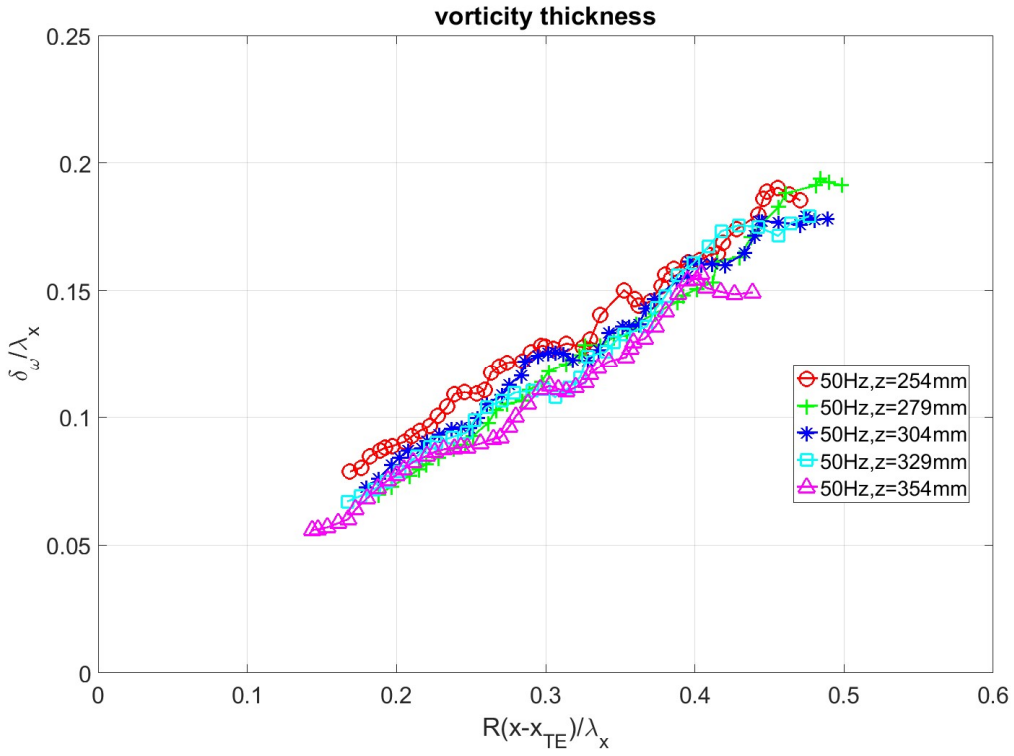

(a)

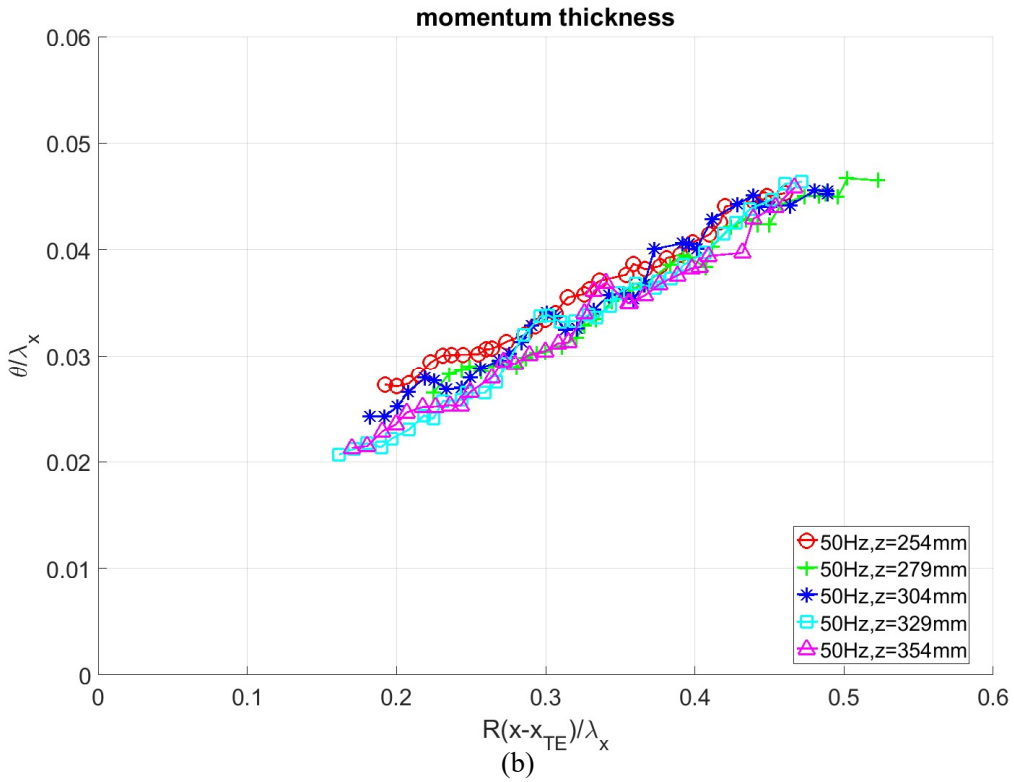

(b)

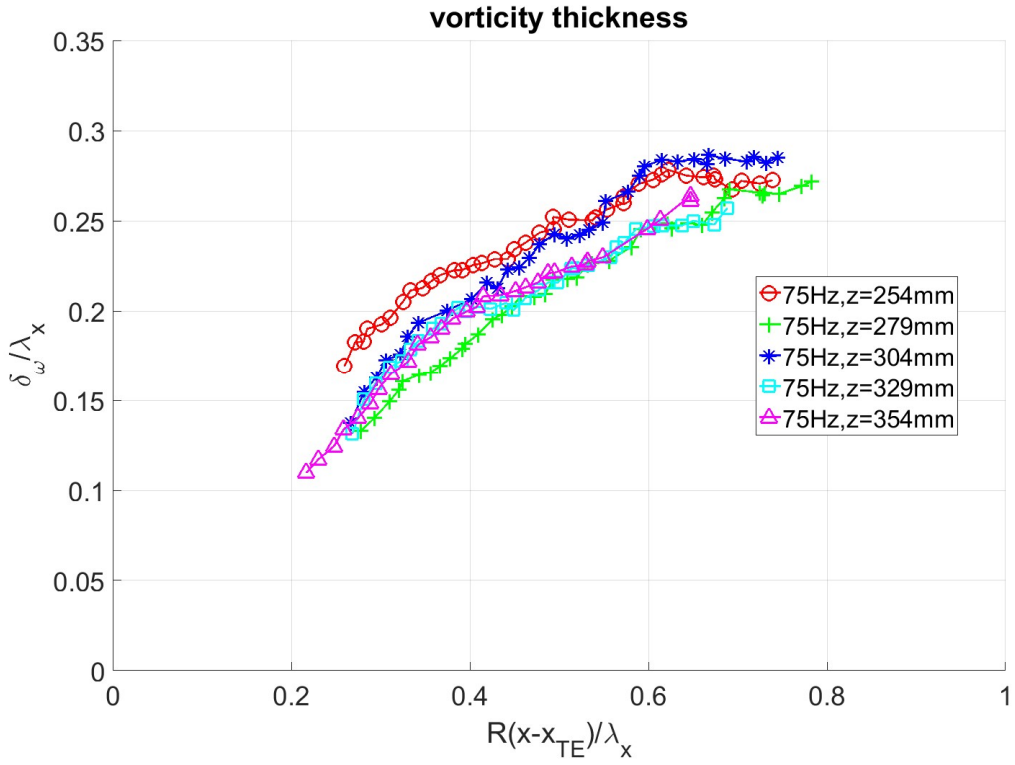
vorticity thickness
0.35
0.3
0.25
0.2
0.15
0.1
0.05
0
0
0.2
0.4
0.6
0.8
1
δ_ω/λ_x
$R(x-x_{TE})/\lambda_x$
75Hz,z=254mm
75Hz,z=279mm
75Hz,z=304mm
75Hz,z=329mm
75Hz,z=354mm

(c)

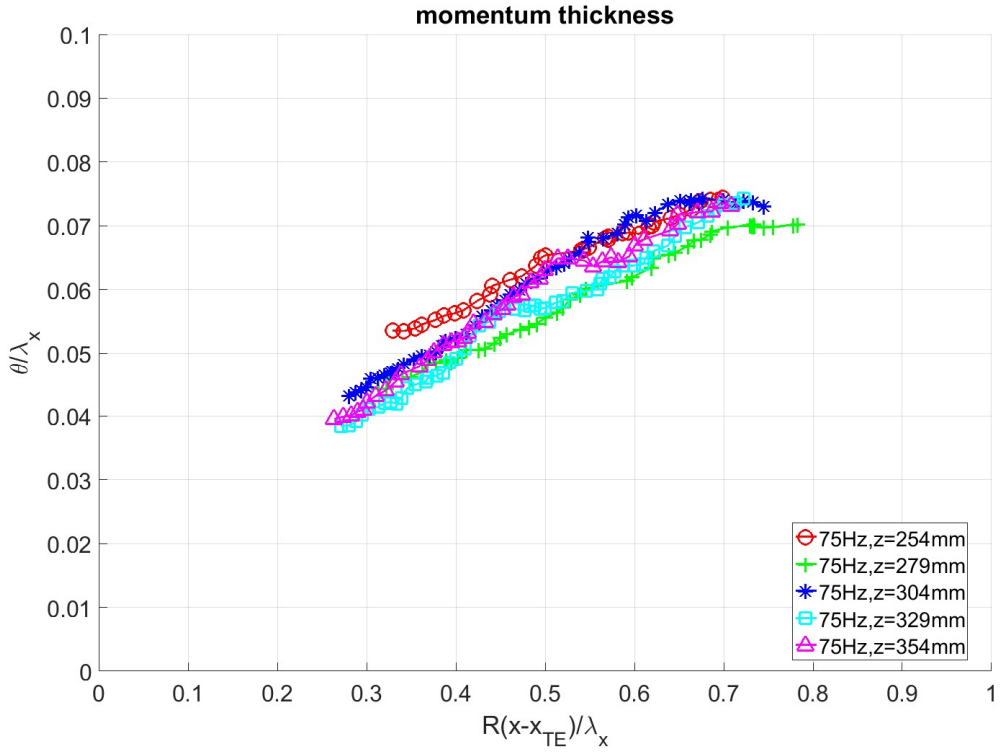
momentum thickness
0.1
0.09
0.08
0.07
0.06
0.05
0.04
0.03
0.02
0.01
0
0
0.1
0.2
0.3
0.4
0.5
0.6
0.7
0.8
0.9
1
θ/λ_x
$R(x-x_{TE})/\lambda_x$
75Hz,z=254mm
75Hz,z=279mm
75Hz,z=304mm
75Hz,z=329mm
75Hz,z=354mm

(d)

Figure 4.2: Normalized growth rate of the mixing layer (a) Vorticity thickness with forcing frequency of f=50Hz (b) Momentum thickness with forcing frequency of f=50Hz (c) Vorticity thickness with forcing frequency of f=75Hz (d) Momentum thickness with forcing frequency of f=75Hz

For a forcing frequency of f = 50 Hz, the vorticity thickness profiles across the wingspan develops similarly to Figure 2.4(b). Whereby for Figure 4.2(a), the vorticity thickness across the wingspan seems to increase linearly until the flow reaches 0.4 or 0.45 of normalized distance downstream. It can be expected based on the independence principle for turbulent mixing layer flow, its momentum thickness along the trailing edge will show a uniform profile. However, the data is slightly scattered in the z-direction. This implies that there is the imperfective for the spanwise flow.

Figures 4.2 (c) and (d) contain vorticity and momentum thickness profiles for a higher frequency of excitation, f = 75 Hz. It can be seen from both figures that the range of both vorticity and momentum thickness are multiplied by about 1.5 times compared to the corresponding profiles for an excitation frequency of 50Hz. For both the vorticity thickness profiles and momentum thickness profiles, large distortions and fluctuations are apparent for both profiles in the spanwise and free stream direction. This is because of the overamplified excitation frequency on a turbulent flow. A combination of either subharmonic or harmonic frequencies might have affected the amalgamation within the region of $0.3 < R(x - x_{TE})/\lambda_x < 0.7$. As such, the turbulent mixing layer flow could not be simplified into regions different flow expansions due to enhancements on coherent structures of the fundamental frequency. The momentum thickness profiles across the wingspan increases linearly until the flow reaches 0.45 or 0.7 of normalized distance downstream where momentum thickness then stays constant. The saturation point for the two-dimensional mixing layer can be located approximately at $St \approx 0.07$ and $Rx/\lambda_x \approx 0.7$ as seen in section 2.3. Thus, this indicates the large range at $R(x - x_{TE})/\lambda_x = 0.45$ or 0.7 might be the neutral points for the corresponding spanwise locations due to distortions generated by an overamplified excitation frequency.

Moreover, the mixing layer flow can be decomposed into divergent (normal to trailing edge) and non-divergent (parallel to trailing edge) components based on the independence principle. This can be simplified as a rotation of the coordinate system by 45°, where both $x -$

x_{TE} and λ_x will be multiplied by cos(45°) which is perpendicular to the trailing edge. This in turn will divide the vertical axes of Figures 4.2 by a scalar of cos(45°). From this, the Strouhal number that corresponds to saturation points for an excitation frequency of 75 Hz is $St \approx 0.1$. Furthermore, one may expect the saturation point for 50 Hz. However, in order to recognize the plateau clearly, the larger swept-back angle will be needed. Smaller velocity ratio also can be used for improvement of the data.

4.1.3 Mean Velocity Profile

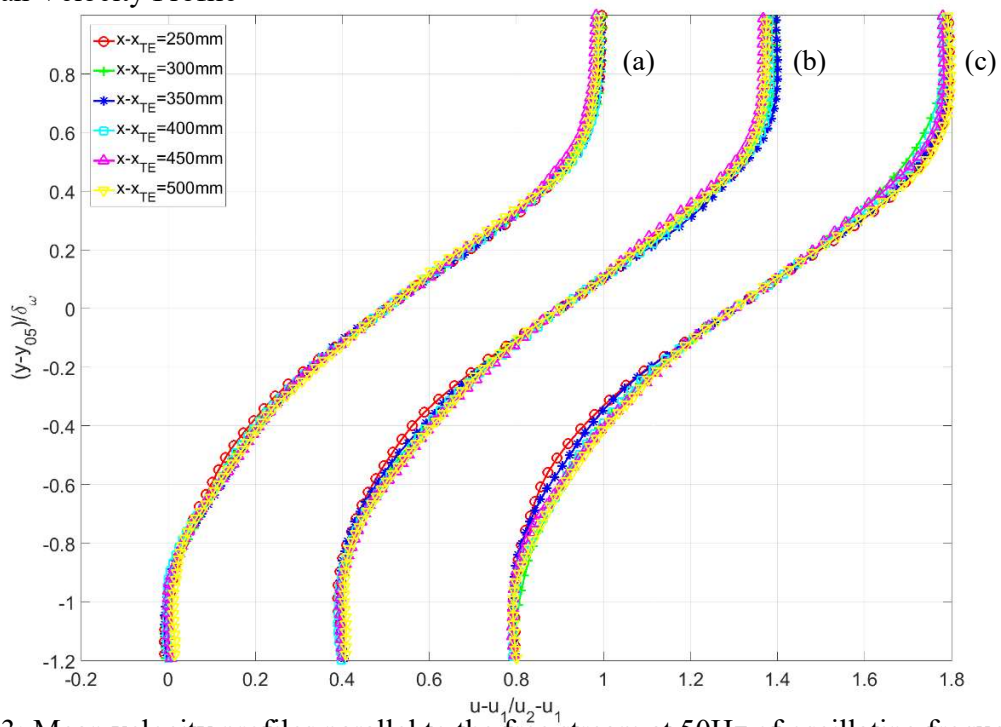

Figure 4.3: Mean velocity profiles parallel to the free stream at 50Hz of oscillating frequency nondimensionalized by vorticity thickness (a) z=254mm (b) z=304mm (c) z=354mm

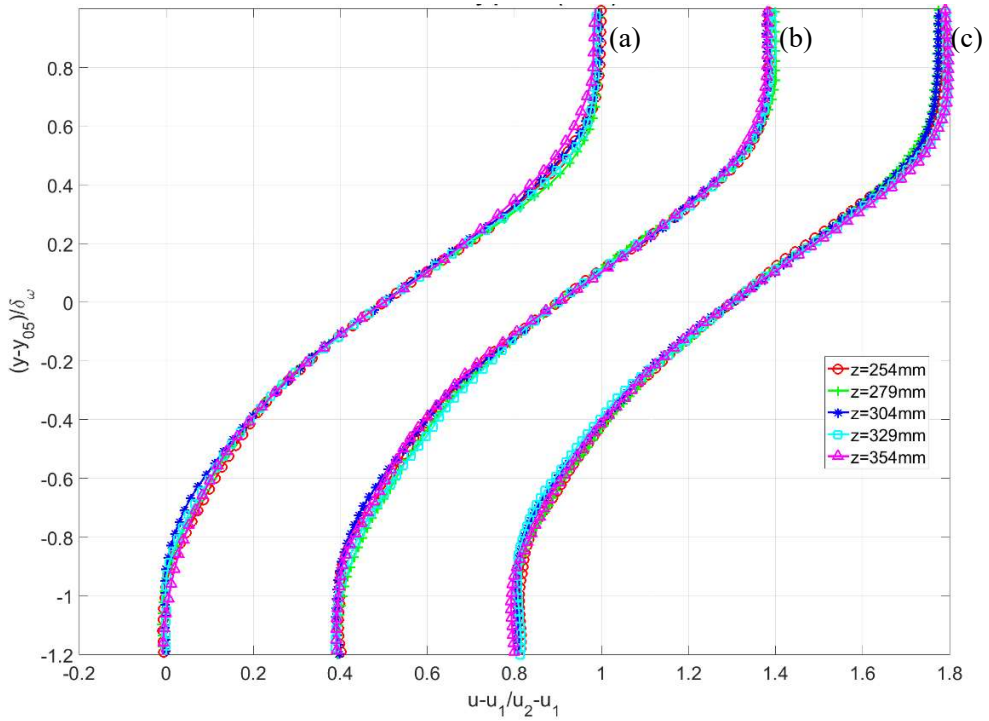

Figure 4.4: Mean velocity profiles parallel to the trailing edge at 50Hz of oscillating frequency nondimensionalized by vorticity thickness (a) $x - x_{TE} = 300mm$ (b) $x - x_{TE} = 400mm$ (c) $x - x_{TE} = 500mm$

Figure 4.3 shows the mean velocity profiles varying with vertical position of the mixing flow with forcing frequency at 50 Hz for three spanwise locations (z = 254mm, 304mm, 354mm). Figure 4.4 shows the mean velocity profiles varying with vertical position of the mixing flow for the same forcing frequency for three trailing edge locations ($x - x_{TE}$ = 300mm, 400mm, 500mm). The velocity profiles of mixing flow were tabulated via subtracting low-speed stream and nondimensionalized by velocity difference between both low and high-speed streams ($U_2 - U_1$). Next, the difference of vertical (y) positions and central vertical position (y_{05}) of mixing flow will be nondimensionalized by local vorticity thickness (δ_ω). This procedure is traditional in mixing layer research since the velocity difference between the two streams provides the initial Kelvin-Helmholtz vorticity necessary to maintain the mixing layer.

The mean velocity profiles appear to attain self-similarity for all downstream and trailing edge location. Minor deviations in both velocity profiles were likely caused by the wake region having a dominant presence in the vicinity of the trailing edge. As velocity profiles were able to achieve near-perfect self-similarity downstream, this indicates that the flow can be decomposed into divergent and non-divergent components which further simplify the flow as a two-dimensional mixing layer flow.

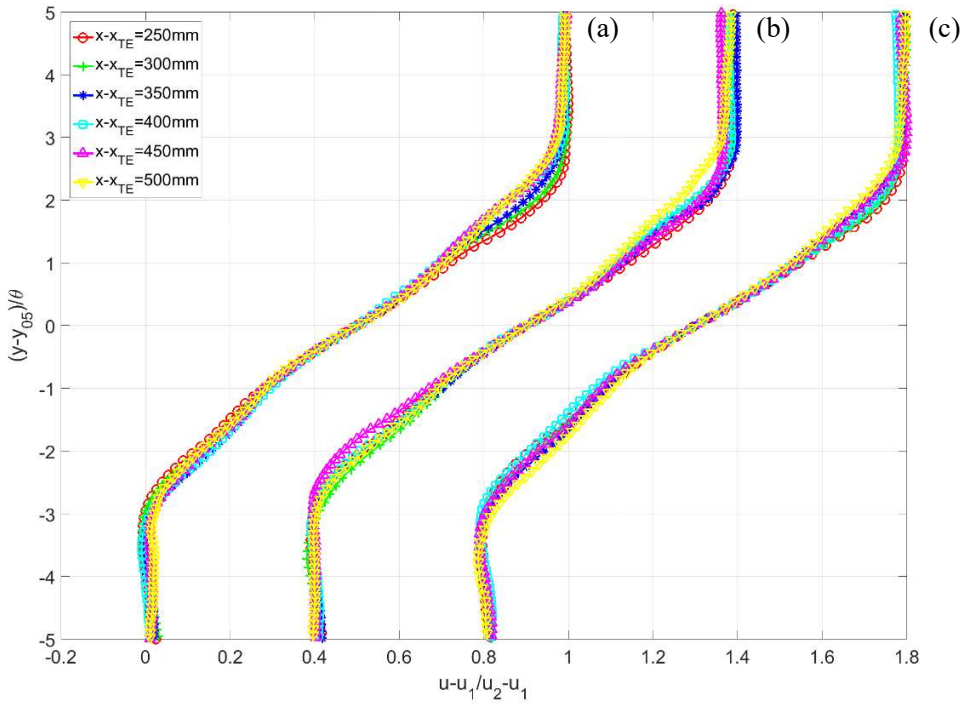

Figure 4.5: Mean velocity profiles parallel to the free stream at 75Hz of oscillating frequency nondimensionalized by momentum thickness (a) z=254mm (b) z=304mm (c) z=354mm

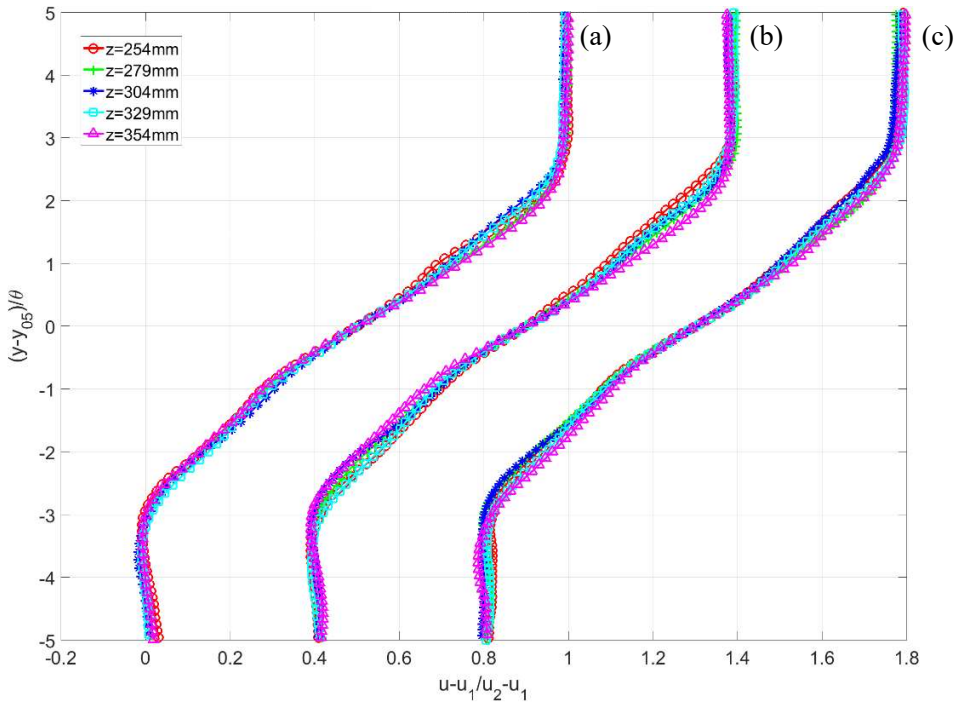

Figure 4.6: Mean velocity profiles parallel to the trailing edge at 75Hz of oscillating frequency nondimensionalized by momentum thickness (a) $x - x_{TE} = 300mm$ (b) $x - x_{TE} = 400mm$ (c) $x - x_{TE} = 500mm$

Figure 4.5 shows the mean velocity profiles varying with vertical position of the mixing flow and forcing frequency at 75 Hz for three spanwise locations (z = 254mm, 304mm, 354mm). Figure 4.6 shows mean velocity profiles varying with vertical position of the mixing flow and forcing frequency at 75 Hz for three trailing edge locations ($x - x_{TE}$ = 300mm, 400mm, 500mm). Unlike the previous velocity profile plots at f = 50 Hz where its vertical positions of mixing flow were nondimensionalized by local vorticity thickness, the vertical positions of mixing flow at f = 75 Hz were nondimensionalized using momentum thickness. This is because when comparing between the vorticity and momentum thickness profile for f = 75 Hz, the momentum thickness profile is relatively stable which meant easier calculations for further analysis.

These velocity profiles show multiple inflection points present downstream and along the trailing edge, unlike velocity profiles for f = 50 Hz where only one inflection point is present (Figures 4.5 and 4.6). This is because of the overamplified excitation frequency and the flow was dominated not only by the fundamental frequency but also by harmonic frequencies. Figures 4.5 and 4.6 further support this statement as the velocity profiles did not attain self-similarities in

both directions parallel to trailing edge and along the free stream. There are fluctuations present in both the upper and lower sides of the center-located vortex, which indicates other instability modes are present in this flow. Although this results in the mixing flow at f =75 Hz to be much more complex than mixing flow at f = 50 Hz, the flow is similar to the two-dimensional mixing layer because the pairing of the frequency can be seen in the two-dimensional mixing layer [15].

It is widely accepted that for shear flow, its mean velocity profile does not match with its corresponding mean temperature profile. This is also true in the case of a heated shear flow where its mean temperature profile exhibits several instability modes. Turbulent temperature fluctuations occurred mostly at the periphery of each vortex while its core was fairly quiescent and well mixed. The inflection points present in for mean velocity profile at f = 75 Hz infers that turbulent mixing layer flow could not be simplified into regions different flow expansions due to enhancements on coherent structures of the fundamental frequency. These inflection points in both mean temperature and velocity profiles hints the presence of an unknown complex instability mechanism.

4.1.4 Fluctuating velocity

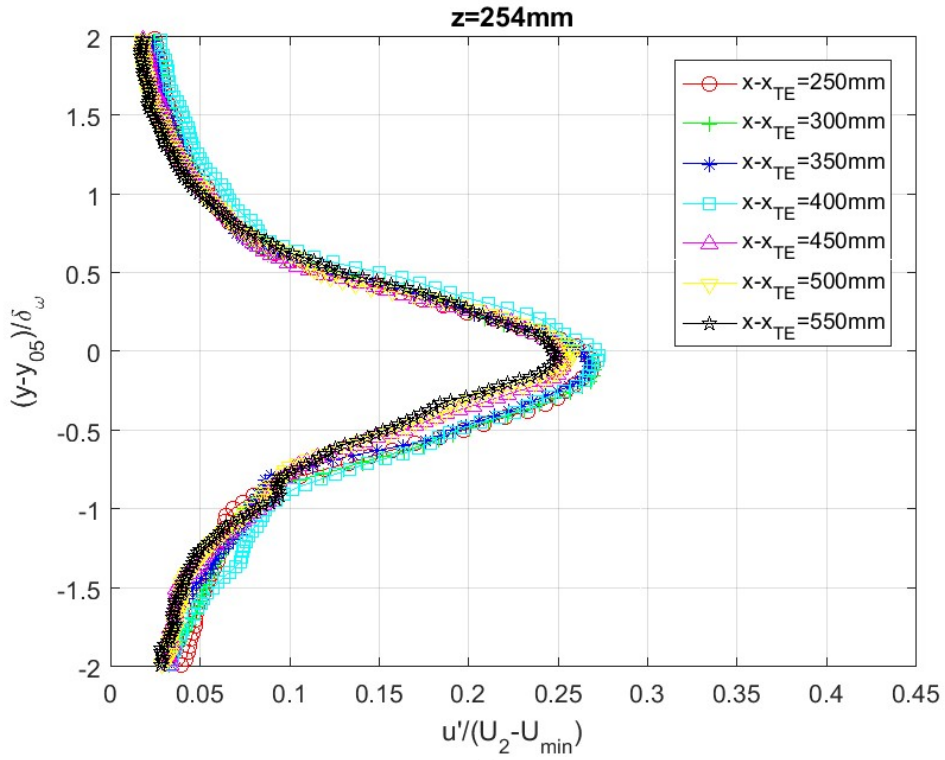

(a)

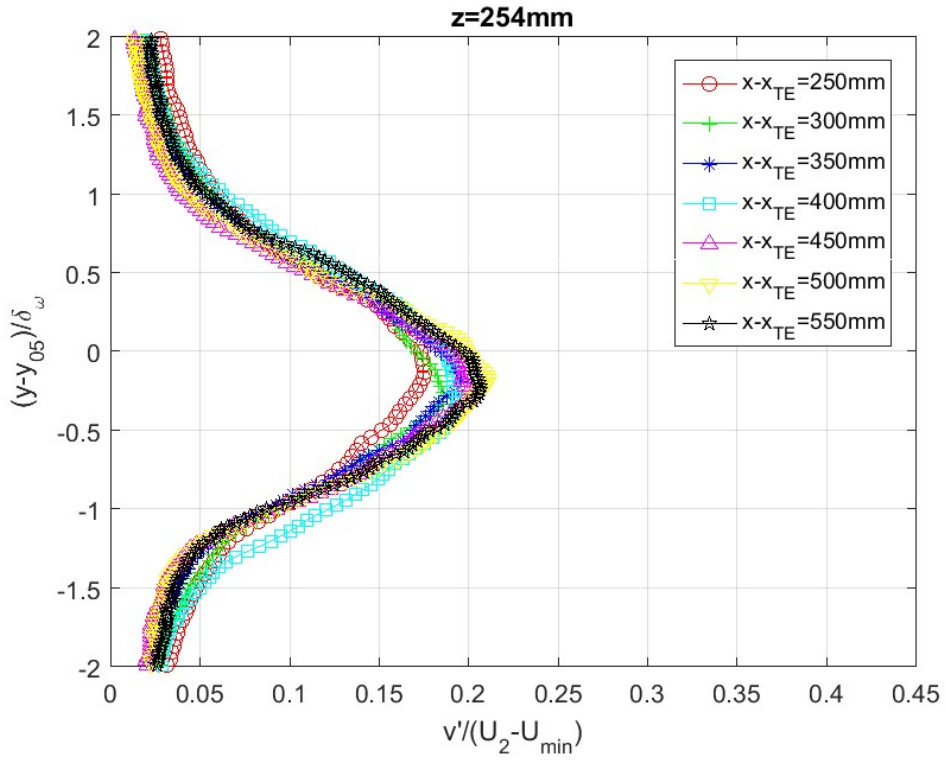

(b)

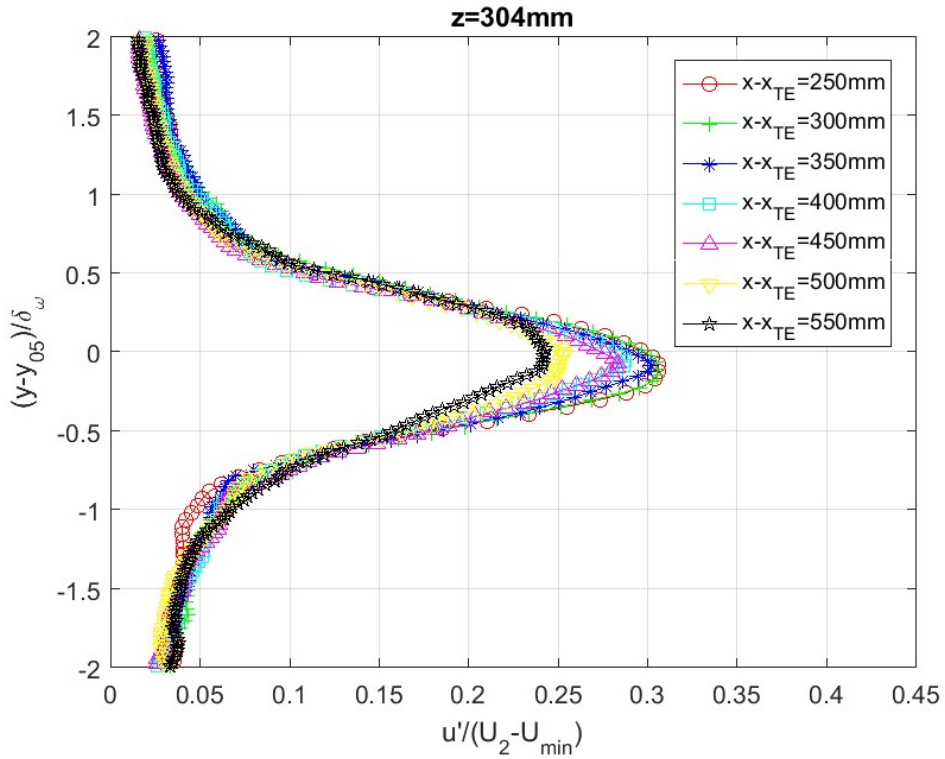
z=304mm
x-x_TE=250mm
x-x_TE=300mm
x-x_TE=350mm
x-x_TE=400mm
x-x_TE=450mm
x-x_TE=500mm
x-x_TE=550mm
(y-y_05)/δ_ω
u'/(U_2-U_min)

(c)

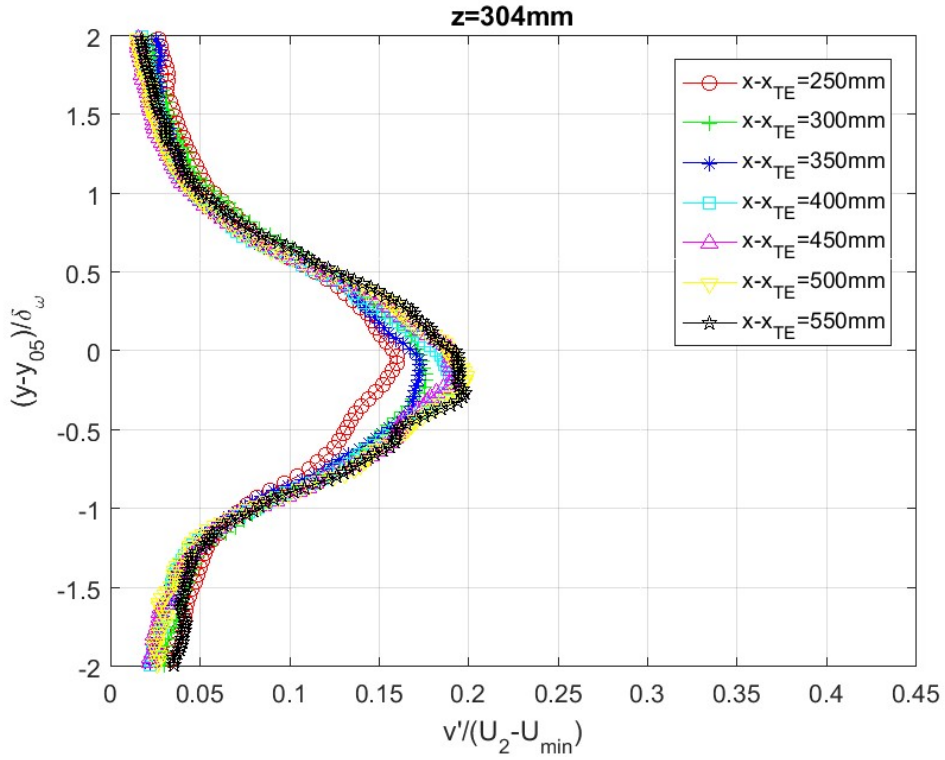
z=304mm
x-x_TE=250mm
x-x_TE=300mm
x-x_TE=350mm
x-x_TE=400mm
x-x_TE=450mm
x-x_TE=500mm
x-x_TE=550mm
(y-y_05)/δ_ω
v'/(U_2-U_min)

(d)

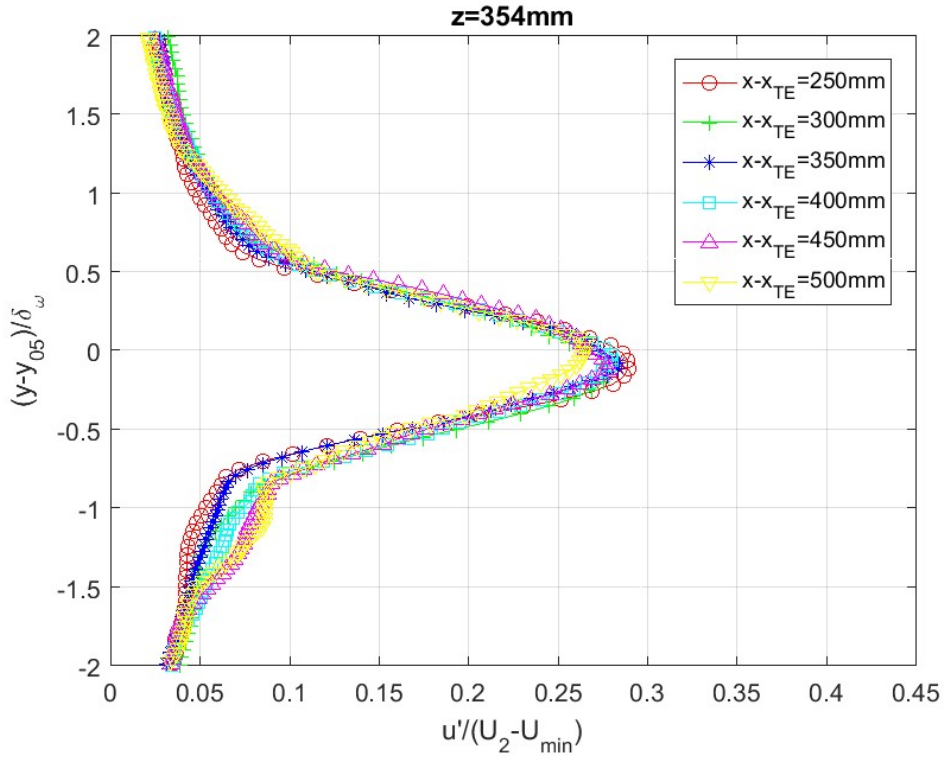

(e)

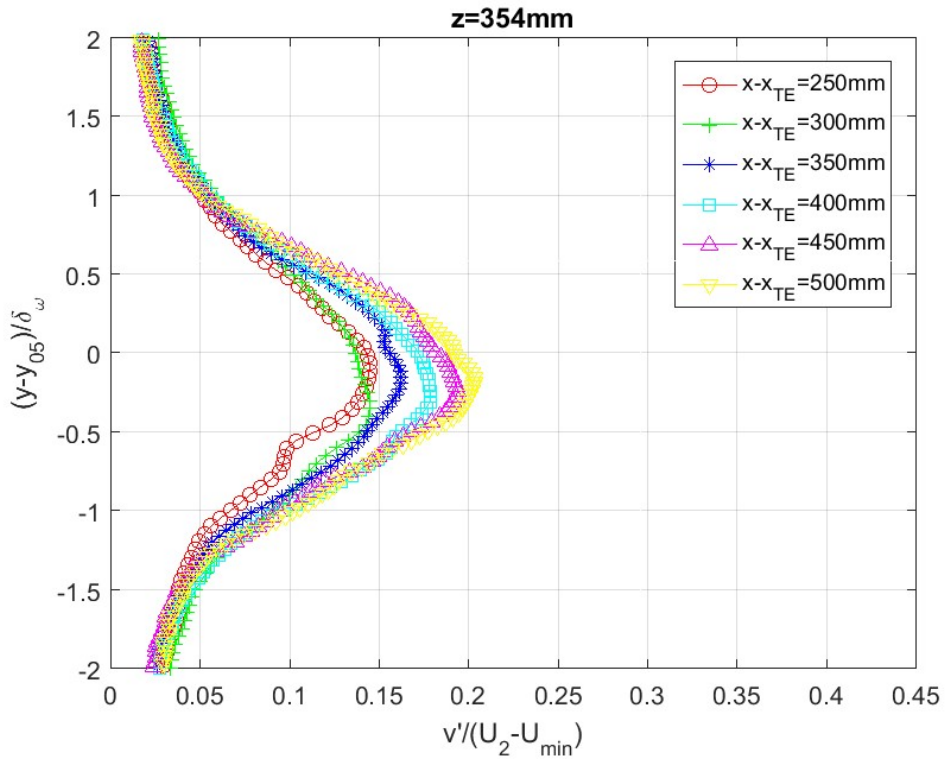

(f)

Figure 4.7: Turbulent intensities of u and v components at 50Hz of the oscillating frequency at (a), (b) z=254mm (c), (d) z=304mm (e), (f) z=354mm

Figures 4.7 shows the turbulent intensities for both streamwise and vertical velocity components of the swept-back wing with forcing frequency at 50 Hz for three spanwise locations (z = 254mm, 304mm, 354mm). For all spanwise locations within the distance $x - x_{TE} < 450mm$, the maximum intensity of the streamwise component $\overline{u'^2}^{1/2}$ remains constant and its intensity profiles appear to be self-similar downstream. On the other hand, vertical velocity component of turbulent intensity $\overline{v'^2}^{1/2}$ increases slightly downstream up to the region of $x - x_{TE} < 450mm$. These characteristics are commonly seen in Region I of a two-dimensional mixing layer flow [3]. For downstream region of $x - x_{TE} > 450mm$, the maximum intensity of $\overline{v'^2}^{1/2}$ stays constant at 0.2, and its intensity profiles appear to be self-similar. Such unique trend where the maximum velocity intensity remains constant can only be found in Region II of a two-dimensional mixing layer flow [3]. This suggests that there are no correlations between $\overline{u'^2}$ and $\overline{v'^2}$ as these variables are independent of one another. If the flow can be simplified into a two-dimensional mixing layer, then the v velocity component should be proportional to the w velocity component. According to the momentum equation in the x-direction for turbulent shear layers, the streamwise momentum is balanced by the momentum fluxes $-\overline{u'^2}$, $-\overline{u'v'}$, $-\overline{u'w'}$ with no dependency on correlations between v' and w'.

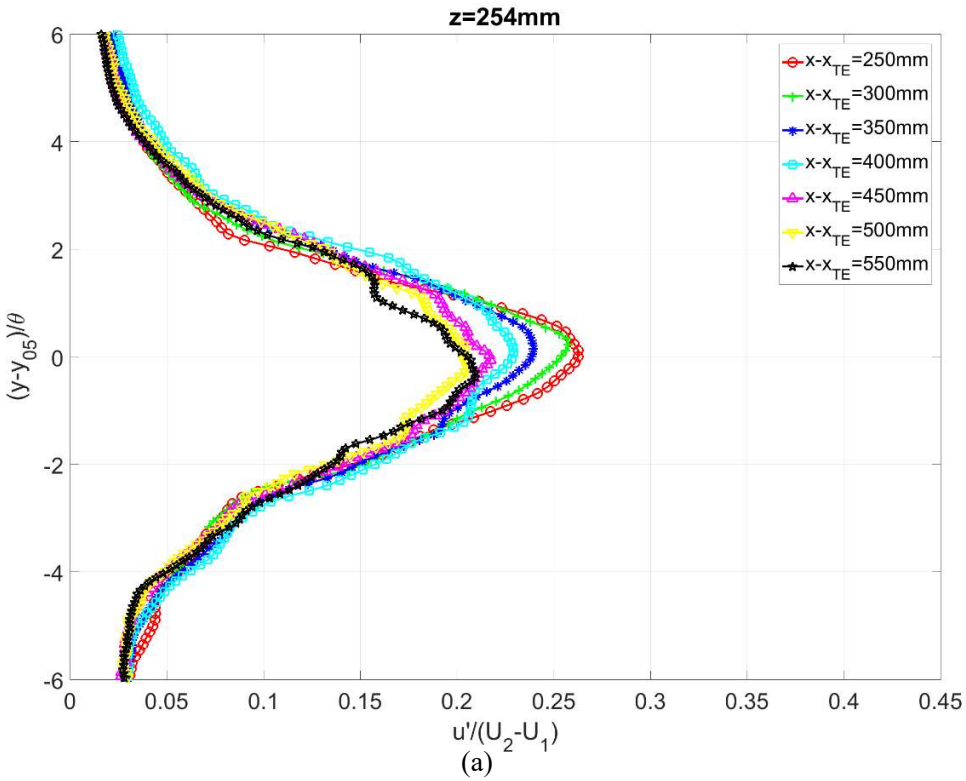
z=254mm
x-x_TE=250mm
x-x_TE=300mm
x-x_TE=350mm
x-x_TE=400mm
x-x_TE=450mm
x-x_TE=500mm
x-x_TE=550mm
(y-y_05)/θ
u'/(U_2-U_1)
6
4
2
0
-2
-4
-6
0
0.05
0.1
0.15
0.2
0.25
0.3
0.35
0.4
0.45

(a)

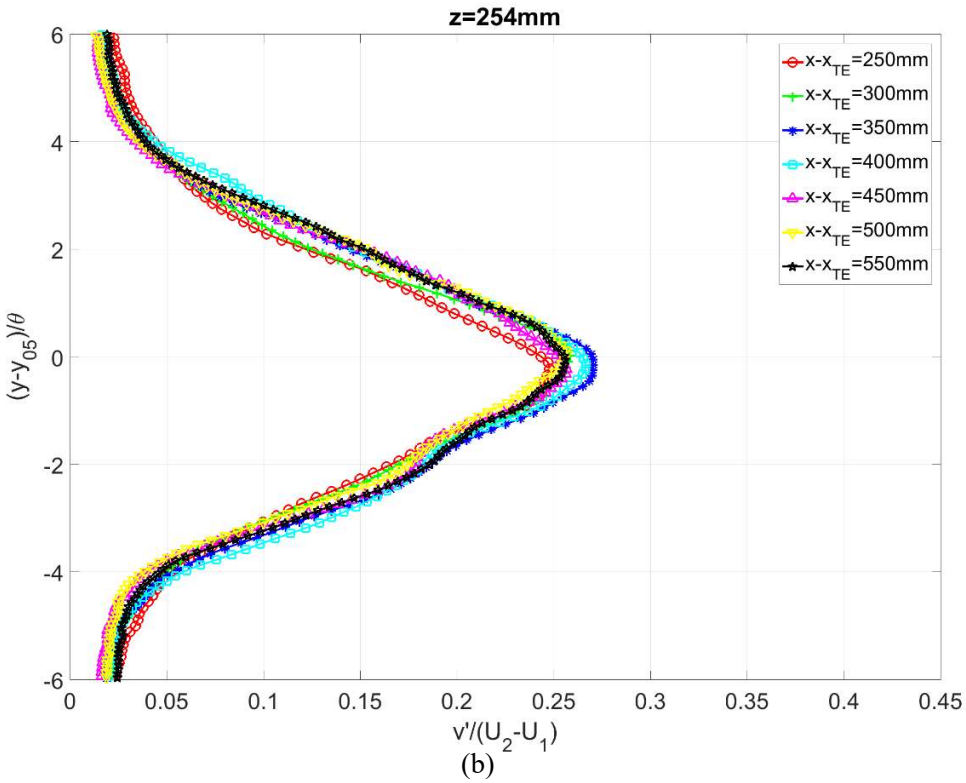
z=254mm
x-x_TE=250mm
x-x_TE=300mm
x-x_TE=350mm
x-x_TE=400mm
x-x_TE=450mm
x-x_TE=500mm
x-x_TE=550mm
(y-y_05)/θ
v'/(U_2-U_1)
6
4
2
0
-2
-4
-6
0
0.05
0.1
0.15
0.2
0.25
0.3
0.35
0.4
0.45

(b)

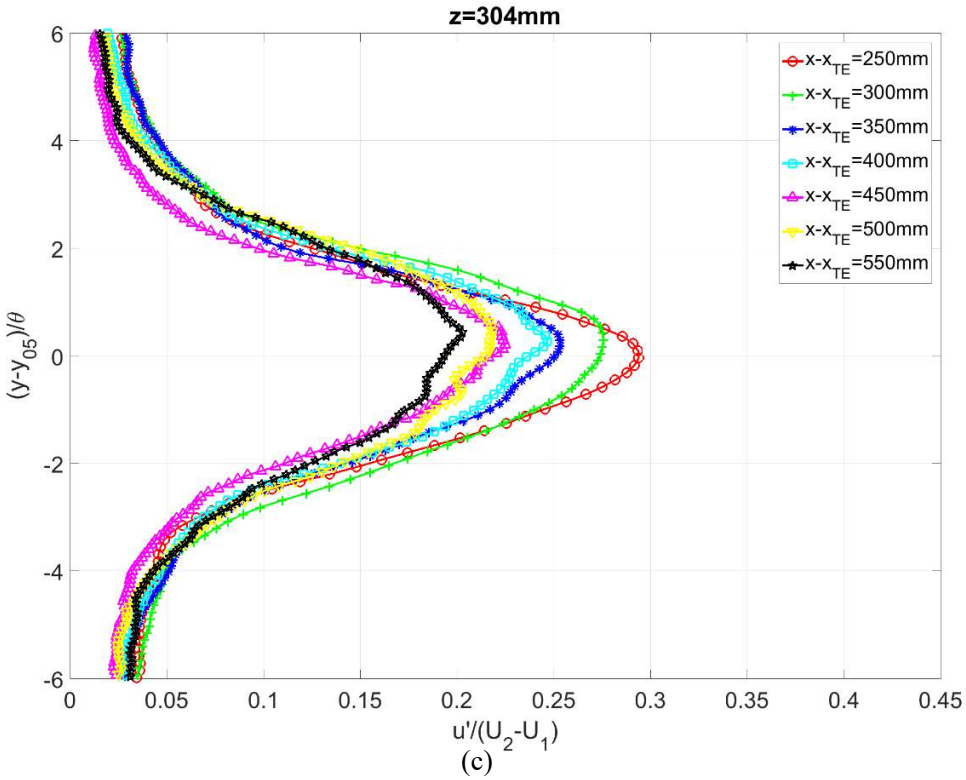
z=304mm
x-x_TE=250mm
x-x_TE=300mm
x-x_TE=350mm
x-x_TE=400mm
x-x_TE=450mm
x-x_TE=500mm
x-x_TE=550mm
(y-y_05)/θ
u'/(U_2-U_1)

(c)

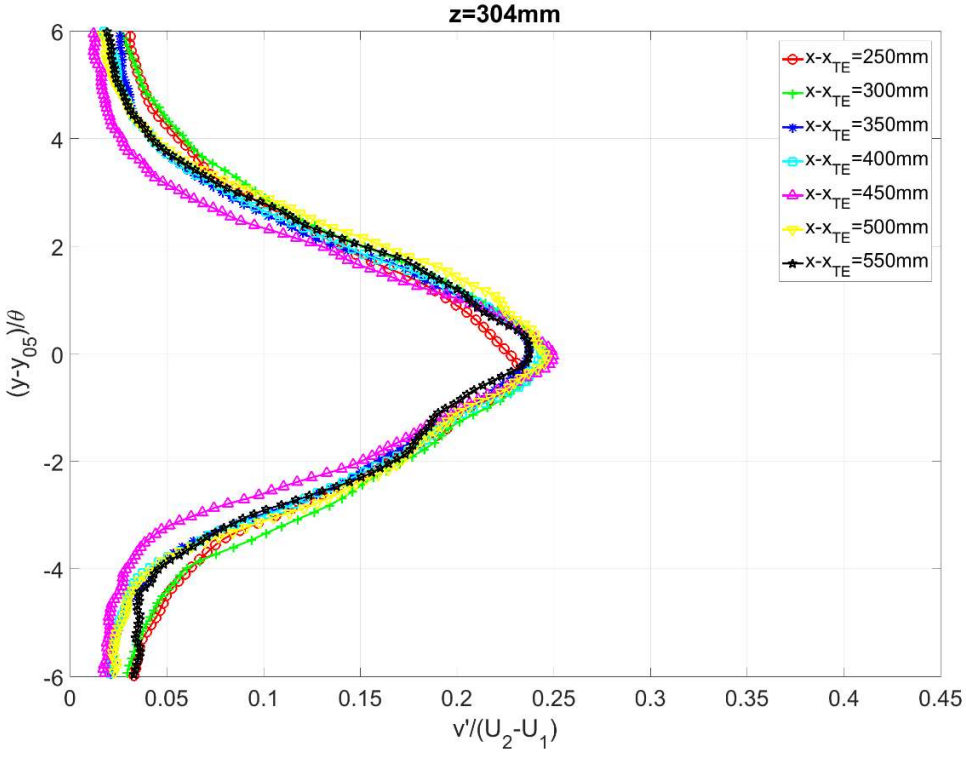
z=304mm
x-x_TE=250mm
x-x_TE=300mm
x-x_TE=350mm
x-x_TE=400mm
x-x_TE=450mm
x-x_TE=500mm
x-x_TE=550mm
(y-y_05)/θ
v'/(U_2-U_1)

(d)

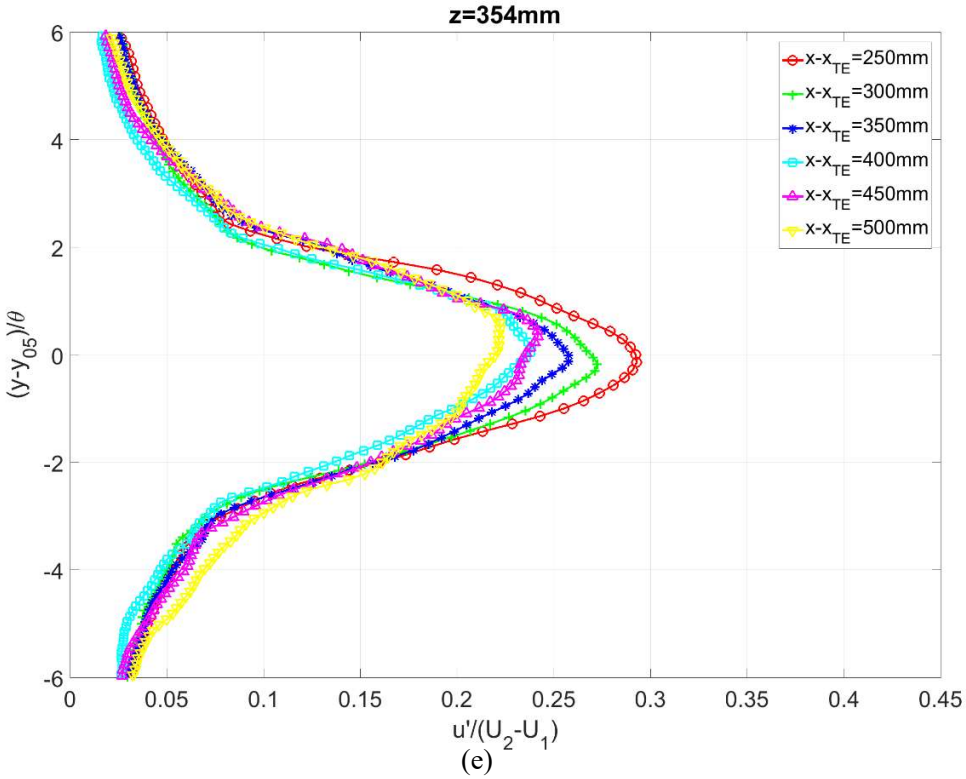

(e)

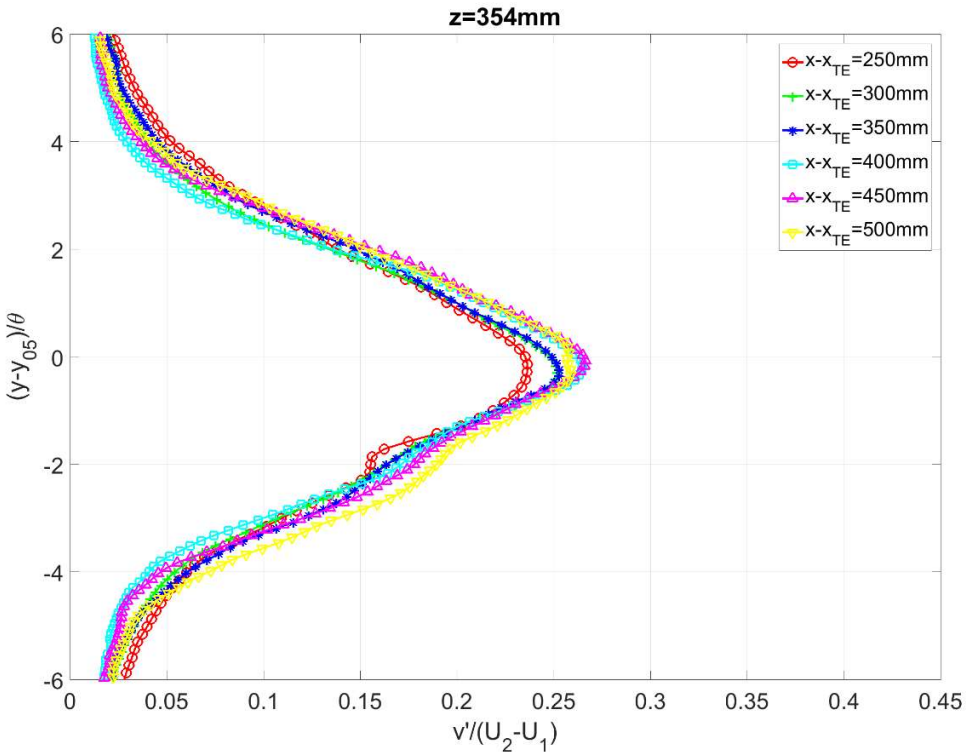

(f)

Figure 4.8: Turbulent intensities of u and v components at 75Hz of the oscillating frequency at (a), (b) z=254mm (c), (d) z=304mm (e), (f) z=354mm

Figures 4.8 shows the turbulent intensities for both streamwise and vertical velocity components of the swept-back wing with forcing frequency at 75 Hz for three spanwise locations (z = 254mm, 304mm, 354mm). When comparing Figures 4.8 with results for f = 50 Hz (Figures 4.7) the turbulent intensity profiles are not in a smooth parabolic fashion. The maximum intensity of the streamwise component $\overline{u'^2}^{1/2}$ increases with spanwise distance but decreases downstream. Figures 4.8(a), (c), and (e) further highlight for $250\ mm < x - x_{TE} < 450mm$, the maximum intensity of the streamwise component $\overline{u'^2}^{1/2}$ ranges from 0.2 to 0.3 throughout wingspan. According to Oster and Wygnanski (1982), if the distribution of $\overline{u'^2}^{1/2}$ has a characteristic bell shape or a double-peak shape, it suggests that the flow is either a Region I or Region II type mixing layer flow respectively. In this respect, the data shown from Figures 4.8 indicates that the flow is neither Region I nor Region II mixing layer flow.

The vertical component of turbulent intensity $\overline{v'^2}^{1/2}$ remains constant at 0.25 for all spanwise locations which is larger than that for f = 50 Hz. In addition, for downstream region of $x - x_{TE} > 300mm$, the vertical component intensity profiles appear to be self-similar for all spanwise locations. The peak of the maximum intensity is located at y equal to y_{05}, this meant the center of mixing layer has greatest turbulent intensity. Both streamwise and vertical velocity components for f = 75 Hz behave inversely compared to respective components for f = 50 Hz. A Region II type mixing layer flow's vertical velocity component $\overline{v'^2}^{1/2}$ behaves similar to vertical turbulent intensity for f = 75 Hz. However, previous results have shown that an excitation frequency of f = 75 Hz, the turbulent mixing layer flow becomes overamplified such that it cannot be categorized as Region I or Region II type.

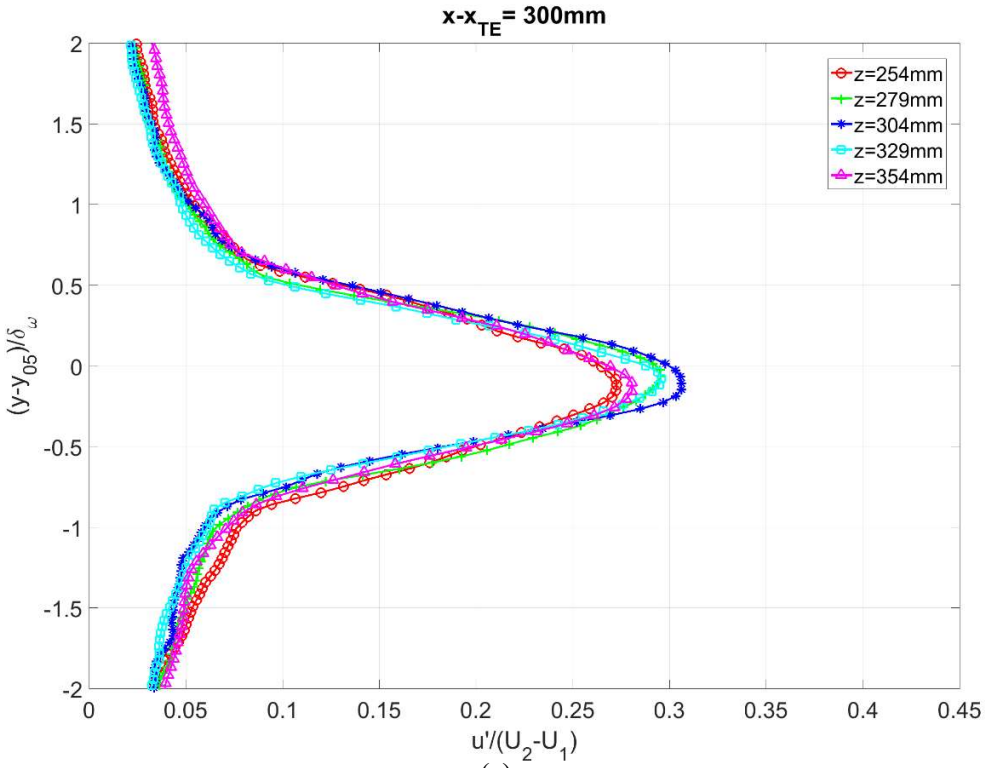
x-x_TE= 300mm
z=254mm
z=279mm
z=304mm
z=329mm
z=354mm
(y-y_05)/δ_ω
u'/(U_2-U_1)

(a)

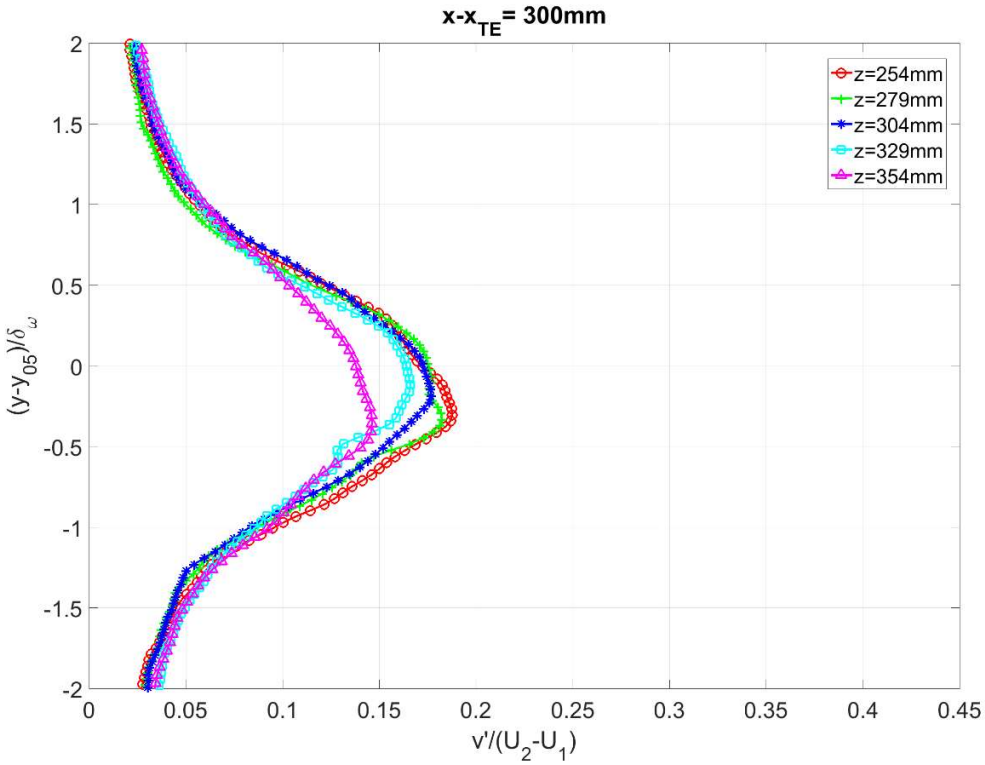
x-x_TE= 300mm
z=254mm
z=279mm
z=304mm
z=329mm
z=354mm
(y-y_05)/δ_ω
v'/(U_2-U_1)

(b)

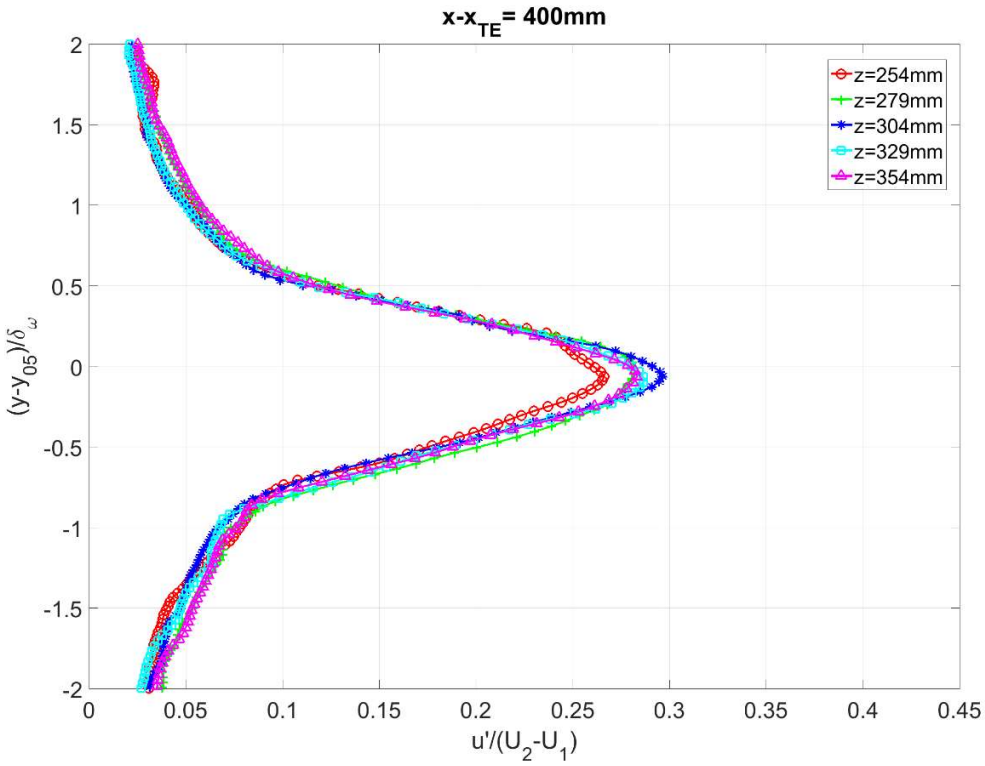
x-x_TE= 400mm
z=254mm
z=279mm
z=304mm
z=329mm
z=354mm
(y-y_05)/δ_ω
u'/(U_2-U_1)

(c)

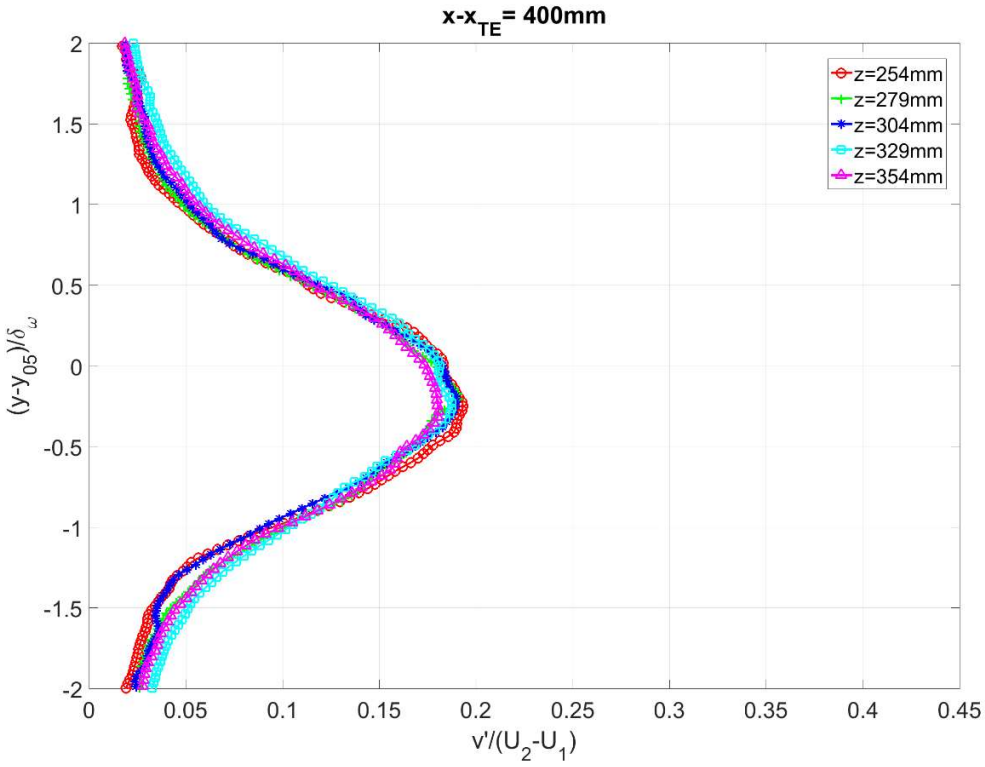
x-x_TE= 400mm
z=254mm
z=279mm
z=304mm
z=329mm
z=354mm
(y-y_05)/δ_ω
v'/(U_2-U_1)

(d)

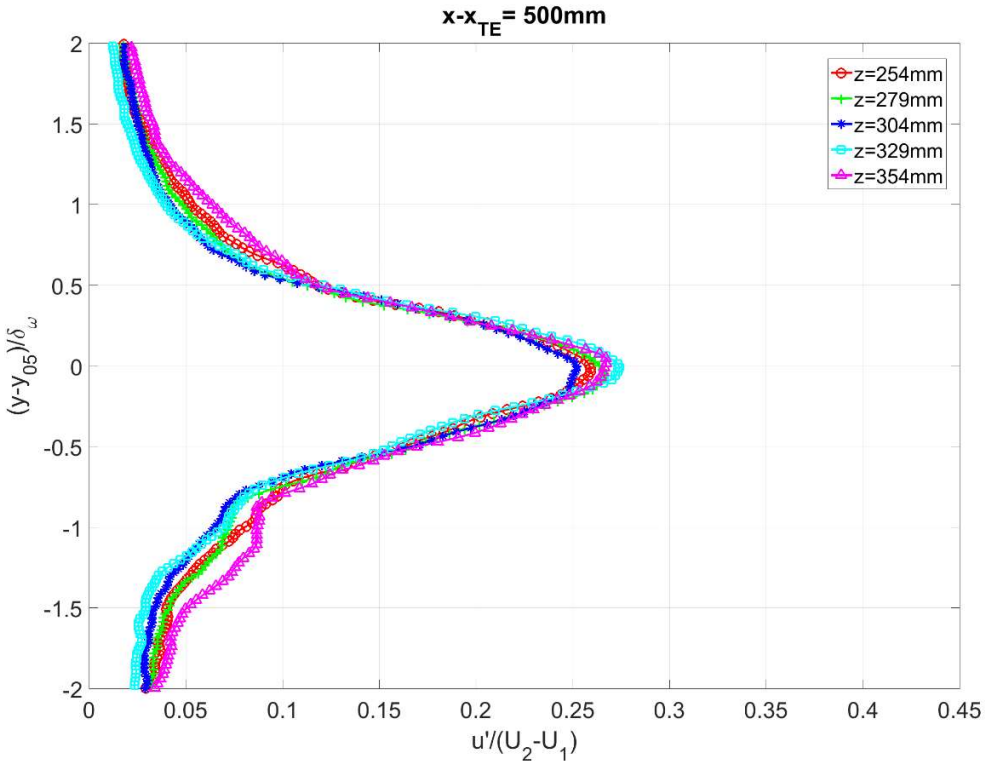
x-x_TE= 500mm
z=254mm
z=279mm
z=304mm
z=329mm
z=354mm
(y-y_05)/δ_ω
u'/(U_2-U_1)

(e)

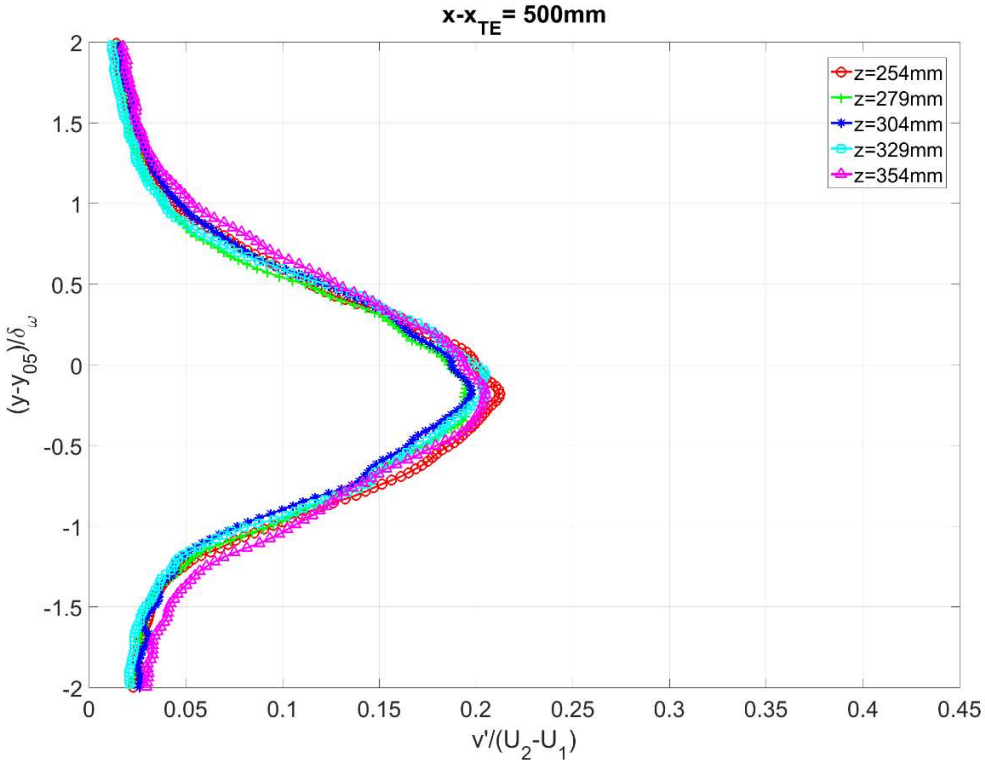
x-x_TE= 500mm
z=254mm
z=279mm
z=304mm
z=329mm
z=354mm
(y-y_05)/δ_ω
v'/(U_2-U_1)

(f)

Figure 4.9: Turbulent intensities of u and v components in the direction parallel to the trailing edge at 50Hz of the oscillating frequency at (a), (b) $x - x_{TE} = 300mm$ (c), (d) $x - x_{TE} = 400mm$ (e), (f) $x - x_{TE} = 500mm$

Figures 4.9 shows the turbulent intensities for both streamwise and lateral components with forcing frequency at 50 Hz for three trailing edge locations ($x - x_{TE}$ = 300mm, 400mm, 500mm). Although both turbulent intensity plots of $\overline{u'^2}^{1/2}$ and $\overline{v'^2}^{1/2}$ share the same bell-shaped curve, turbulent intensity plot for streamwise component is much narrower than that of lateral turbulent intensity. At $x - x_{TE} = 500mm$ and $-1.5 < y - y_{05}/\delta_\omega < -1$, the streamwise turbulent intensity varies for different spanwise locations.

In addition, the turbulent intensity plots of $\overline{v'^2}^{1/2}$ remains self-similar for $x - x_{TE} > 300mm$ (Figures 4.9 (b), (d), (f)). The maximum turbulent intensity plot does not remain constant for $x - x_{TE} = 300mm$. This might be due to the wake affects located near the trailing edge.

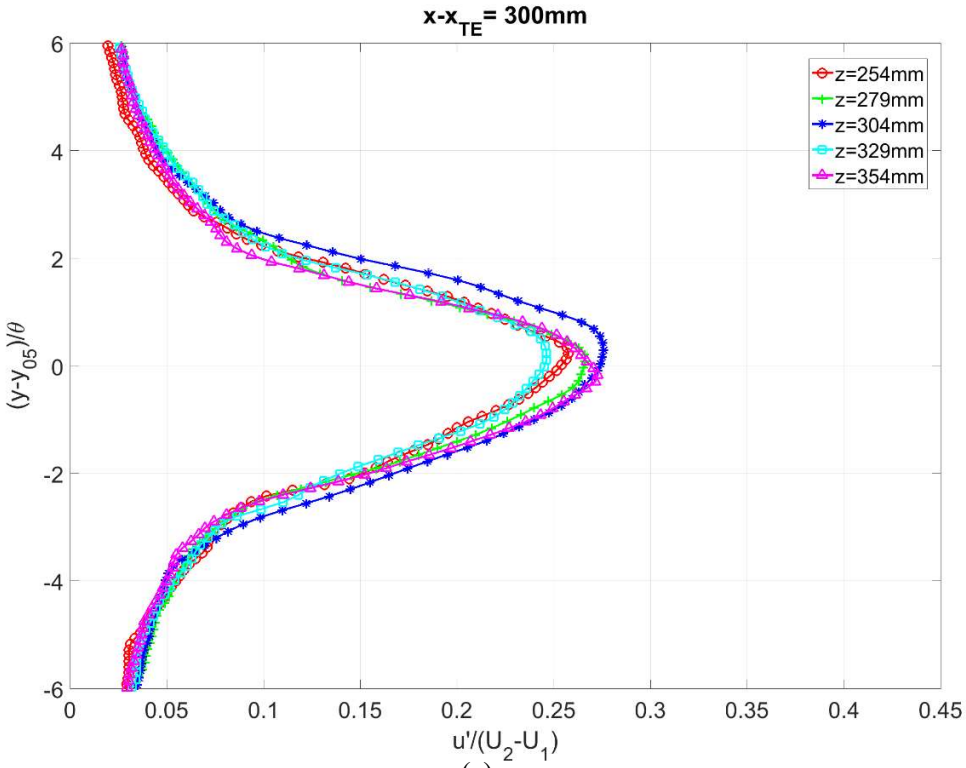
x-x_TE= 300mm
z=254mm
z=279mm
z=304mm
z=329mm
z=354mm
(y-y_05)/θ
u'/(U_2-U_1)
6
4
2
0
-2
-4
-6
0
0.05
0.1
0.15
0.2
0.25
0.3
0.35
0.4
0.45

(a)

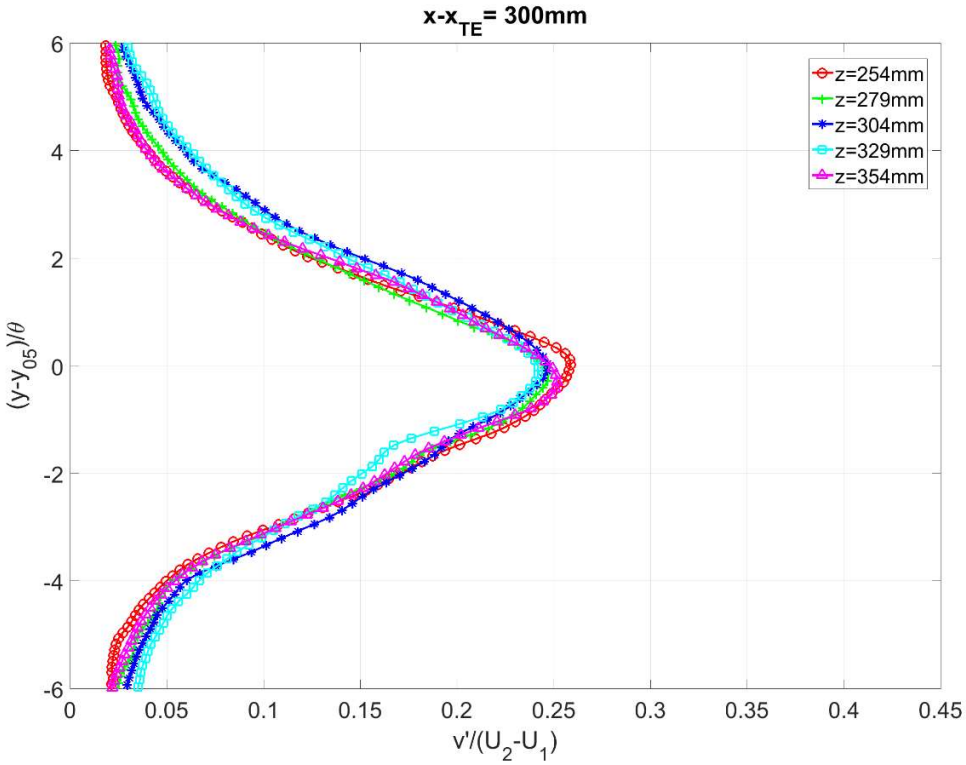
x-x_TE= 300mm
z=254mm
z=279mm
z=304mm
z=329mm
z=354mm
(y-y_05)/θ
v'/(U_2-U_1)
6
4
2
0
-2
-4
-6
0
0.05
0.1
0.15
0.2
0.25
0.3
0.35
0.4
0.45

(b)

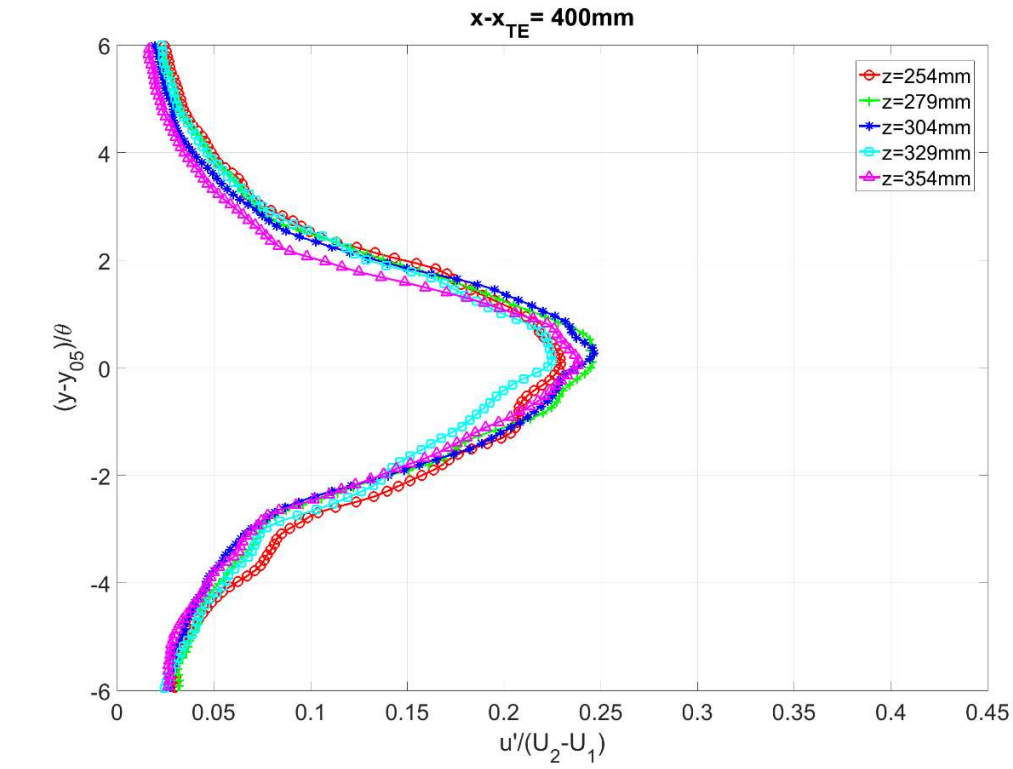
x-x_TE= 400mm
z=254mm
z=279mm
z=304mm
z=329mm
z=354mm
(y-y_05)/θ
u'/(U_2-U_1)

(c)

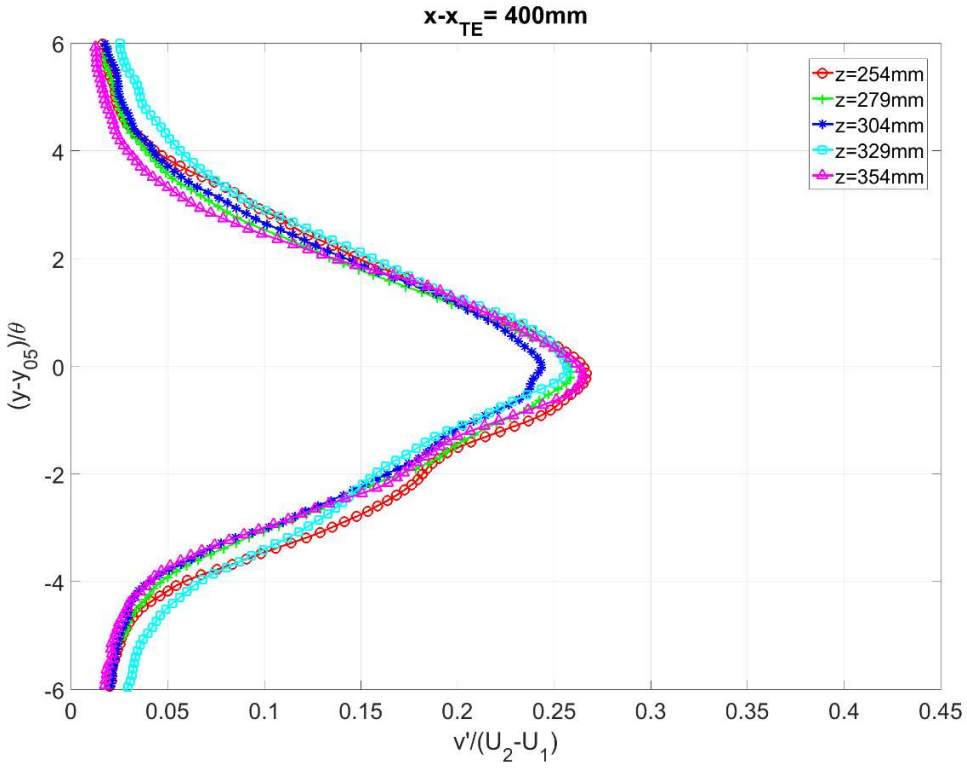
x-x_TE= 400mm
z=254mm
z=279mm
z=304mm
z=329mm
z=354mm
(y-y_05)/θ
v'/(U_2-U_1)

(d)

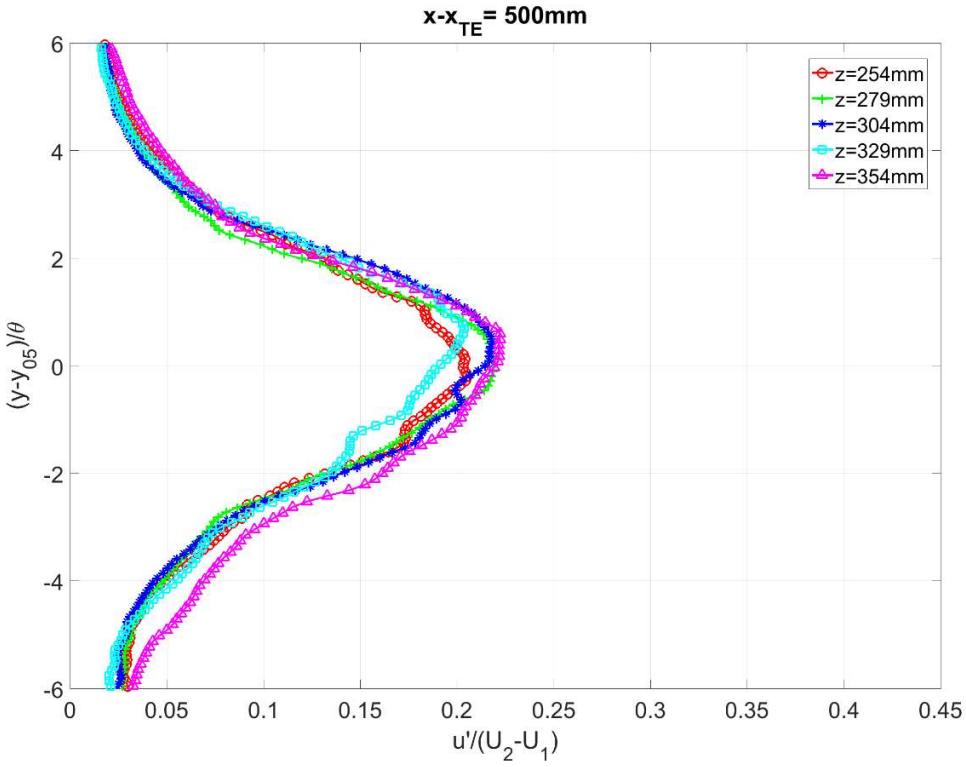
x-x_TE= 500mm
z=254mm
z=279mm
z=304mm
z=329mm
z=354mm
(y-y_05)/θ
u'/(U_2-U_1)

(e)

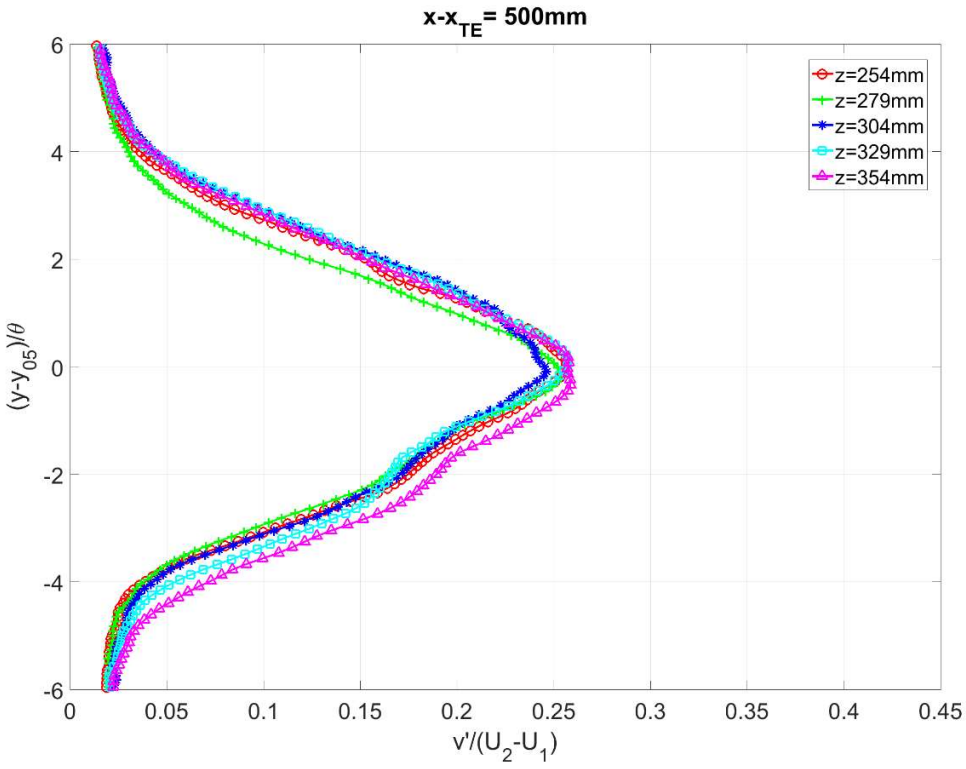
x-x_TE= 500mm
z=254mm
z=279mm
z=304mm
z=329mm
z=354mm
(y-y_05)/θ
v'/(U_2-U_1)

(f)

Figure 4.10: Turbulent intensities of u and v components in the direction parallel to the trailing edge at 75Hz of the oscillating frequency at (a), (b) $x - x_{TE} = 300mm$ (c), (d) $x - x_{TE} = 400mm$ (e), (f) $x - x_{TE} = 500mm$

Figure 4.10 shows the turbulent intensities for both streamwise and lateral components with forcing frequency at 75 Hz for three trailing edge locations ($x - x_{TE}$ = 300mm, 400mm, 500mm). Although both turbulent intensity plots of $\overline{u'^2}^{1/2}$ for f = 50 Hz and 75 Hz oscillation frequencies share the same bell-shaped curve, turbulent intensity plot for f = 75 Hz is much wider than that of 50 Hz graph. However, the turbulent intensity of $\overline{u'^2}^{1/2}$ at f = 75 Hz deteriorates as the flow travels downstream.

The turbulent intensity plots of $\overline{v'^2}^{1/2}$ with oscillation frequency of 75 Hz attains self-preserving property across the entire trailing edge. The maximum turbulent intensity of $\overline{v'^2}^{1/2}$ remains constant at 0.25 across the entire trailing edge.

4.1.5 Center location of the mixing layer

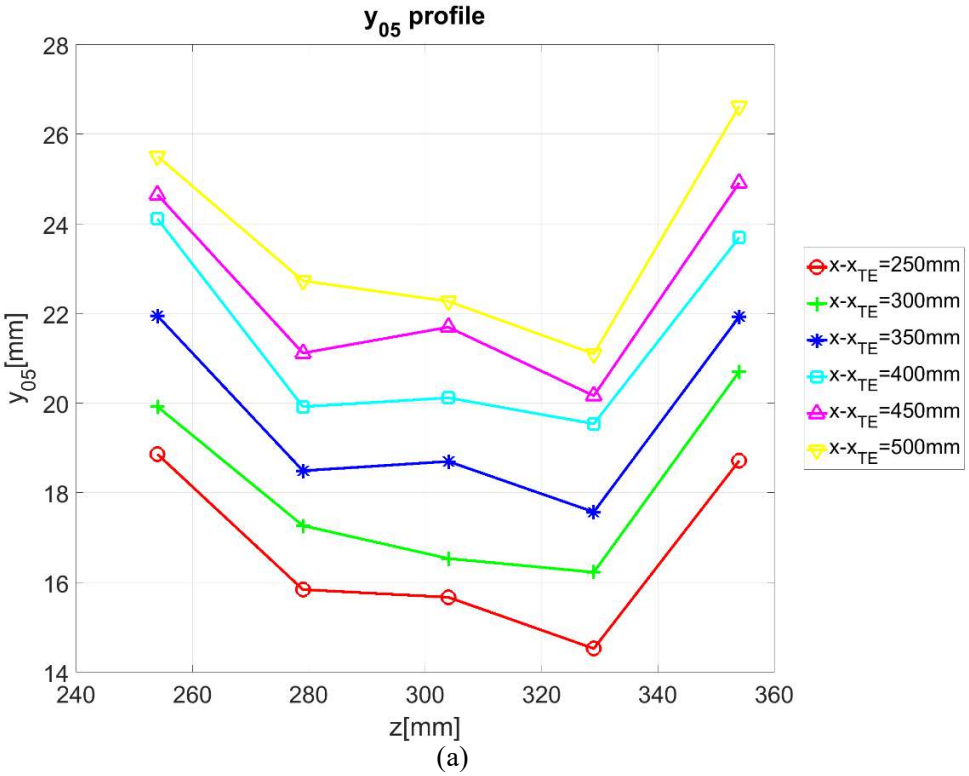

(a)

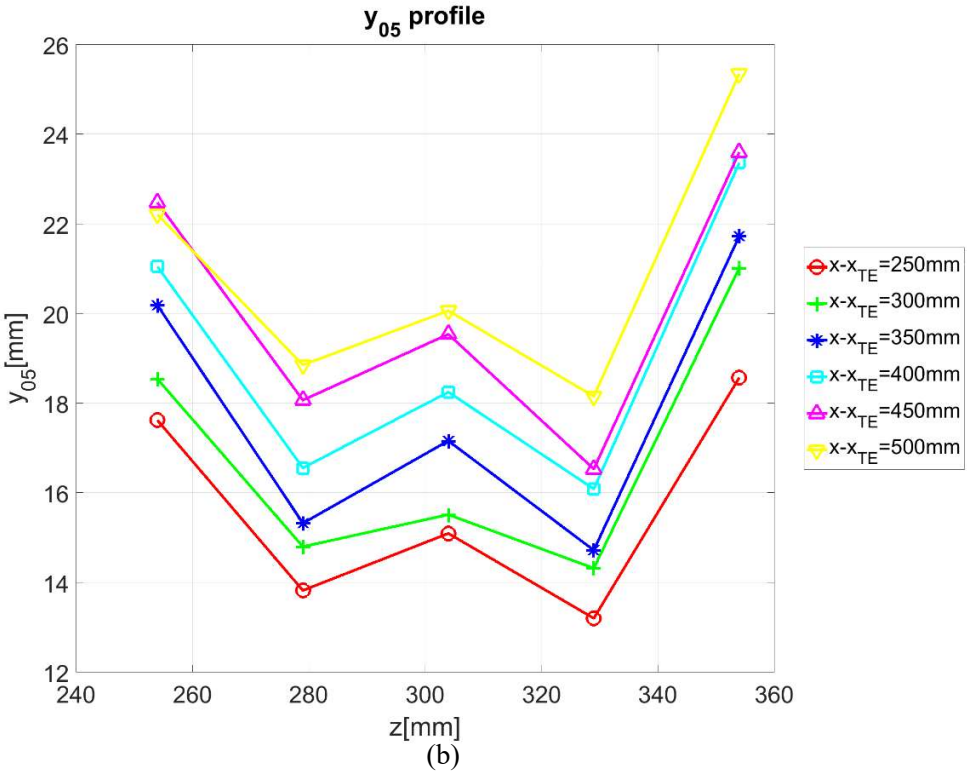

(b)

Figure 4.11: Center location profile of the mixing layer at (a) f=50Hz (b) f=75Hz

The mean local center of mixing layer (y_{05}) is defined as the location where mean velocity of mixing layer is equal to the average of both low and high-speed flow streams from tunnel nozzle. Figures 4.11 reveals the local center of mixing layer profile for both oscillation frequencies with respect to varying spanwise and trailing edge locations. Although the y_{05} profile varies throughout the entire wingspan (Figures 4.11), the mean local center increases downstream and reaches maxima points at z=254mm and z=354mm respectively. The best way to compensate the imperfection in the z-direction is using a wind tunnel with a larger spanwise width and this will reduce the wall effect especially for the center location. The y_{05} profile variation in the z-direction also will be improved by changing the aspect ratio of the test model.

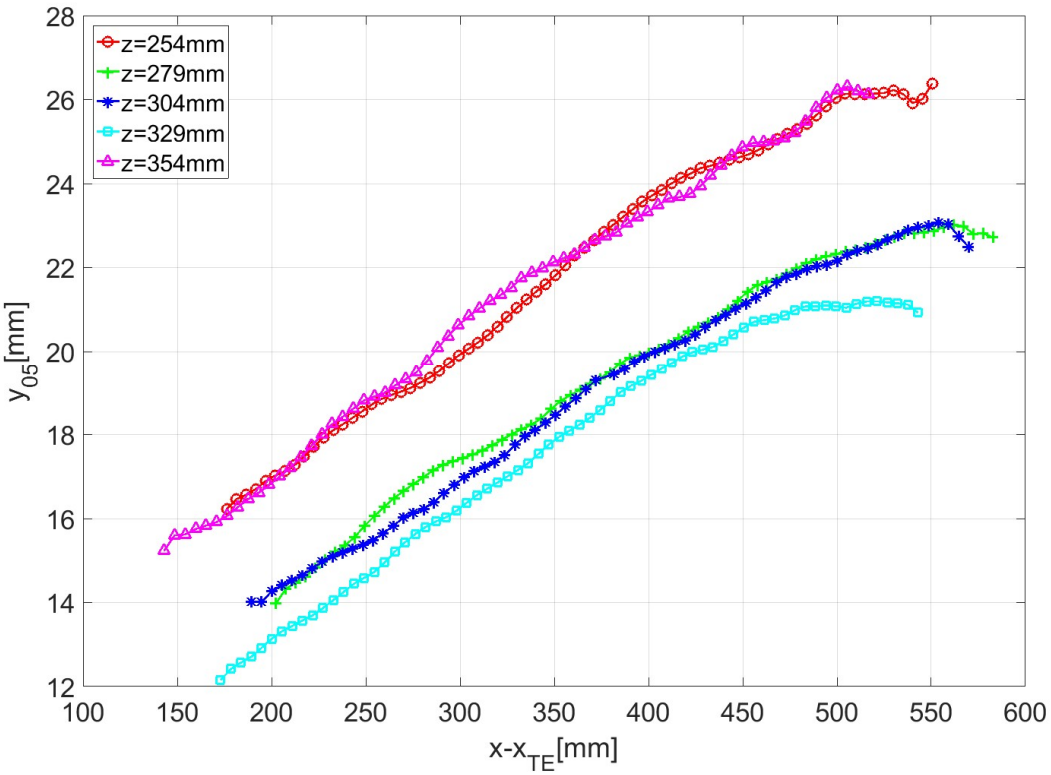

(a)

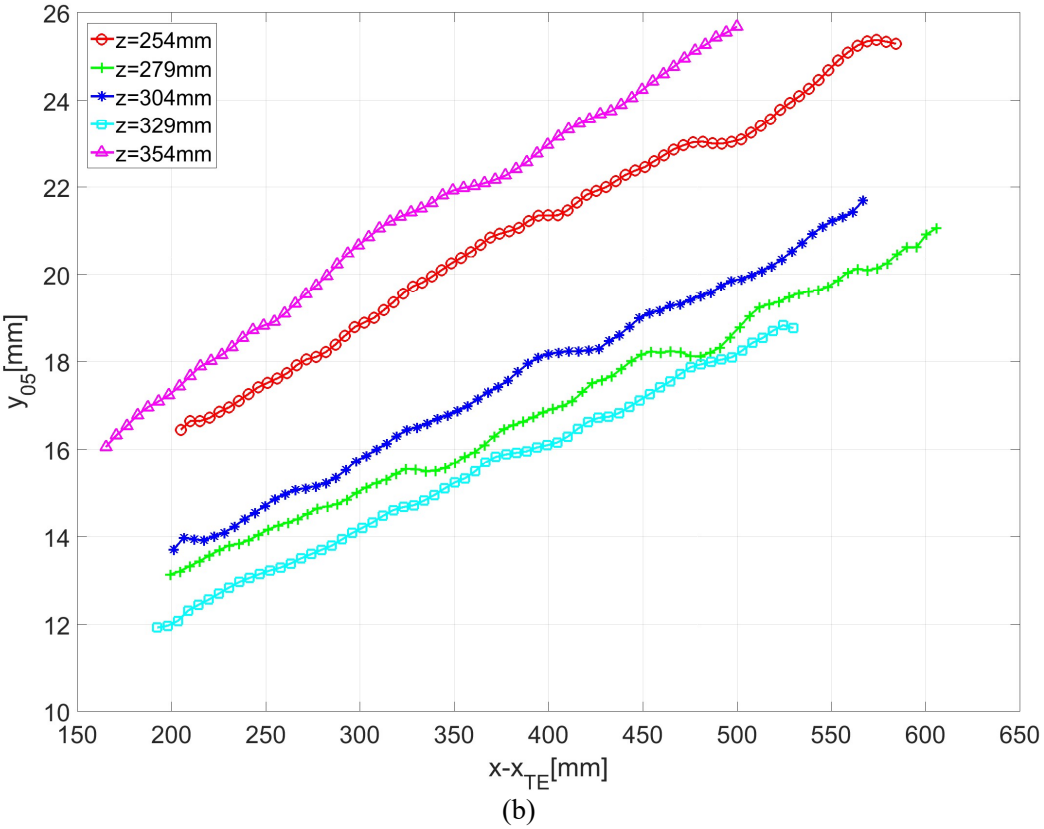

(b)

Figure 4.12: Center location profile of the mixing layer at (a) f=50Hz (b) f=75Hz

The trend that y_{05} moves toward low-speed stream with increasing downstream distance can be seen in the two-dimensional mixing layer. However, the center location of mixing layer drifts towards high-speed stream from tunnel nozzle (U_2) with increasing *x* regardless of varying oscillation frequencies and spanwise location. This implies the presence of the pressure gradient in the y-direction. The test model had negative angle of attack (-4°) and this means that the negative lift worked on the wing. This lift induced vortex which produced upwash flow behind the wing. The initial y_{05} can be explained by this induced vortex. The other possibility is that the flow is distorted with bending the streamline causes the pressure gradient.

4.2 Phase-locked sampling data

The difference would be discussed by comparing the random sampling data and the phase-locked sampling data in this section mainly. The coherent term and the random term would vanish when they are taken to be averaged. If this can be applied, then the average of random sampling frequency and the average of phase-locked sampling are equivalent to each other.

$$\overline{u_{ci}} = \overline{u_{ri}} = 0$$

The number of phase-locked data is 300 events for each phase.

4.2.1 Vorticity thickness profile and momentum thickness profile

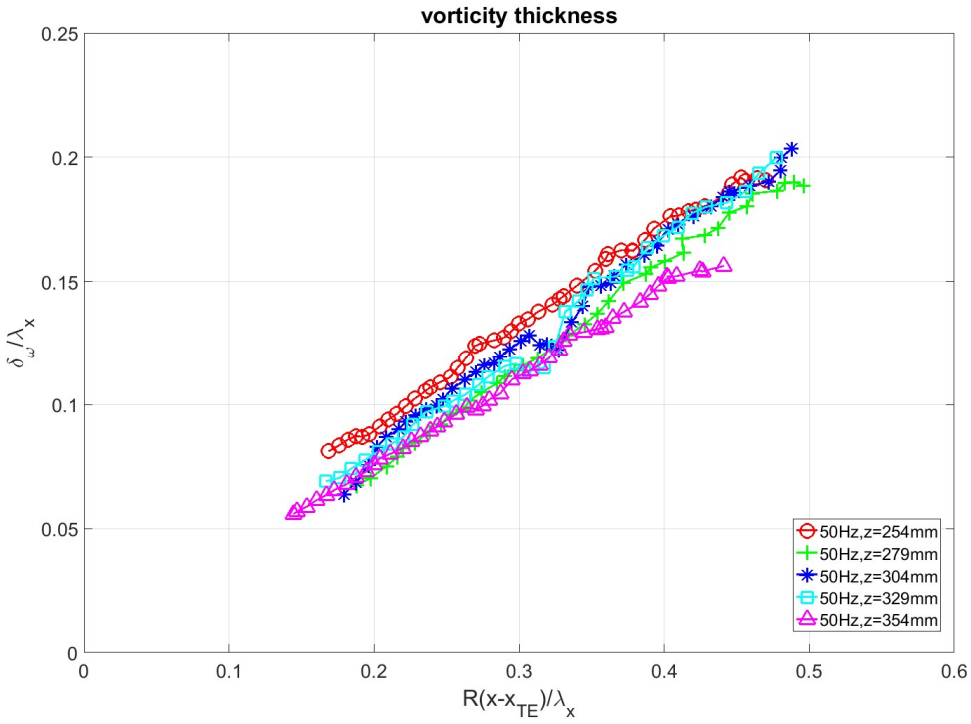

(a)

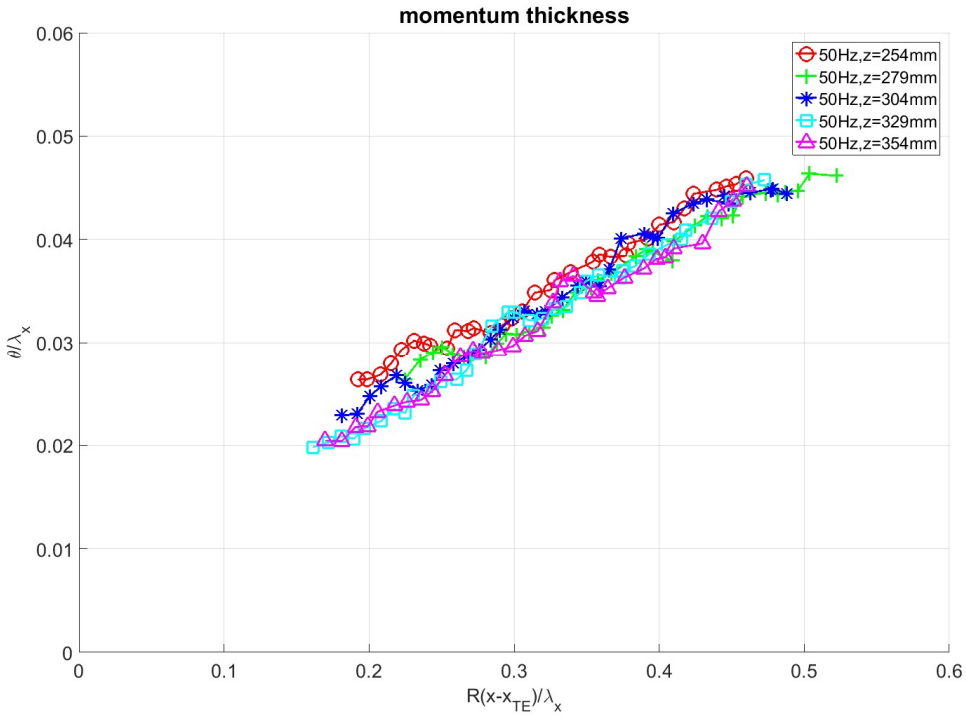
momentum thickness
50Hz,z=254mm
50Hz,z=279mm
50Hz,z=304mm
50Hz,z=329mm
50Hz,z=354mm
θ/λx
R(x-xTE)/λx
0
0.01
0.02
0.03
0.04
0.05
0.06
0.1
0.2
0.3
0.4
0.5
0.6

(b)

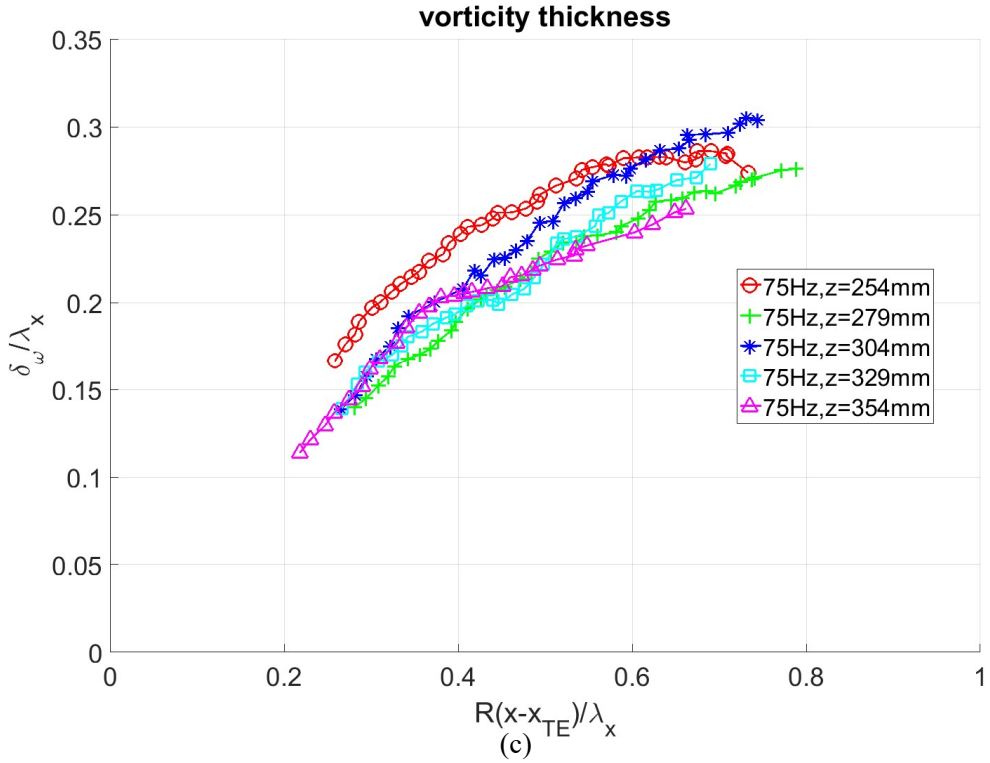
vorticity thickness
75Hz,z=254mm
75Hz,z=279mm
75Hz,z=304mm
75Hz,z=329mm
75Hz,z=354mm
δω/λx
R(x-xTE)/λx
0
0.05
0.1
0.15
0.2
0.25
0.3
0.35
0.2
0.4
0.6
0.8
1

(c)

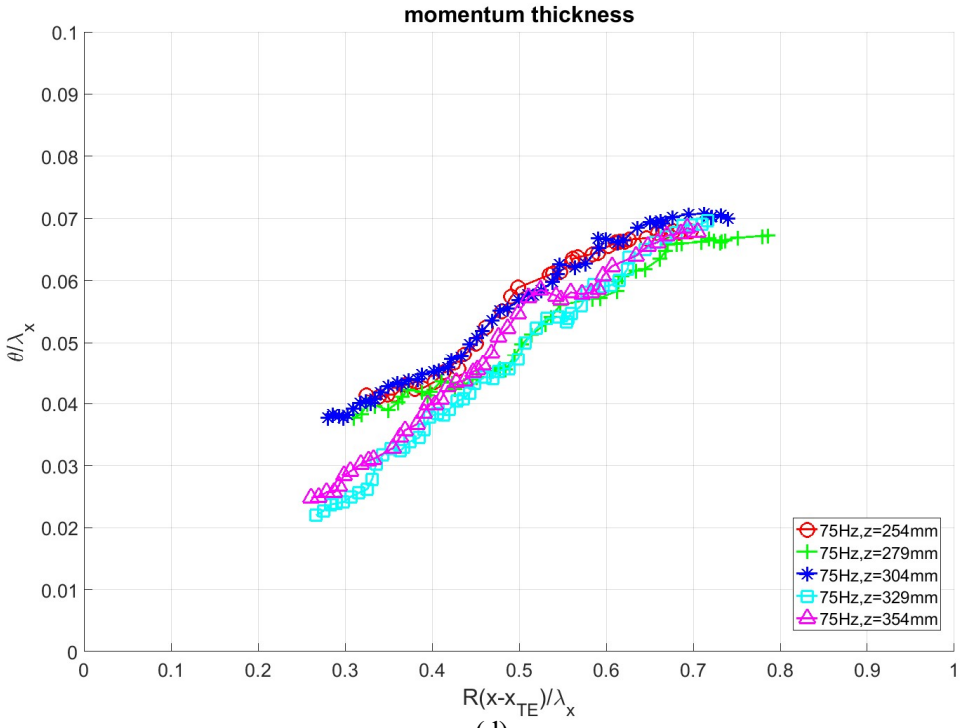

(d)

Figure 4.13: Phase-locked normalized growth rate of the mixing layer (a) Vorticity thickness with forcing frequency of f=50Hz (b) Momentum thickness with forcing frequency of f=50Hz (c) Vorticity thickness with forcing frequency of f=75Hz (d) Momentum thickness with forcing frequency of f=75Hz

The vorticity thickness profiles and the momentum thickness profiles of the phase-locked sampling data look very similar to those of the random sampling data. One of the trends that the vorticity thickness and momentum thickness at 50 Hz grow linearly along the trailing edge is the same as the Figure 4.2(a) and (b).

4.2.2 Mean velocity profile

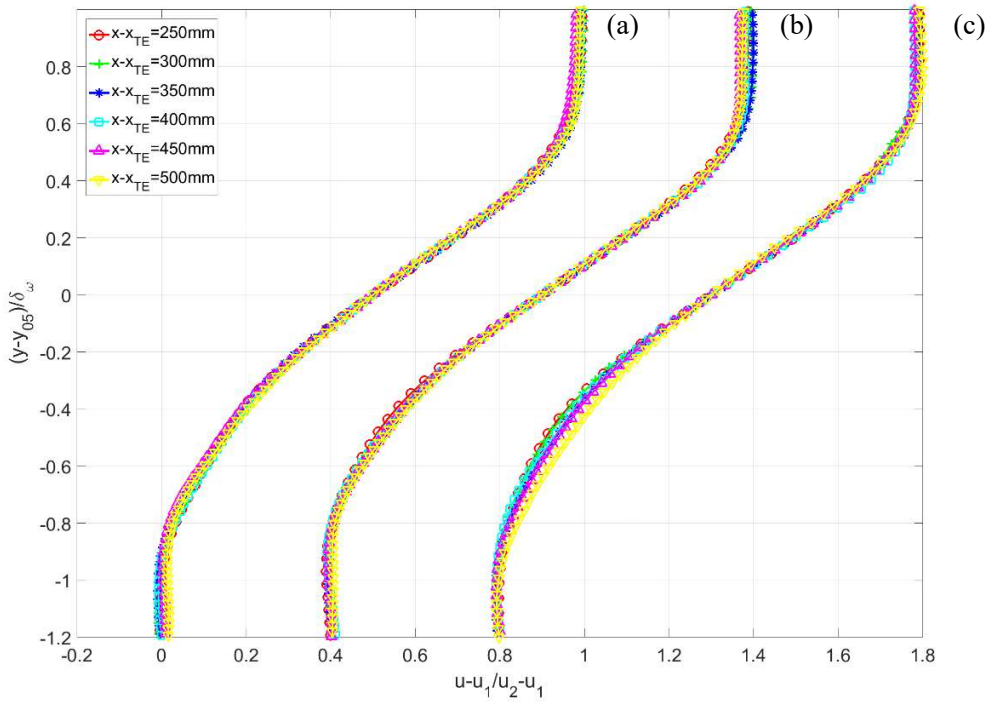

Figure 4.14: Mean velocity profiles parallel to the free stream at 50Hz of oscillating frequency nondimensionalized by vorticity thickness (a) z=254mm (b) z=304mm (c) z=354mm

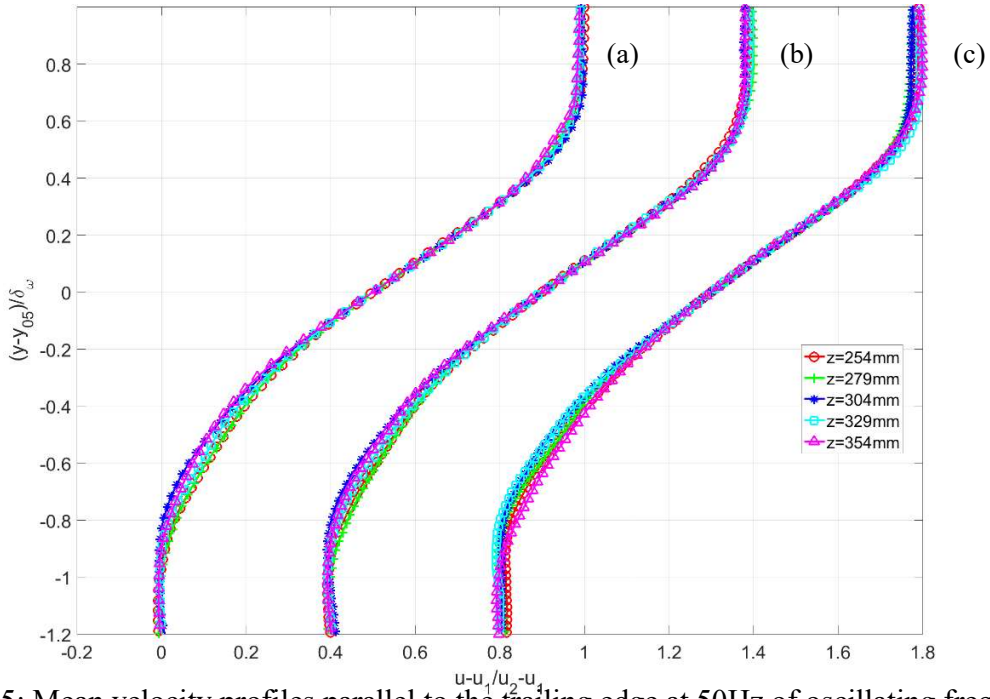

Figure 4.15: Mean velocity profiles parallel to the trailing edge at 50Hz of oscillating frequency nondimensionalized by vorticity thickness (a) $x - x_{TE} = 300mm$ (b) $x - x_{TE} = 400mm$ (c) $x - x_{TE} = 500mm$

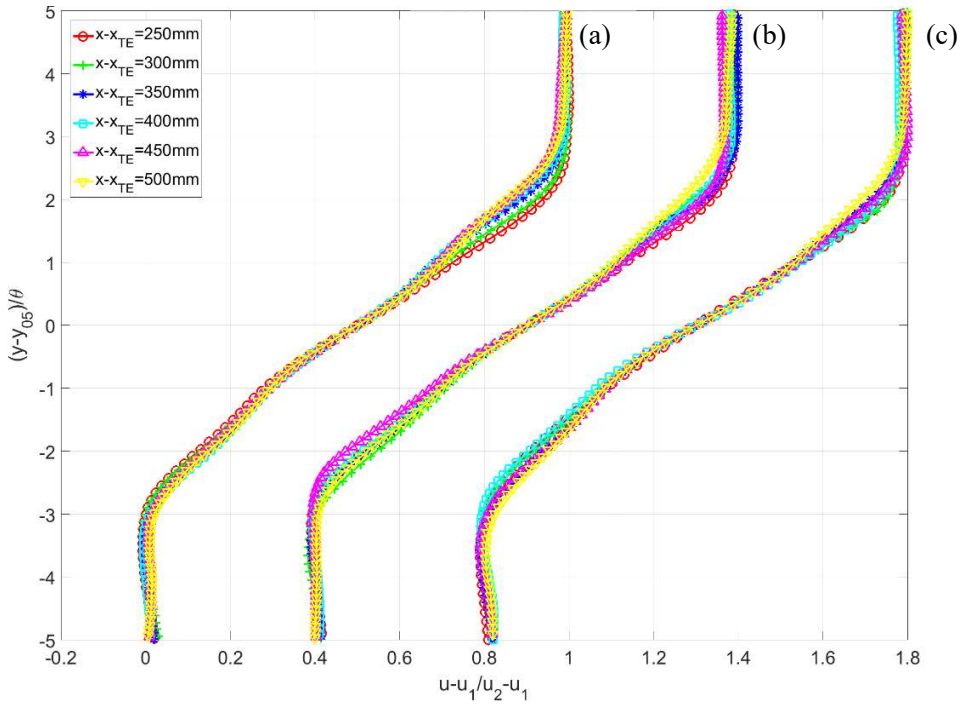

Figure 4.16: Mean velocity profiles parallel to the free stream at 75Hz of oscillating frequency nondimensionalized by vorticity thickness (a) z=254mm (b) z=304mm (c) z=354mm

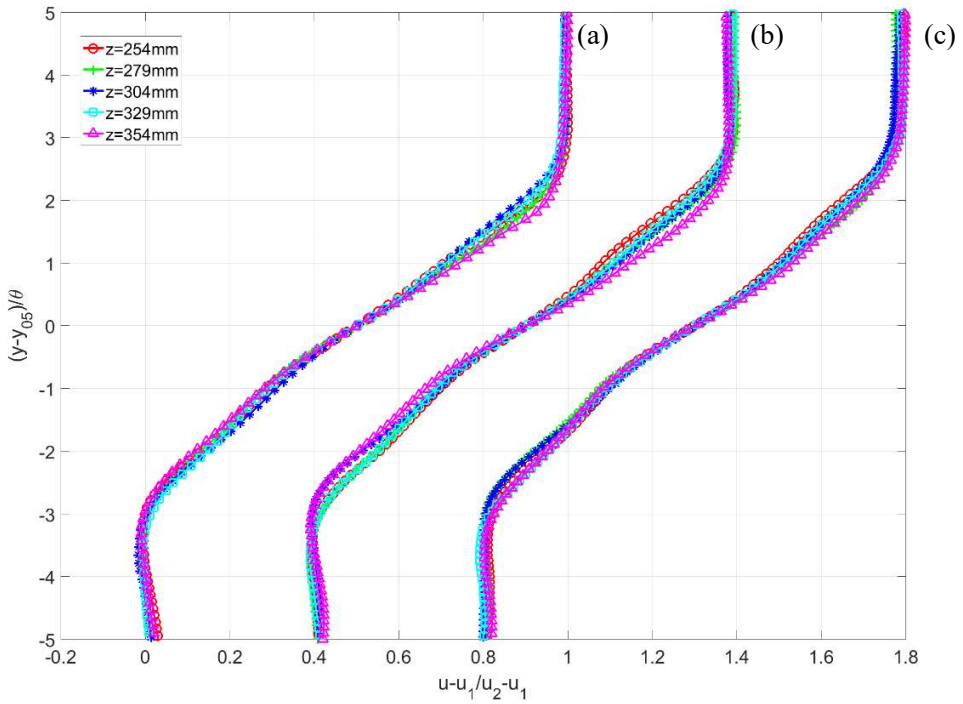

Figure 4.17: Mean velocity profiles parallel to the trailing edge at 75Hz of oscillating frequency nondimensionalized by vorticity thickness (a) $x - x_{TE} = 300mm$ (b) $x - x_{TE} = 400mm$ (c) $x - x_{TE} = 500mm$

Figure 4.14 and Figure 4.16 show the mean velocity profiles of the swept-back wing with forcing frequency at 50 Hz and 75 Hz, respectively, for three spanwise locations (z = 254mm, 304mm, 354mm). Figure 4.15 and Figure 4.17 show the mean velocity profiles with the same forcing frequency for three trailing edge locations ($x - x_{TE}$ = 300mm, 400mm, 500mm). These are very similar to those of the random sampling data. One of the trends is that the mean velocity profiles at 50 Hz appear to attain self-similarities for all downstream and trailing edge locations (Figure 4.3, 4.4, 4.14, and 4.15). The other is that the mean velocity profiles at 75Hz do not attain self-similarities in both directions parallel to the trailing edge and parallel to the free stream (Figure 4.5, 4.6, 4.16, and 4.17).

4.2.3 Fluctuating velocity

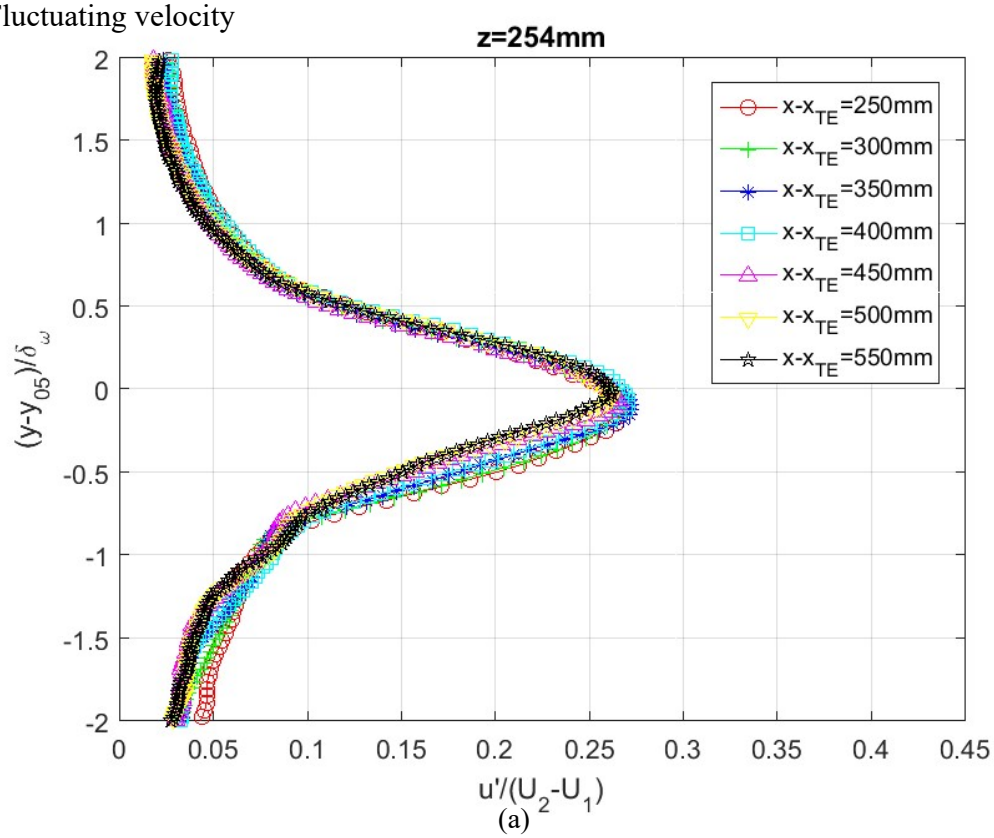

(a)

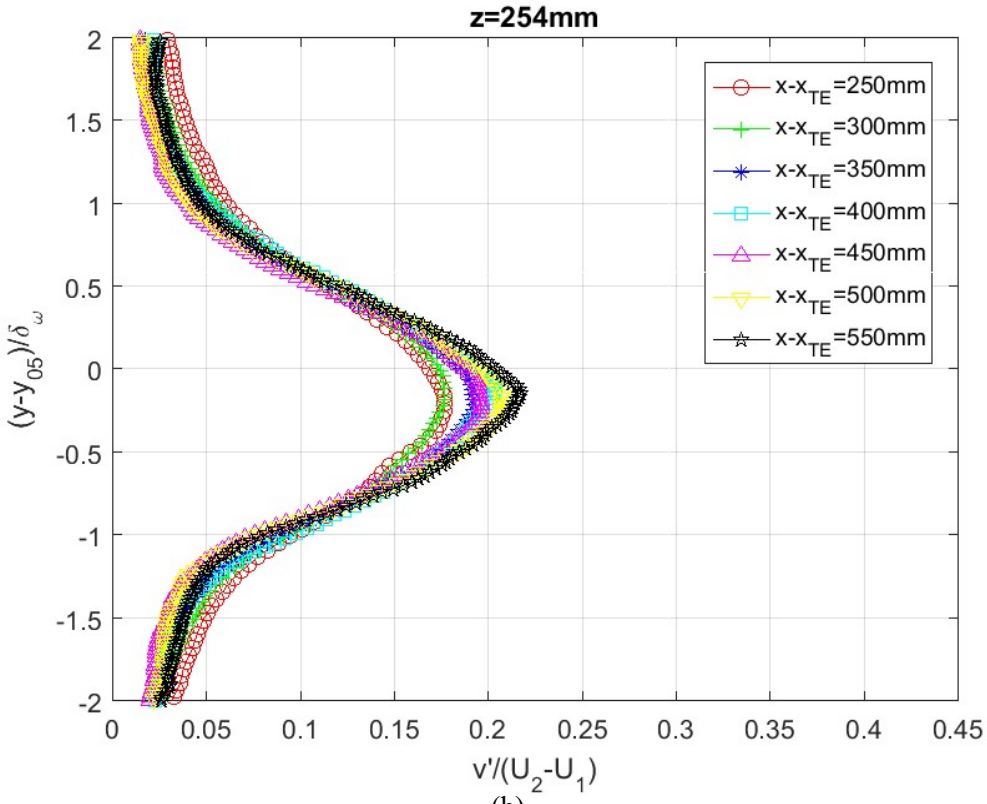

(b)

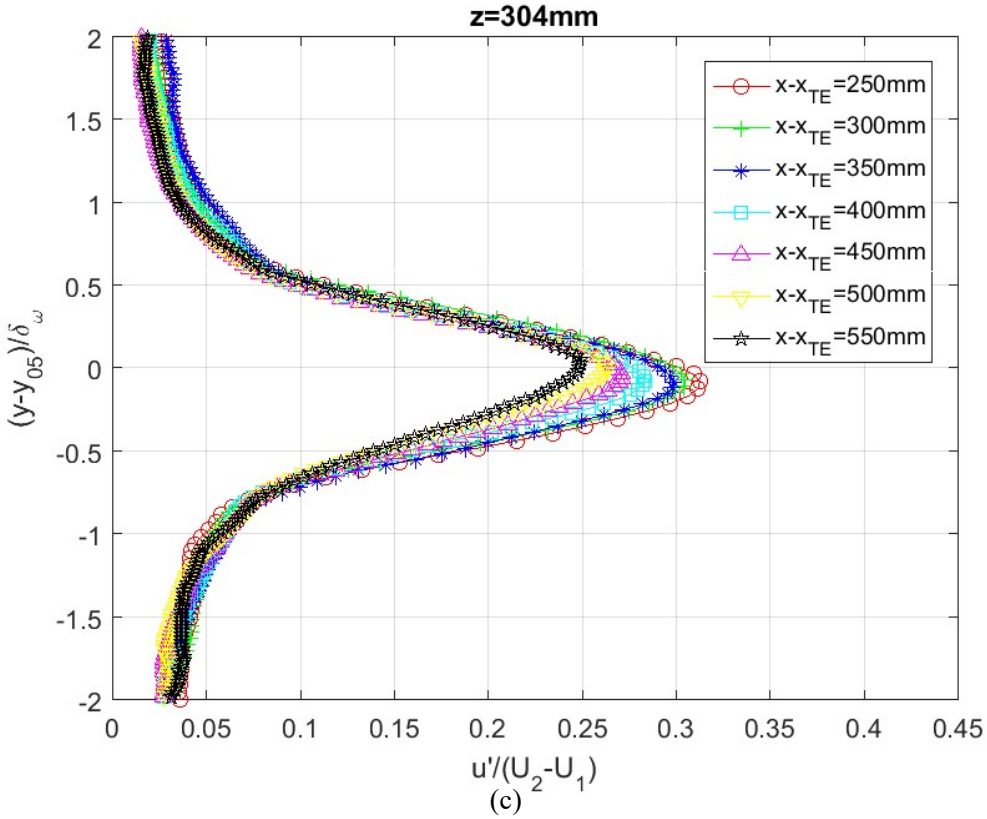
z=304mm
x-x_TE=250mm
x-x_TE=300mm
x-x_TE=350mm
x-x_TE=400mm
x-x_TE=450mm
x-x_TE=500mm
x-x_TE=550mm
(y-y_05)/δ_ω
u'/(U_2-U_1)

(c)

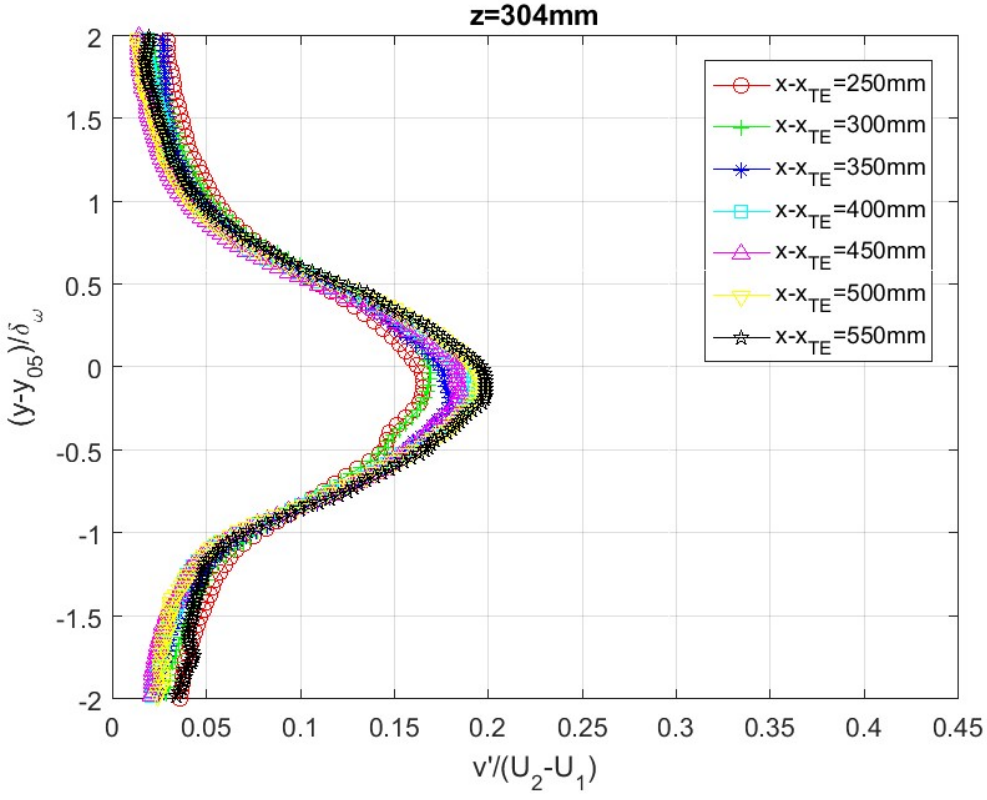
z=304mm
x-x_TE=250mm
x-x_TE=300mm
x-x_TE=350mm
x-x_TE=400mm
x-x_TE=450mm
x-x_TE=500mm
x-x_TE=550mm
(y-y_05)/δ_ω
v'/(U_2-U_1)

(d)

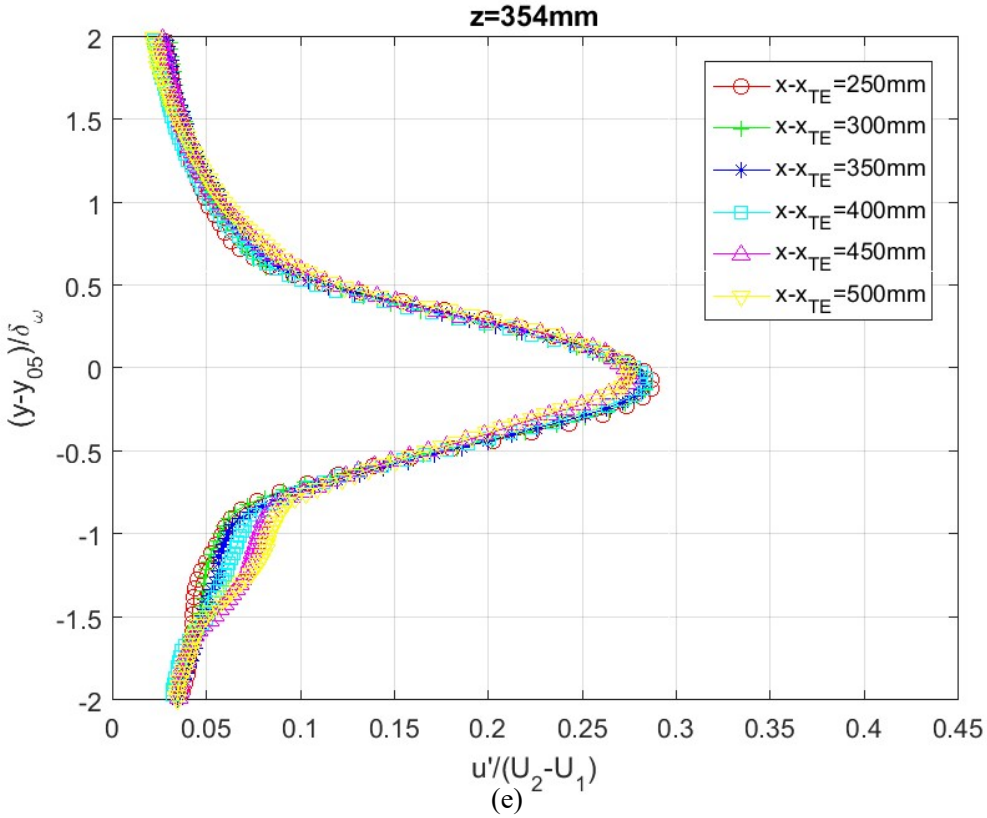

(e)

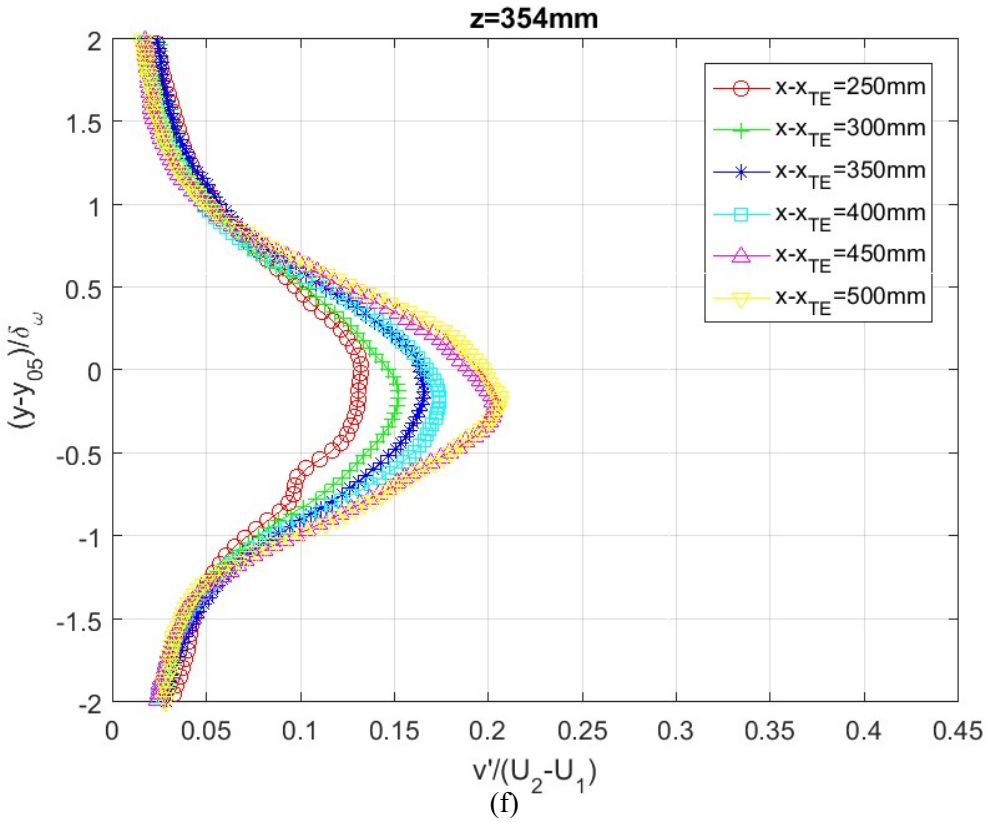

(f)

Figure 4.18: Turbulent intensities at 50Hz of the oscillating frequency at (a), (b) z=254mm (c), (d) z=304mm (e), (f) z=354mm

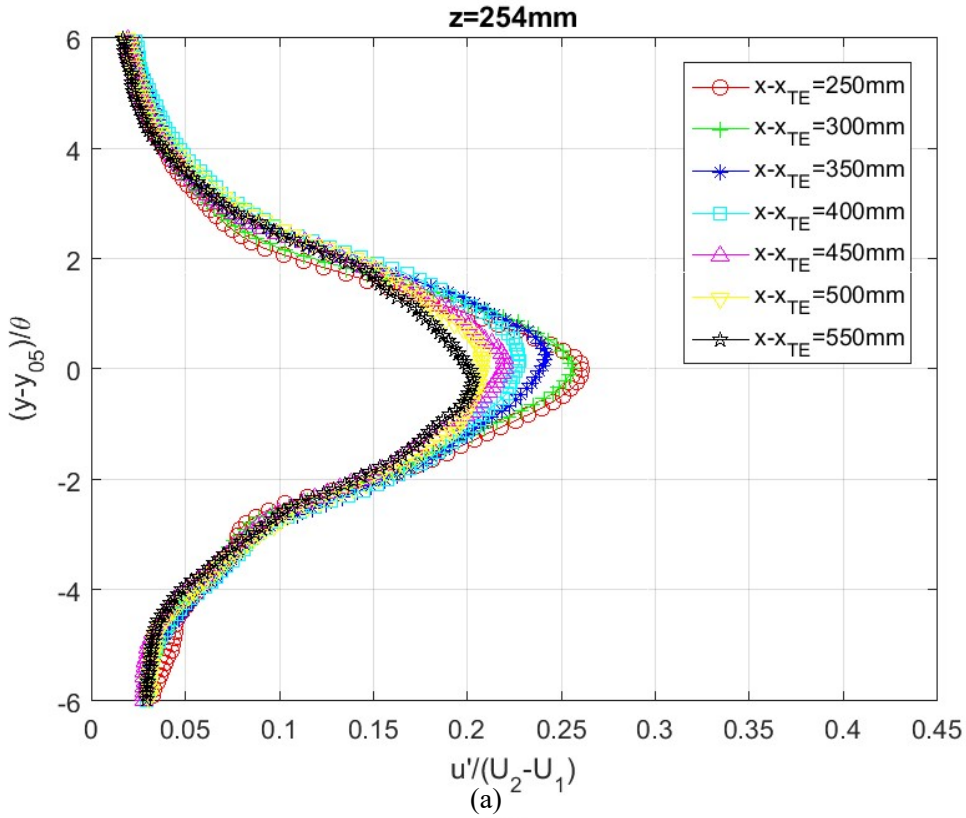
z=254mm
x-x_TE=250mm
x-x_TE=300mm
x-x_TE=350mm
x-x_TE=400mm
x-x_TE=450mm
x-x_TE=500mm
x-x_TE=550mm
(y-y_05)/θ
u'/(U_2-U_1)
6
4
2
0
-2
-4
-6
0
0.05
0.1
0.15
0.2
0.25
0.3
0.35
0.4
0.45

(a)

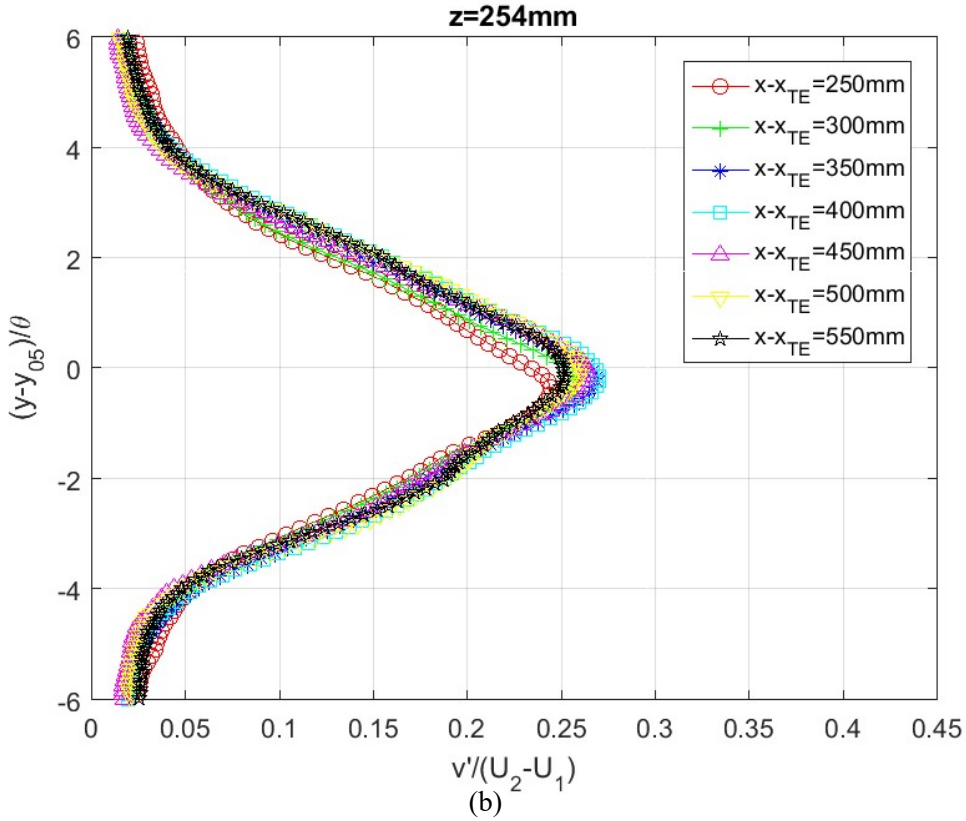
z=254mm
x-x_TE=250mm
x-x_TE=300mm
x-x_TE=350mm
x-x_TE=400mm
x-x_TE=450mm
x-x_TE=500mm
x-x_TE=550mm
(y-y_05)/θ
v'/(U_2-U_1)
6
4
2
0
-2
-4
-6
0
0.05
0.1
0.15
0.2
0.25
0.3
0.35
0.4
0.45

(b)

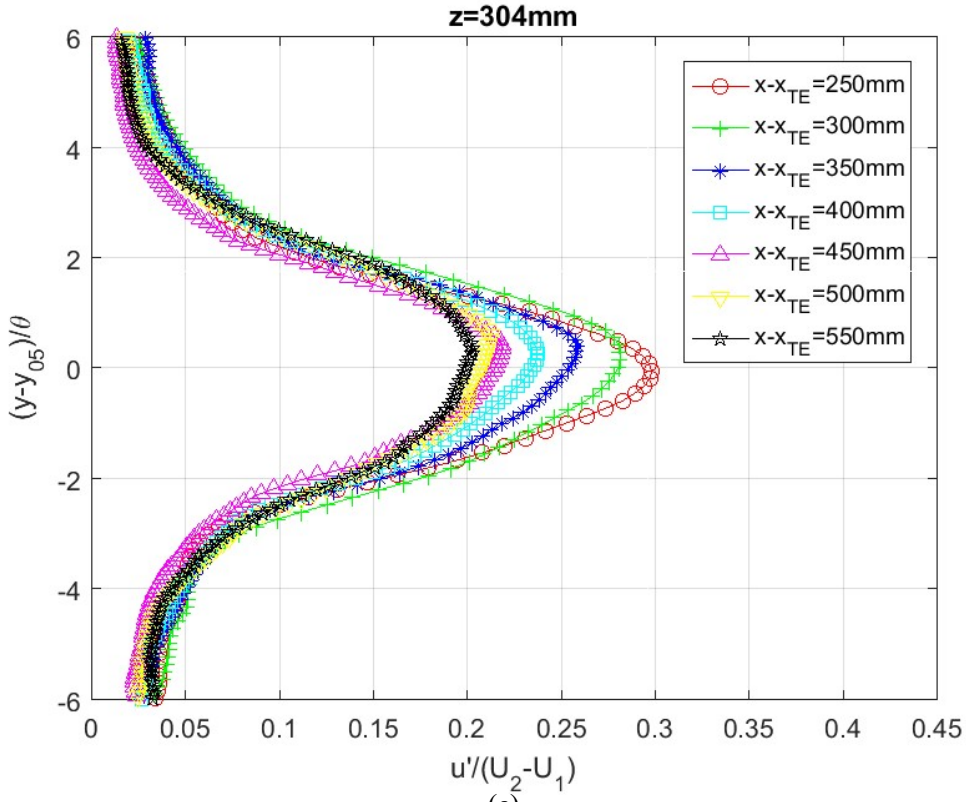
z=304mm
x-x_TE=250mm
x-x_TE=300mm
x-x_TE=350mm
x-x_TE=400mm
x-x_TE=450mm
x-x_TE=500mm
x-x_TE=550mm
(y-y_05)/θ
u'/(U_2-U_1)
6
4
2
0
-2
-4
-6
0
0.05
0.1
0.15
0.2
0.25
0.3
0.35
0.4
0.45

(c)

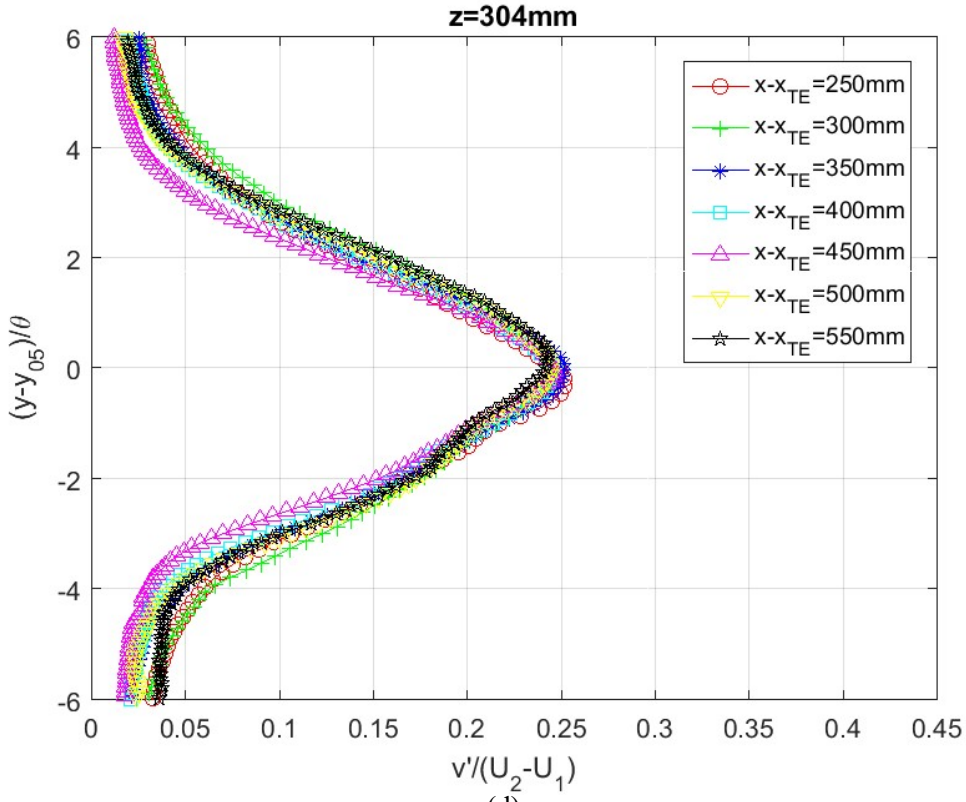
z=304mm
x-x_TE=250mm
x-x_TE=300mm
x-x_TE=350mm
x-x_TE=400mm
x-x_TE=450mm
x-x_TE=500mm
x-x_TE=550mm
(y-y_05)/θ
v'/(U_2-U_1)
6
4
2
0
-2
-4
-6
0
0.05
0.1
0.15
0.2
0.25
0.3
0.35
0.4
0.45

(d)

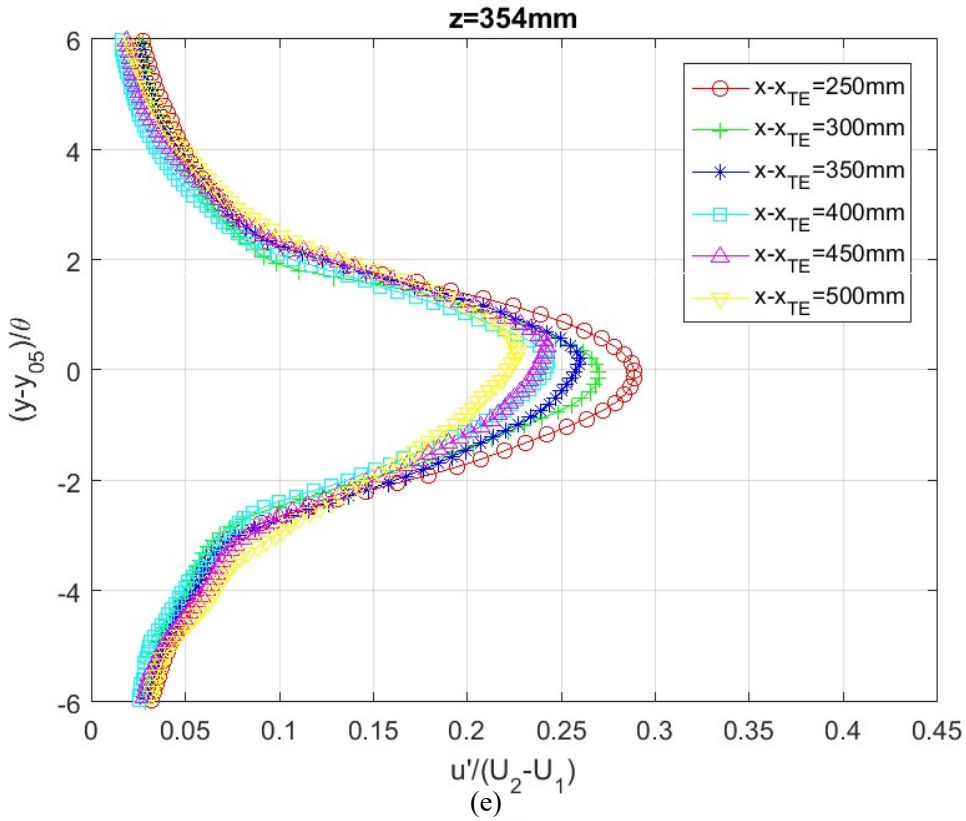

(e)

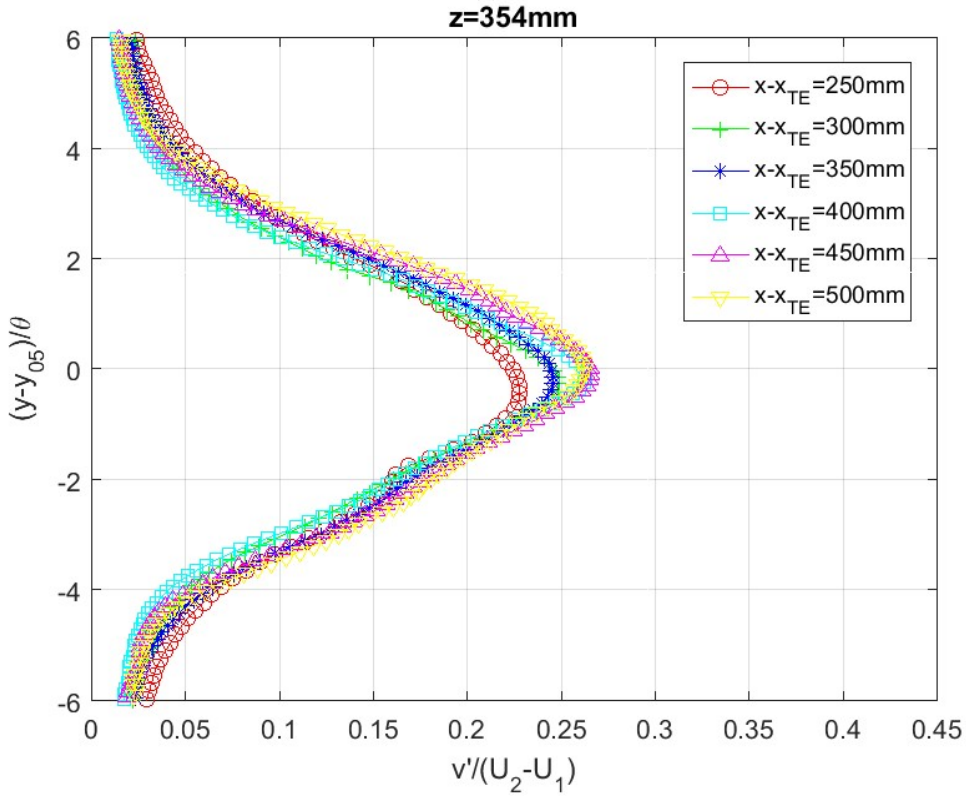

(f)

Figure 4.19: Turbulent intensities at 75Hz of the oscillating frequency at (a), (b) z=254mm (c), (d) z=304mm (e), (f) z=354mm

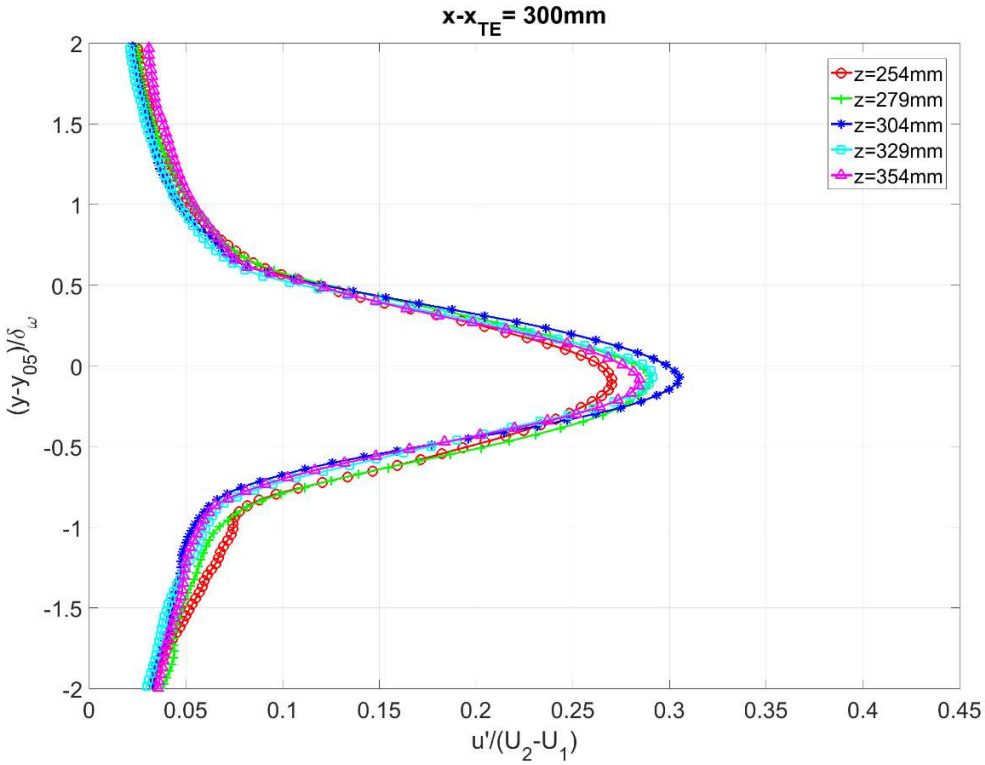
x-x_TE= 300mm
z=254mm
z=279mm
z=304mm
z=329mm
z=354mm
(y-y_05)/δ_ω
u'/(U_2-U_1)

(a)

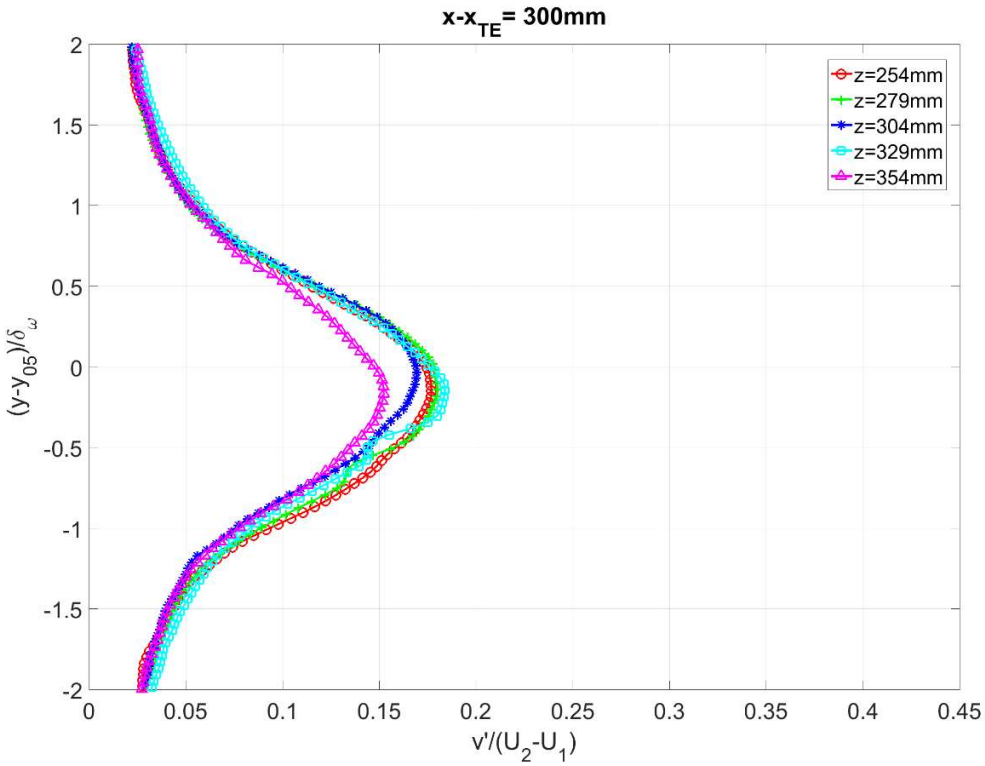
x-x_TE= 300mm
z=254mm
z=279mm
z=304mm
z=329mm
z=354mm
(y-y_05)/δ_ω
v'/(U_2-U_1)

(b)

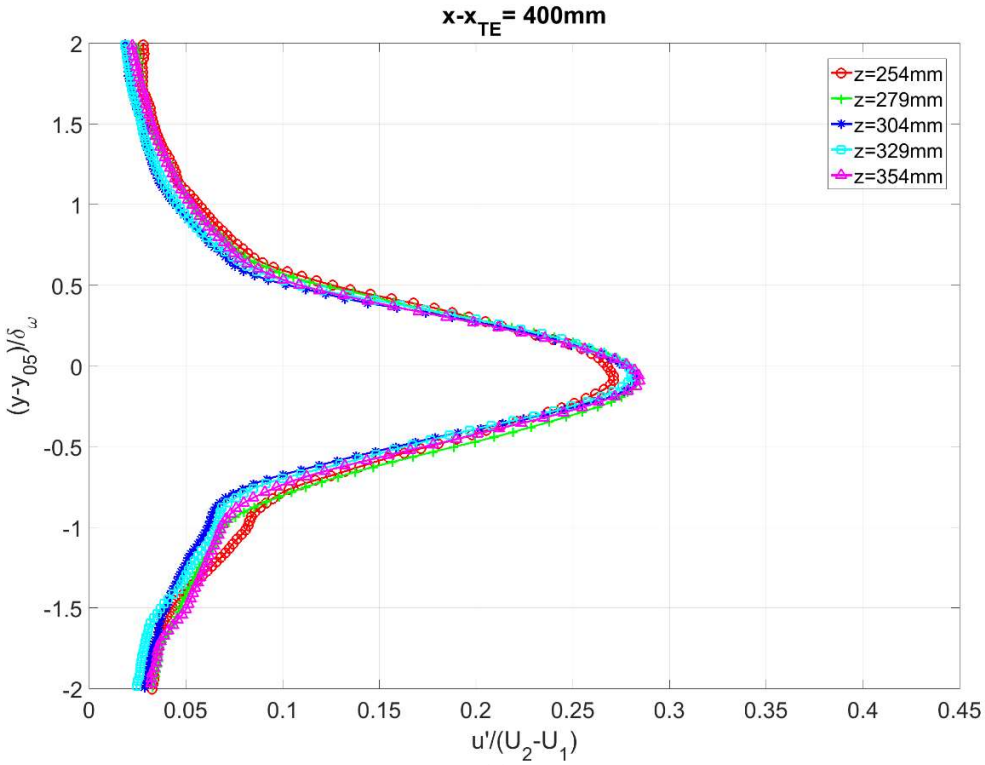
x-x_TE= 400mm
z=254mm
z=279mm
z=304mm
z=329mm
z=354mm
(y-y_05)/δ_ω
u'/(U_2-U_1)

(c)

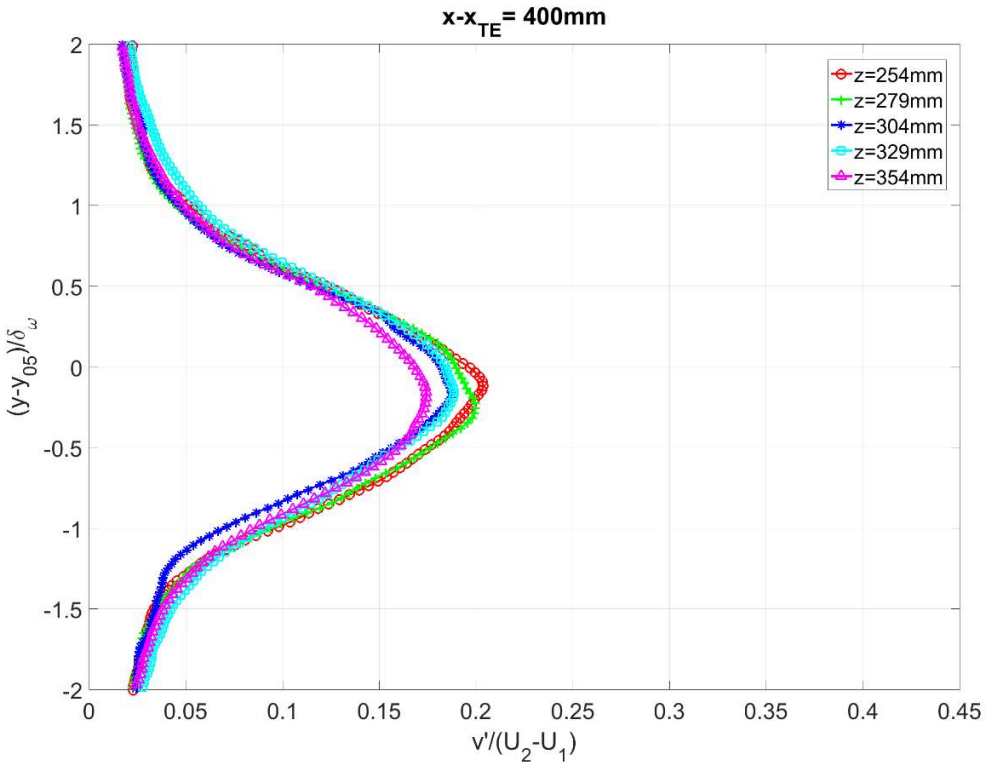
x-x_TE= 400mm
z=254mm
z=279mm
z=304mm
z=329mm
z=354mm
(y-y_05)/δ_ω
v'/(U_2-U_1)

(d)

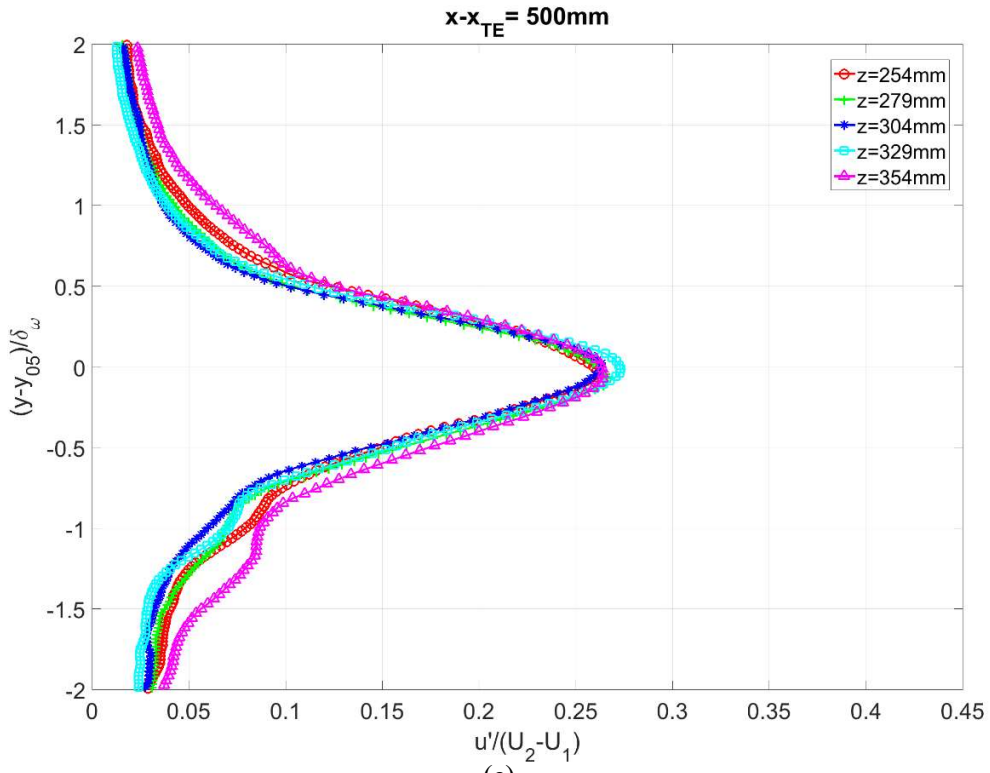
x-x_TE= 500mm
z=254mm
z=279mm
z=304mm
z=329mm
z=354mm
(y-y_05)/δ_ω
u'/(U_2-U_1)
2
1.5
1
0.5
0
-0.5
-1
-1.5
-2
0
0.05
0.1
0.15
0.2
0.25
0.3
0.35
0.4
0.45

(e)

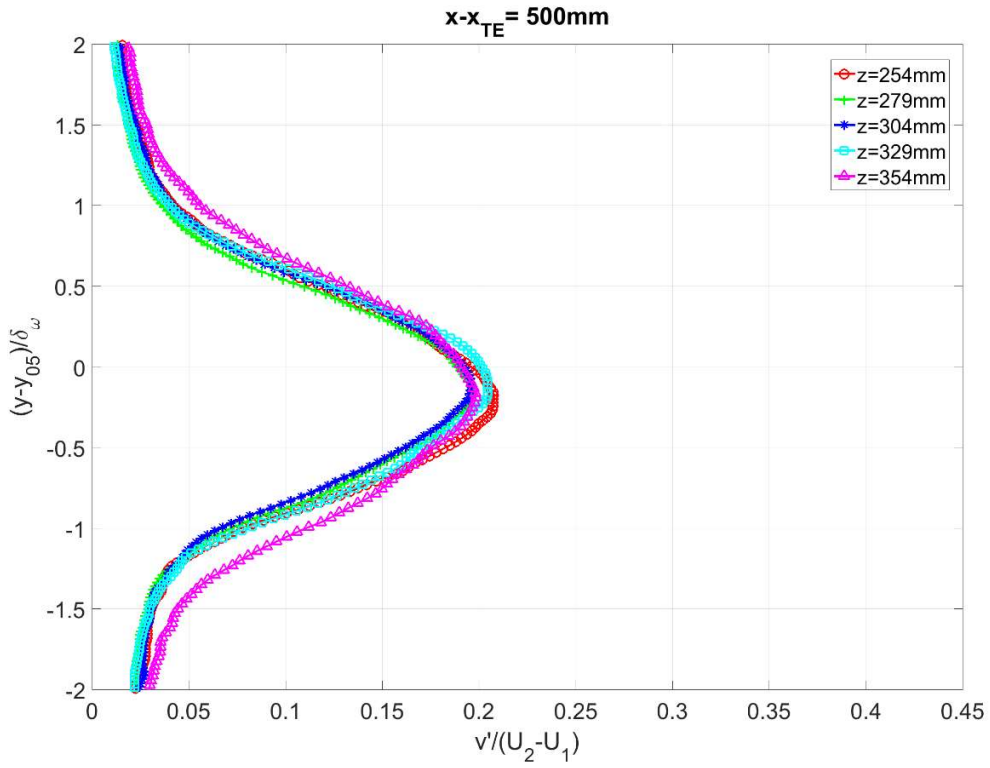
x-x_TE= 500mm
z=254mm
z=279mm
z=304mm
z=329mm
z=354mm
(y-y_05)/δ_ω
v'/(U_2-U_1)
2
1.5
1
0.5
0
-0.5
-1
-1.5
-2
0
0.05
0.1
0.15
0.2
0.25
0.3
0.35
0.4
0.45

(f)

Figure 4.20: Turbulent intensities of u and v components in the direction parallel to the trailing edge at 50Hz of the oscillating frequency at (a), (b) $x - x_{TE} = 300mm$ (c), (d) $x - x_{TE} = 400mm$ (e), (f) $x - x_{TE} = 500mm$

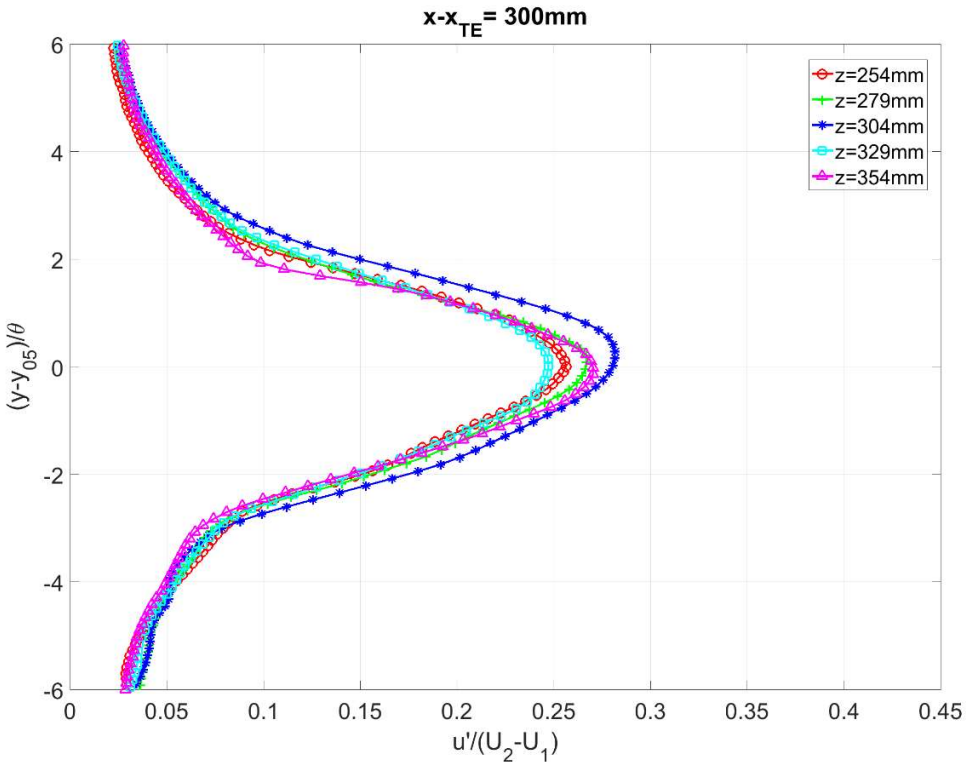

(a)

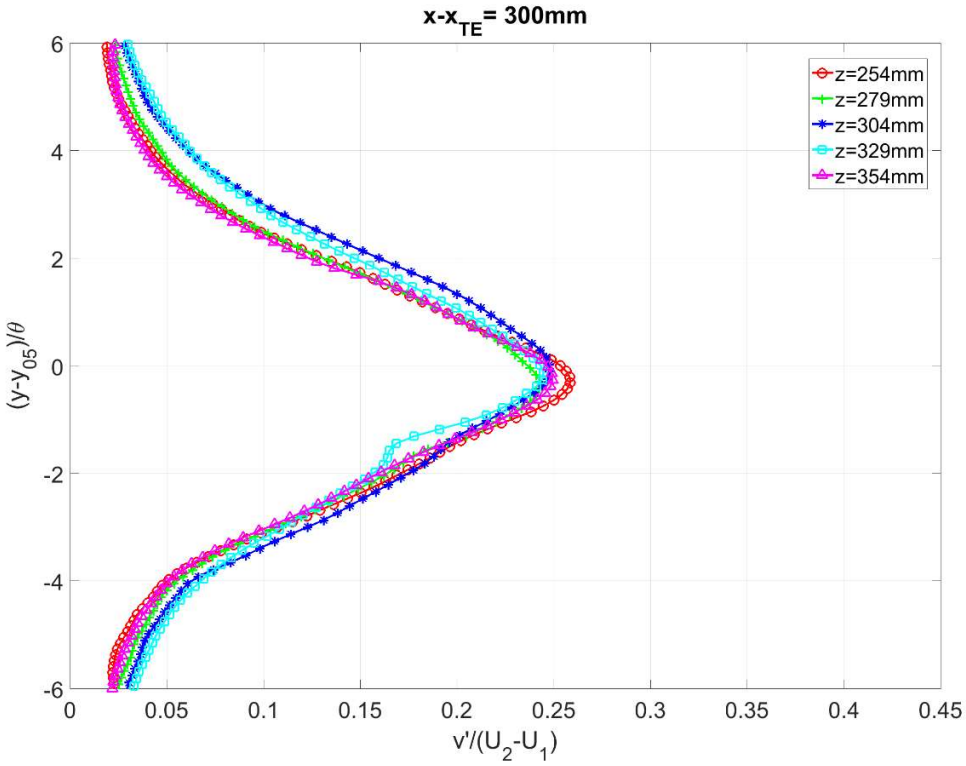
x-x_TE= 300mm
z=254mm
z=279mm
z=304mm
z=329mm
z=354mm
(y-y_05)/θ
v'/(U_2-U_1)

(b)

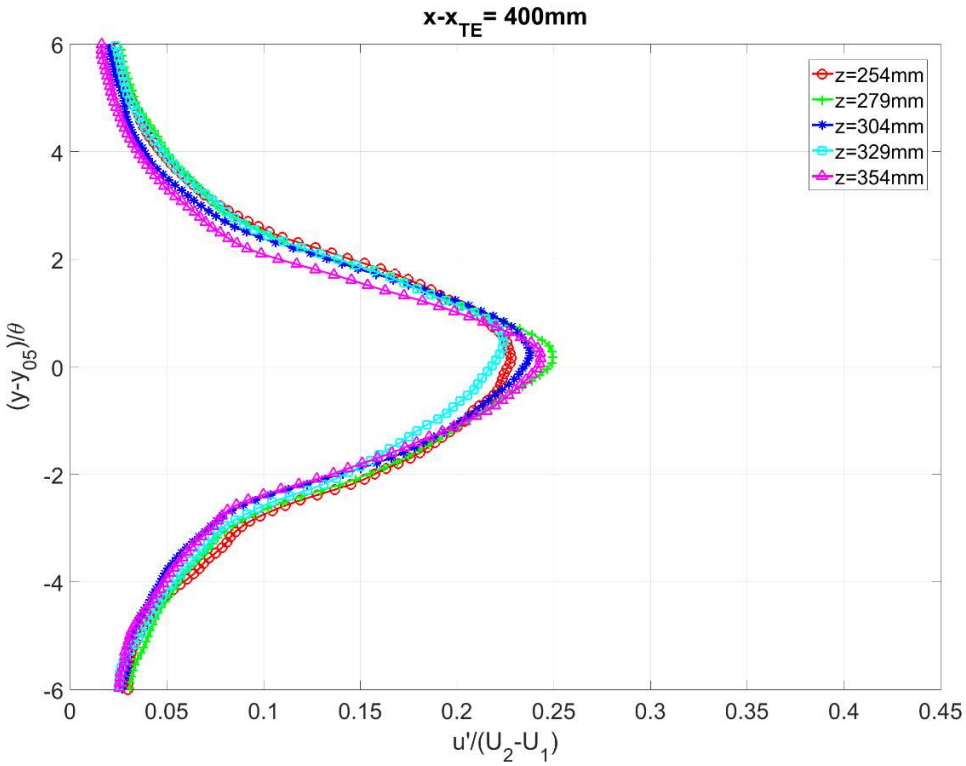
x-x_TE= 400mm
z=254mm
z=279mm
z=304mm
z=329mm
z=354mm
(y-y_05)/θ
u'/(U_2-U_1)

(c)

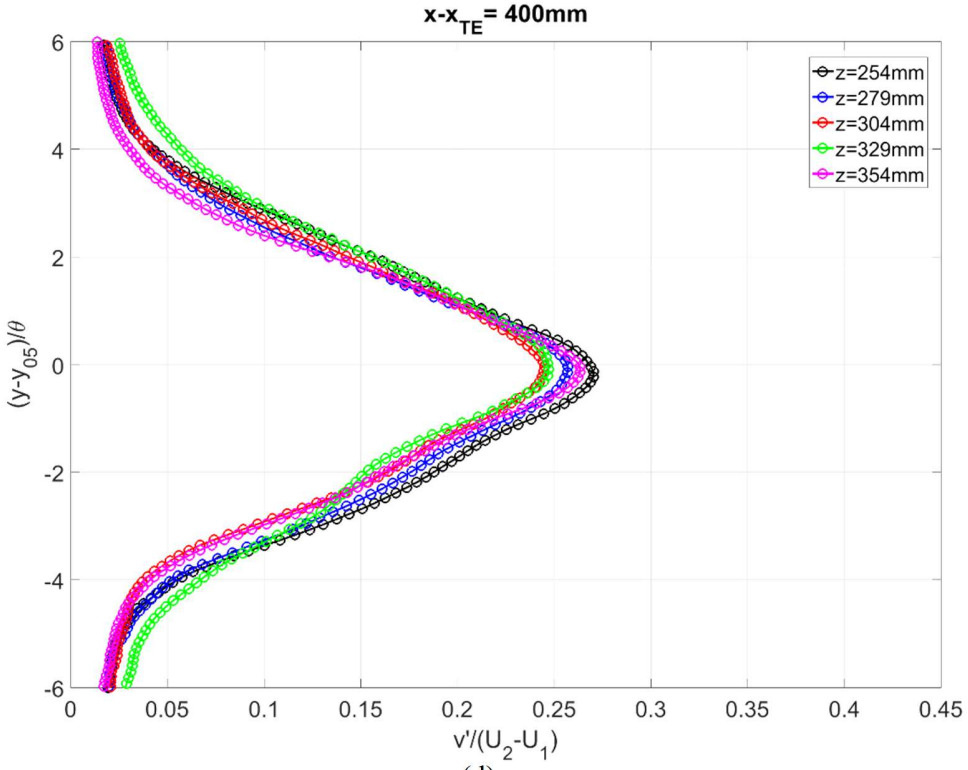
x-x_TE= 400mm
z=254mm
z=279mm
z=304mm
z=329mm
z=354mm
(y-y_05)/θ
v'/(U_2-U_1)
6
4
2
0
-2
-4
-6
0
0.05
0.1
0.15
0.2
0.25
0.3
0.35
0.4
0.45

(d)

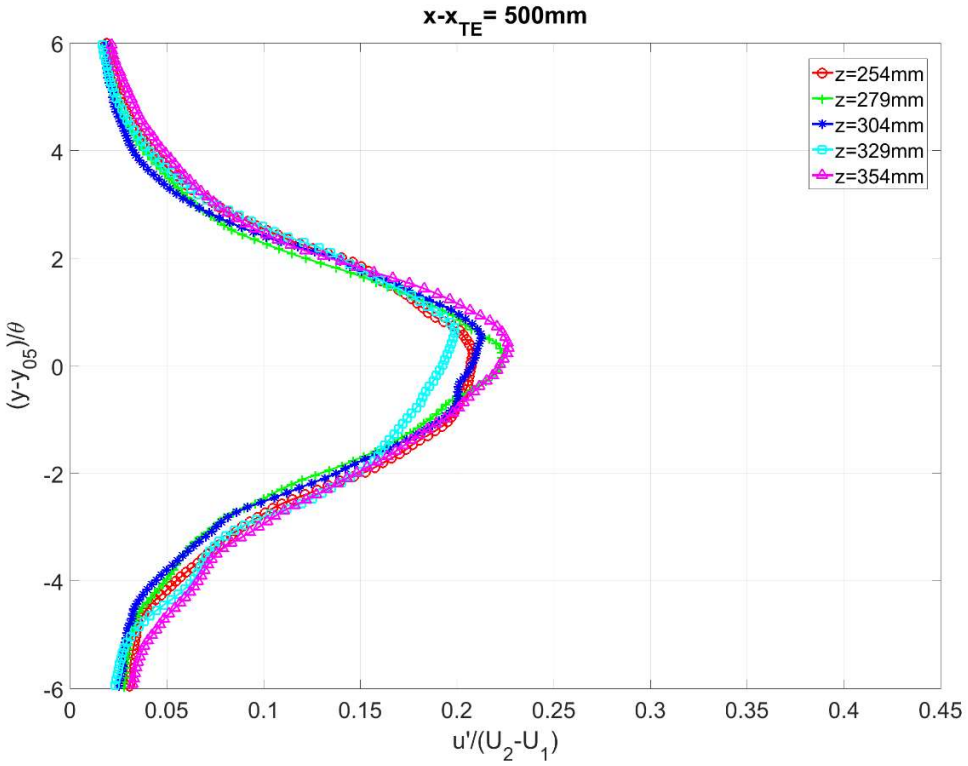
x-x_TE= 500mm
z=254mm
z=279mm
z=304mm
z=329mm
z=354mm
(y-y_05)/θ
u'/(U_2-U_1)
6
4
2
0
-2
-4
-6
0
0.05
0.1
0.15
0.2
0.25
0.3
0.35
0.4
0.45

(e)

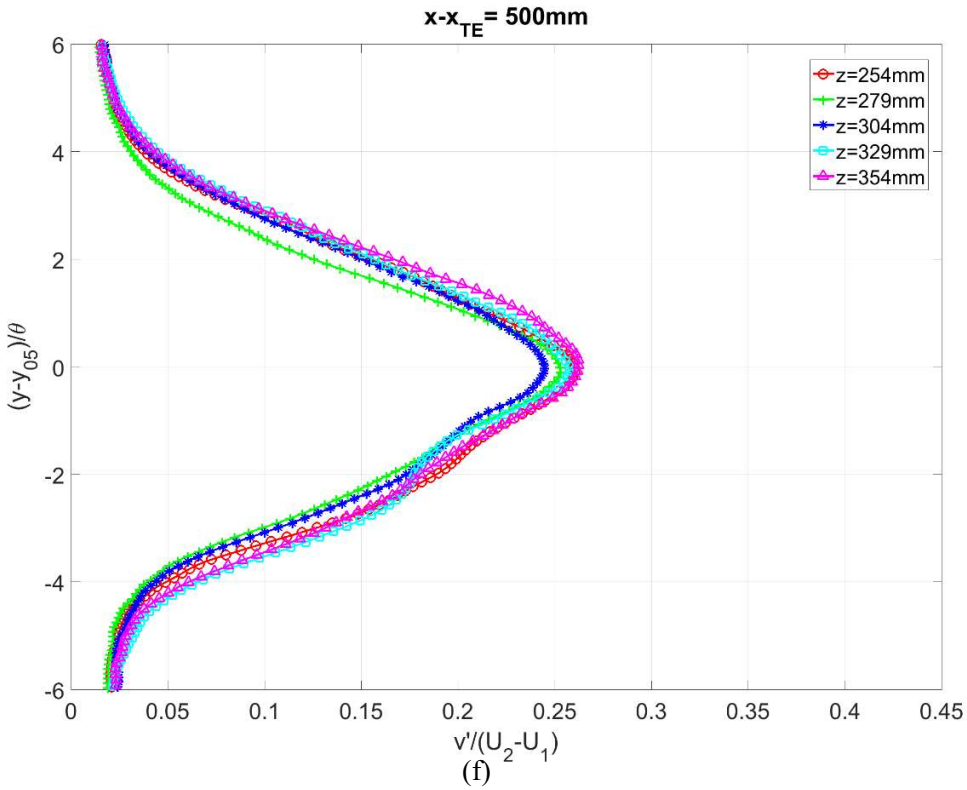

(f)

Figure 4.21: Turbulent intensities of u and v components in the direction parallel to the trailing edge at 75Hz of the oscillating frequency at (a), (b) $x - x_{TE} = 300mm$ (c), (d) $x - x_{TE} = 400mm$ (e), (f) $x - x_{TE} = 500mm$

There are no definite differences between the random sampling data and the phase-locked sampling data. One of the trends is that the maximum intensities of $\overline{v'^2}^{1/2}$ remain constant behind $x - x_{TE} = 450mm$ (Fig. 4.18 and Fig. 4.7).

4.2.4 Vorticity field

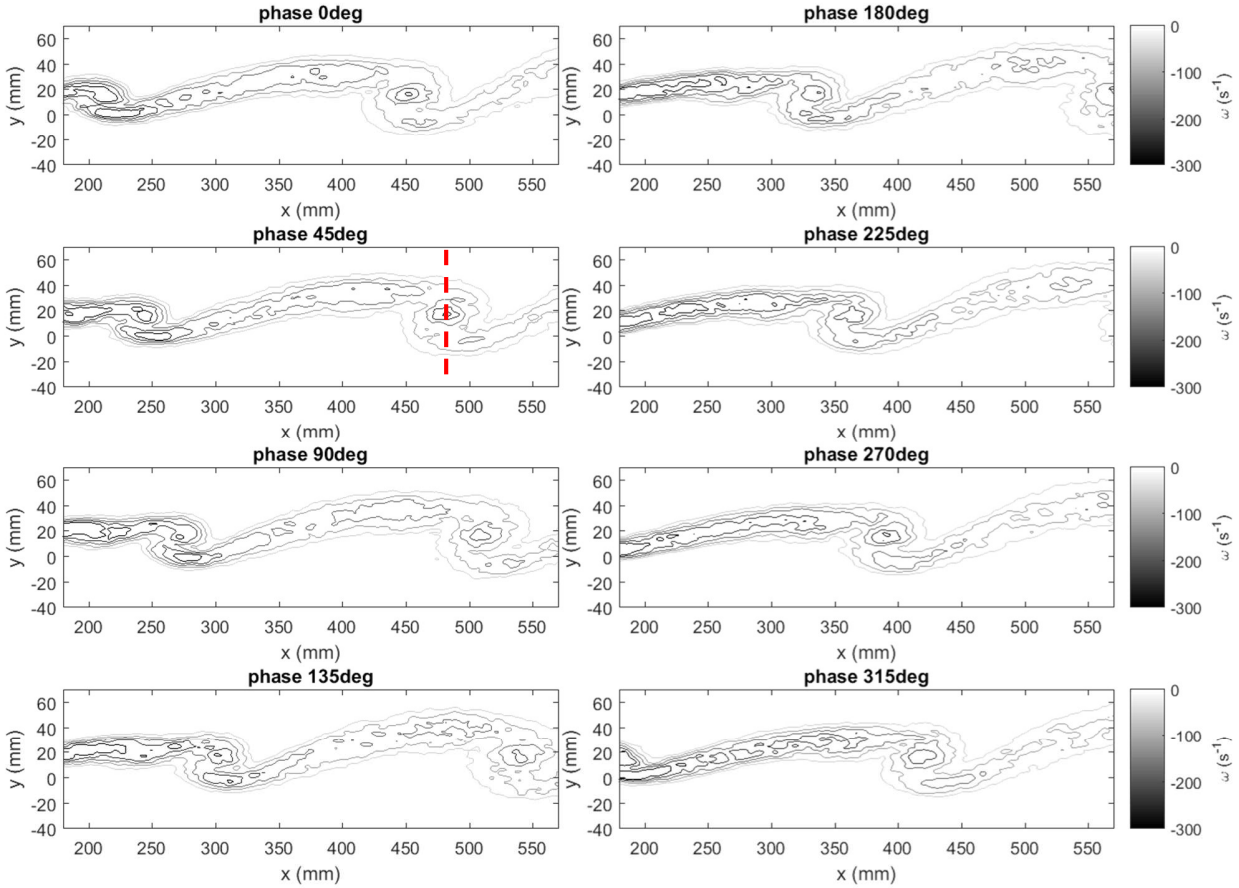

Figure 4.22: Phase-locked vorticity fields at z=254mm with forcing frequency of f=50Hz

Figure 4.22 shows the phase-locked vorticity fields at spanwise location z = 254 mm and forcing frequency of f = 50 Hz. The horizontal axis is defined as measured distance from the trailing edge to measurement point. The vorticity field at phase 45° shows that the vortex is angled vertically at around x = 480 mm ($R(x - x_{TE})/\lambda_x = 0.45$), which indicates the development of mixing layer remains neutral at this point.

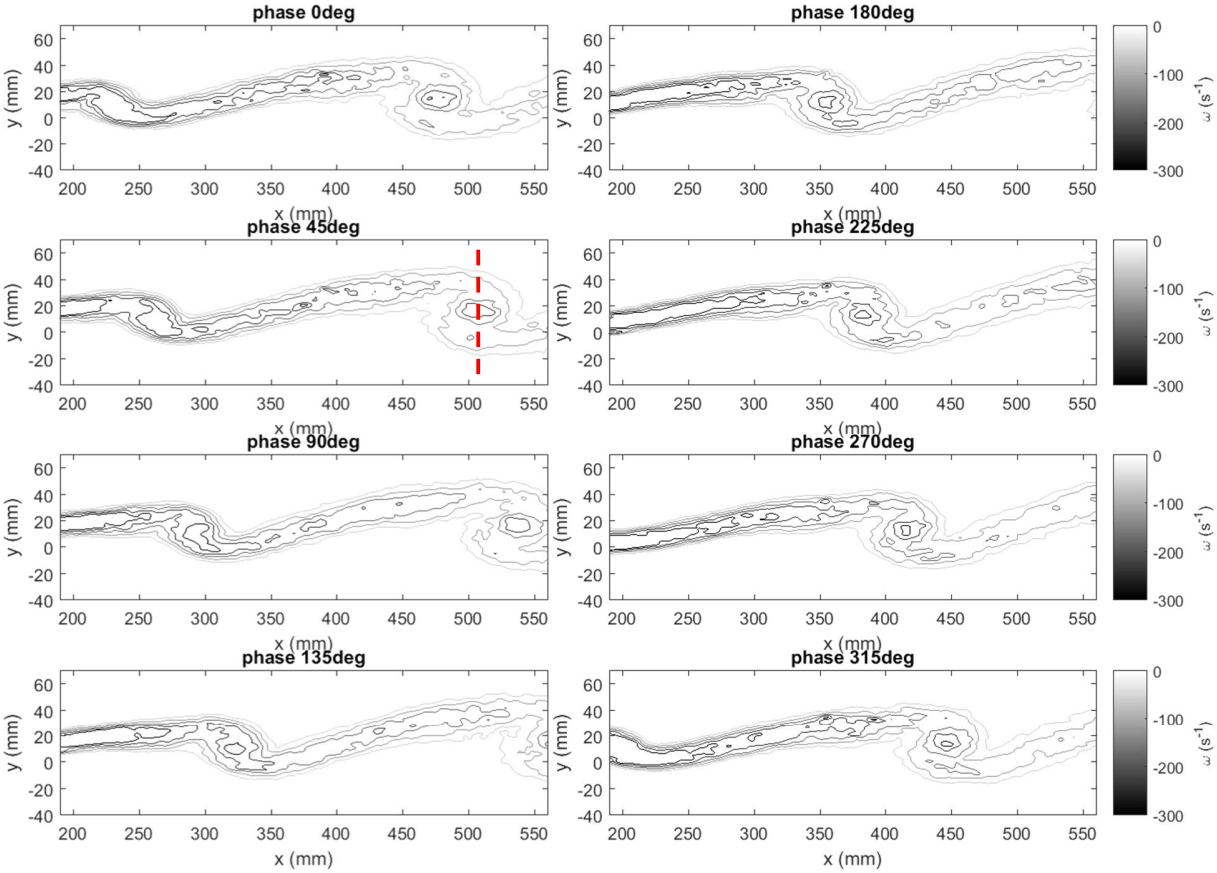

Figure 4.23: Phase-locked vorticity fields at z=304mm with forcing frequency of f=50Hz

Figure 4.23 shows the phase-locked vorticity fields at spanwise location z = 304 mm and forcing frequency of f = 50 Hz. The vorticity field at phase 45° shows that the vortex is angled vertically at around x = 500 mm ($R(x - x_{TE})/\lambda_x = 0.45$), which indicates the development of mixing layer remains neutral at this point.

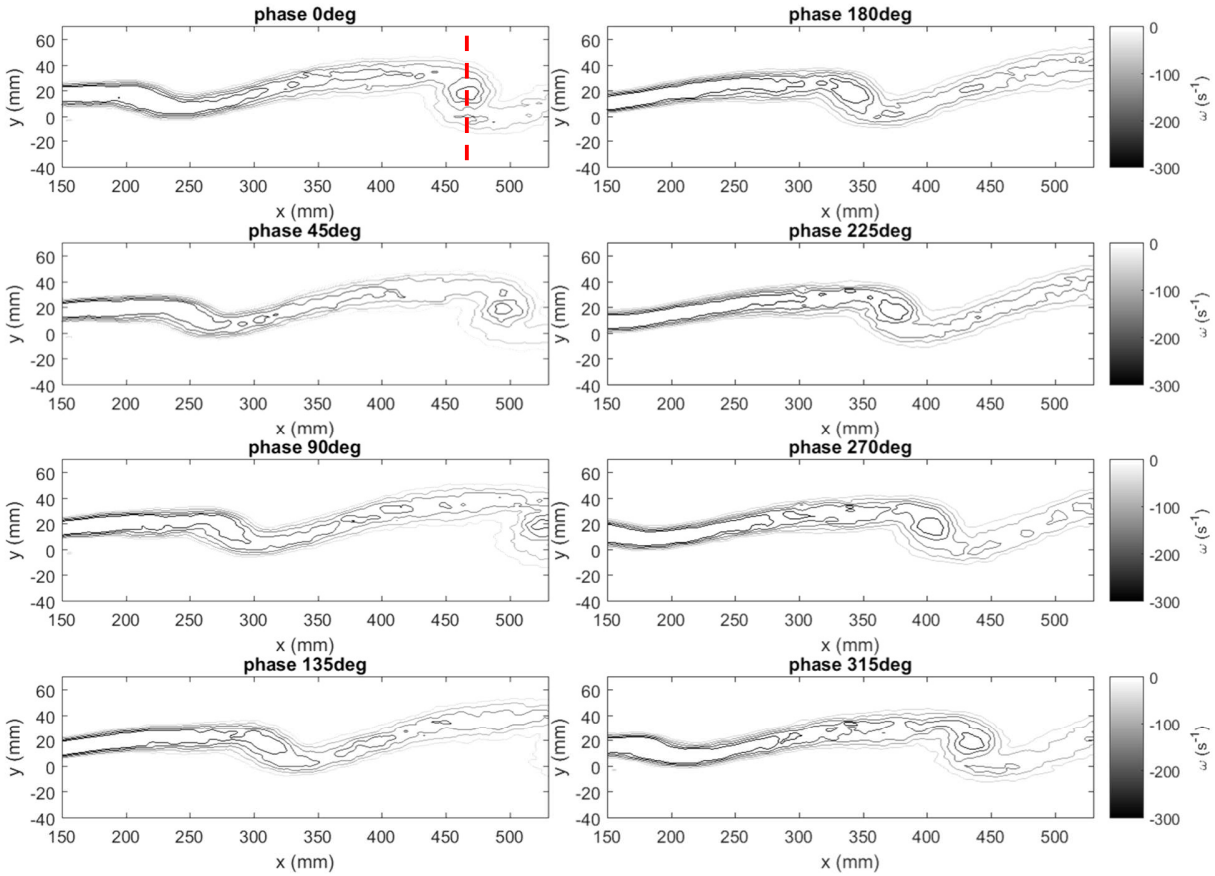

Figure 4.24: Phase-locked vorticity fields at z=354mm with forcing frequency of f=50Hz

Figure 4.24 shows the phase-locked vorticity fields at spanwise location z = 354 mm and forcing frequency of f = 50 Hz. The vorticity field at phase 90º shows that the vortex is angled vertically at around x = 460 mm ($R(x - x_{TE})/\lambda_x = 0.4$), which indicates the development of mixing layer remains neutral at this point.

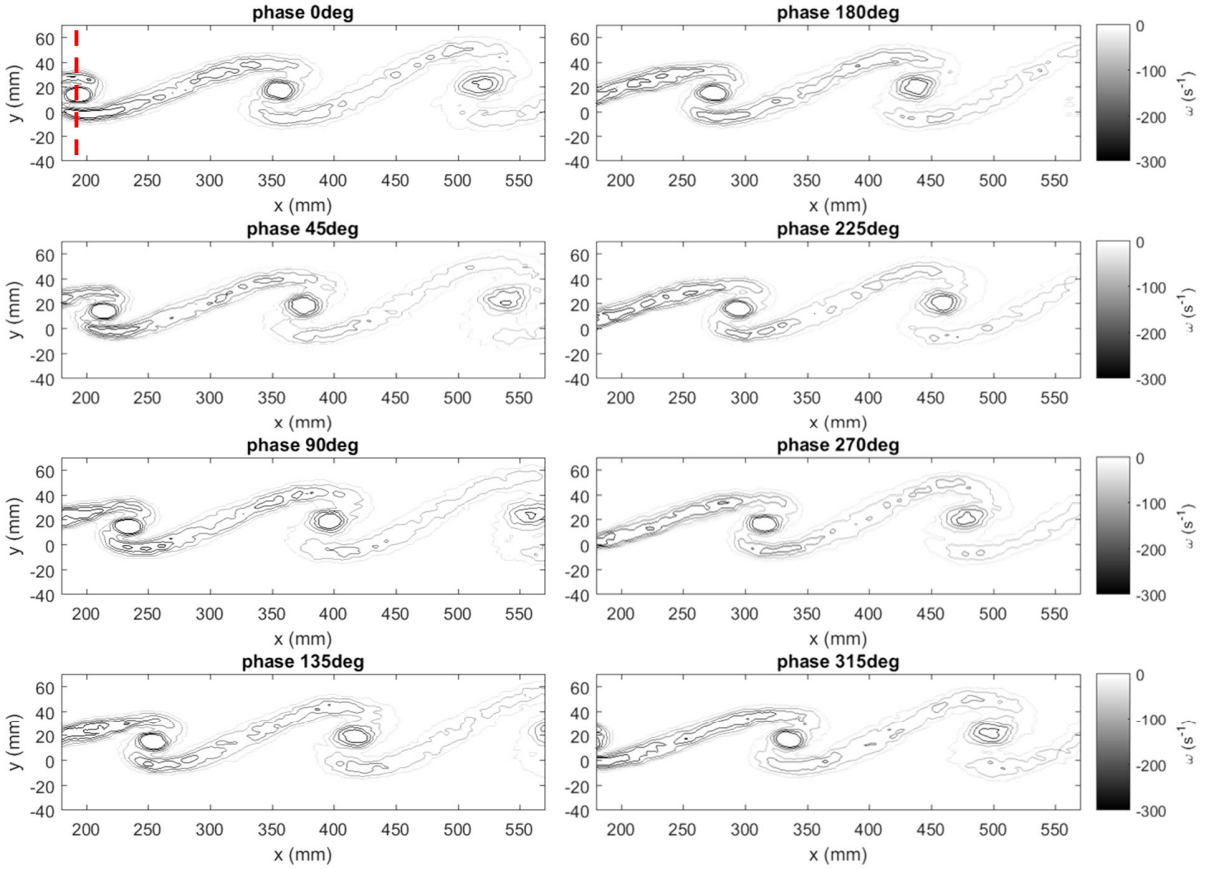

Figure 4.25: Phase-locked vorticity fields at z=254mm with forcing frequency of f=75Hz

Figure 4.25 shows the phase-locked vorticity fields at spanwise location z = 254 mm and forcing frequency of f = 75 Hz. The vorticity field at phase 0° shows that the vortex is angled vertically at around x = 200 mm, and this location corresponds to $R(x - x_{TE})/\lambda_x = 0.28$. However, this experimental result obtained does not support the vorticity thickness profile from section 4.1.2 as Figure 4.25 does not indicate any saturation point in the mixing layer flow as calculated in section 4.1.2. In addition, the entire vorticity fields with forcing frequency of 75Hz does not behave like the vorticity fields at f = 50 Hz, which implies that vorticity field is overamplified at f = 75 Hz.

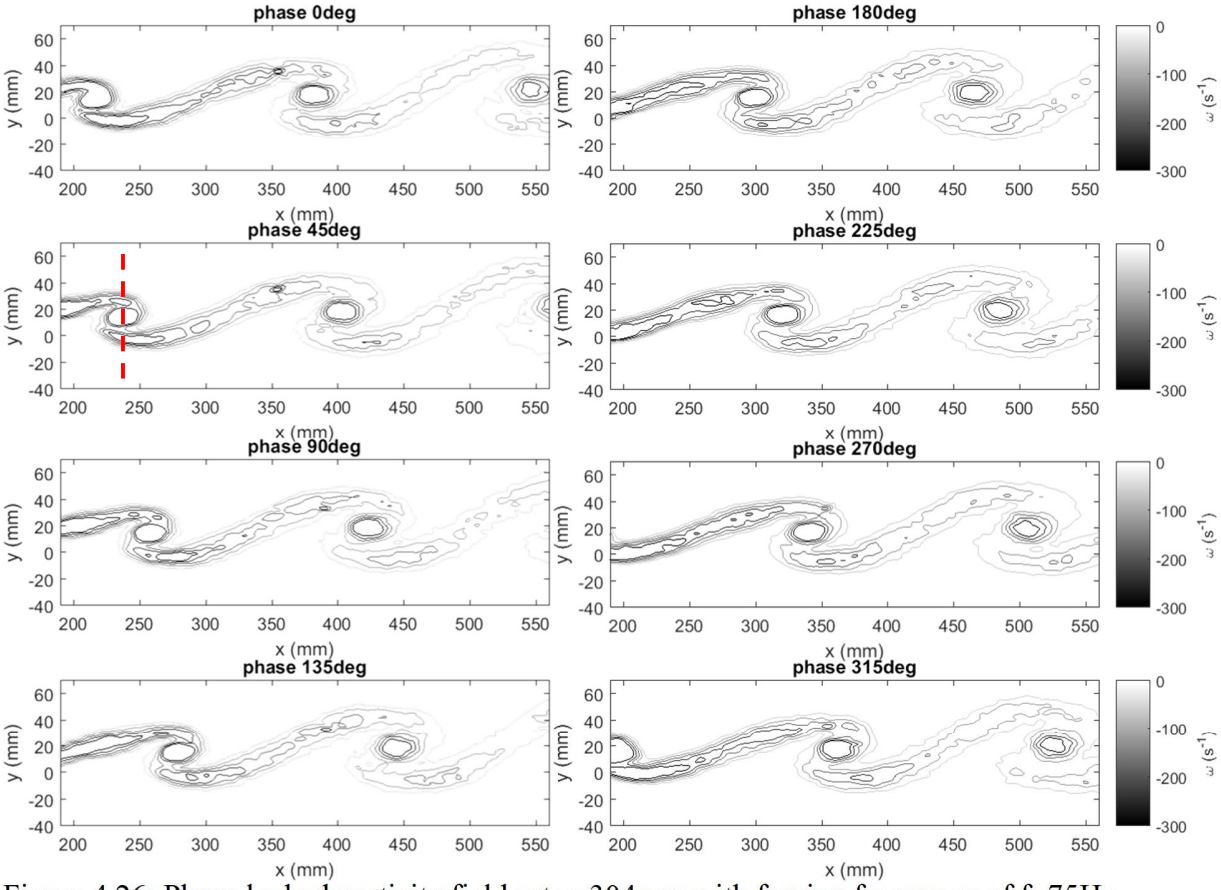

Figure 4.26: Phase-locked vorticity fields at z=304mm with forcing frequency of f=75Hz

Figure 4.26 shows the phase-locked vorticity fields at spanwise location z = 304 mm and forcing frequency of f = 75 Hz. The vorticity field at phase 45° shows that the vortex is angled vertically at around x = 230 mm ($R(x - x_{TE})/\lambda_x = 0.32$). However, this experimental result obtained does not support the vorticity thickness profile from section 4.1.2 as Figure 4.26 does not indicate any saturation point in the mixing layer flow as calculated in section 4.1.2. In addition, the entire vorticity fields with forcing frequency of 75Hz does not behave like the vorticity fields at f = 50 Hz, which implies that vorticity field is too amplified at f = 75 Hz.

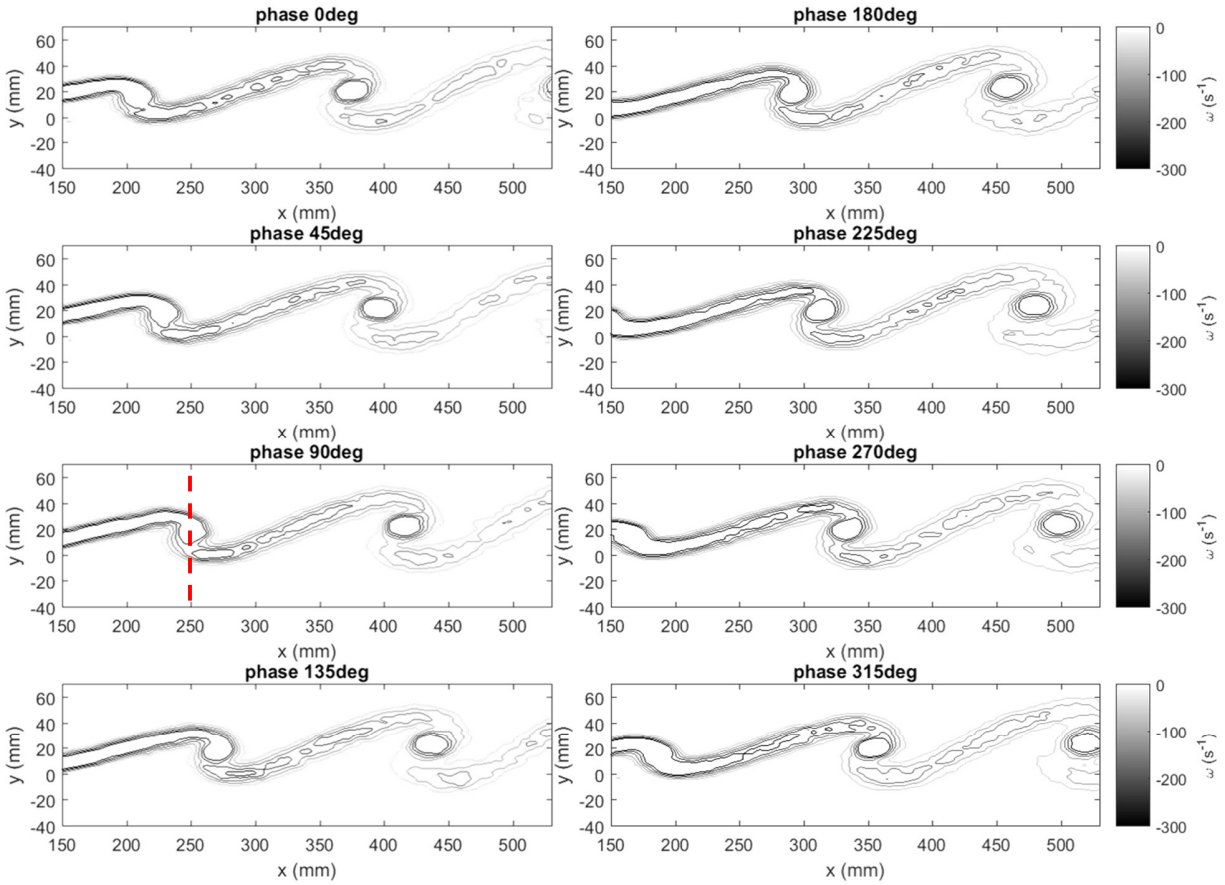

Figure 4.27: Phase-locked vorticity fields at z=354mm with forcing frequency of f=75Hz

Figure 4.27 shows the phase-locked vorticity fields at spanwise location z = 254 mm and forcing frequency of f = 75 Hz. The vorticity field at phase 90º shows that the vortex is angled vertically at around x = 250 mm, and this location corresponds to $R(x - x_{TE})/\lambda_x = 0.34$. However, this experimental result obtained does not support the vorticity thickness profile from section 4.1.2 as Figure 4.27 does not indicate any saturation point in the mixing layer flow as calculated in section 4.1.2. In addition, the entire behavior of the vorticity fields at 75Hz does not behave the vorticity fields at f = 50 Hz, which implies that vorticity field is overexcited at f = 75 Hz.

If the two-dimensional flow is properly amplified, the locations where vertical vortices are generated should be constant across the entire wingspan. However, Figure 4.27 contradicts the previous statement as vortex locations vary linearly across the span. As such, vorticity thickness results obtained from section 4.1.2 are incorrect.

4.2.5 Center location of the mixing layer

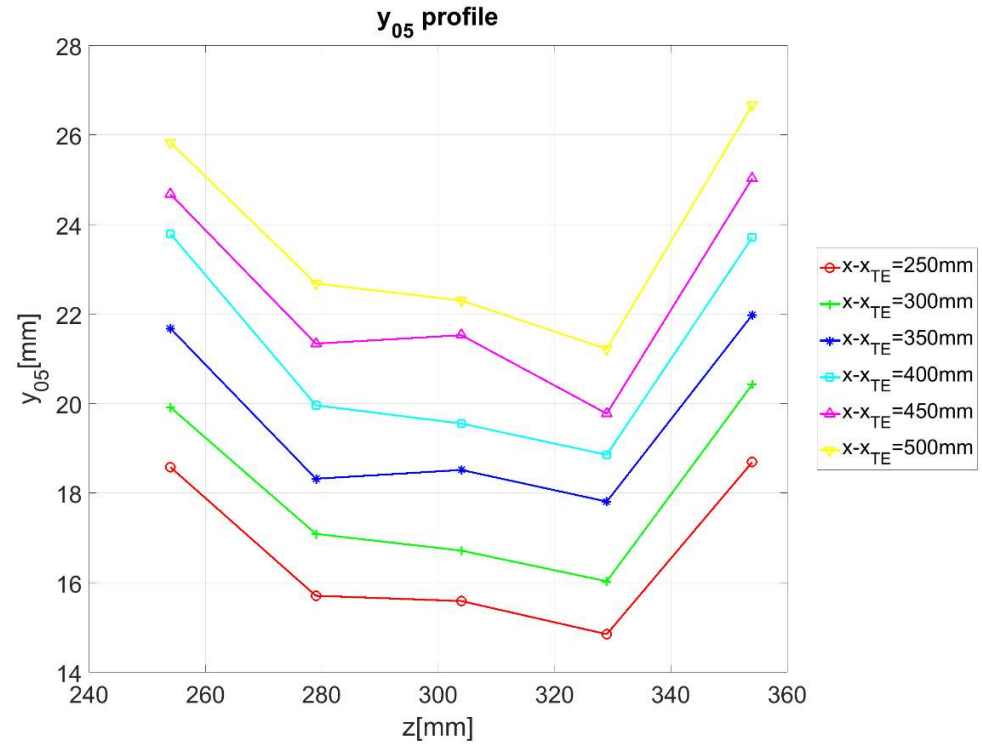

(a)

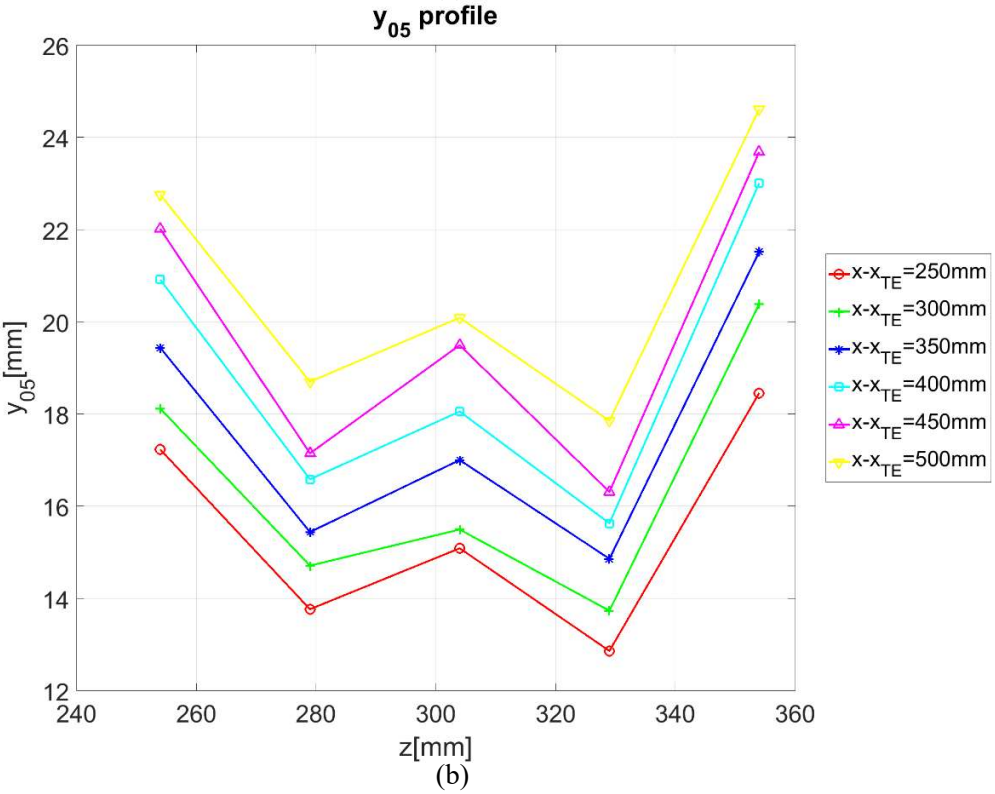

(b)

Figure 4.28: Phase-locked center location profile of the mixing layer at (a) f=50Hz (b) f=75Hz

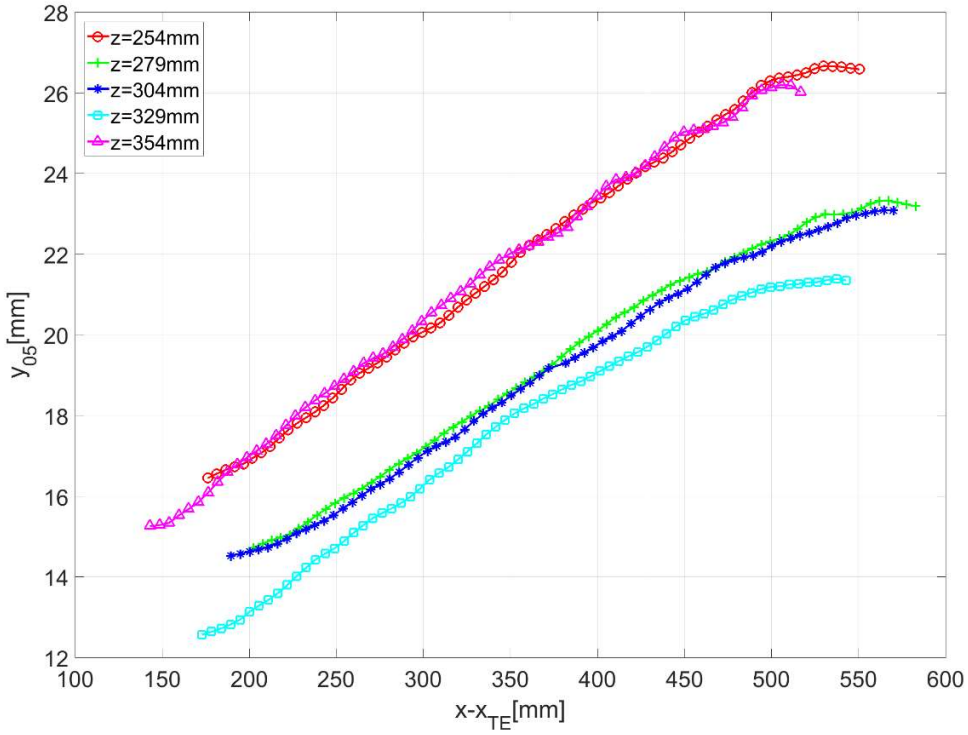

(a)

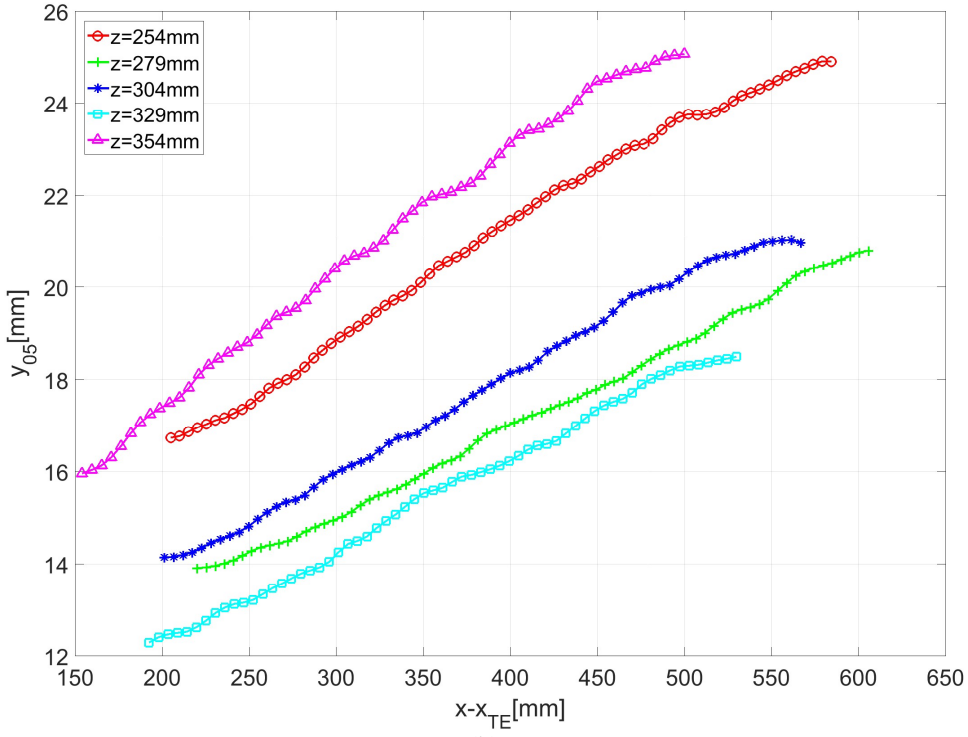

(b)

Figure 4.29: Phase-locked center location profile along the free stream at (a) f=50Hz (b) f=75Hz

Figures 4.28 and 4.29 show the center location of mixing layer profile along both trailing edge and free stream respectively, using phase-locked sampling data at 50 Hz and 75 Hz. The results are the same as figures 4.11 and 4.12, where y_{05} profile varies throughout the entire wingspan. In addition, the mean local center increases downstream and reaches maxima points at z = 254 mm and z = 354 mm respectively.

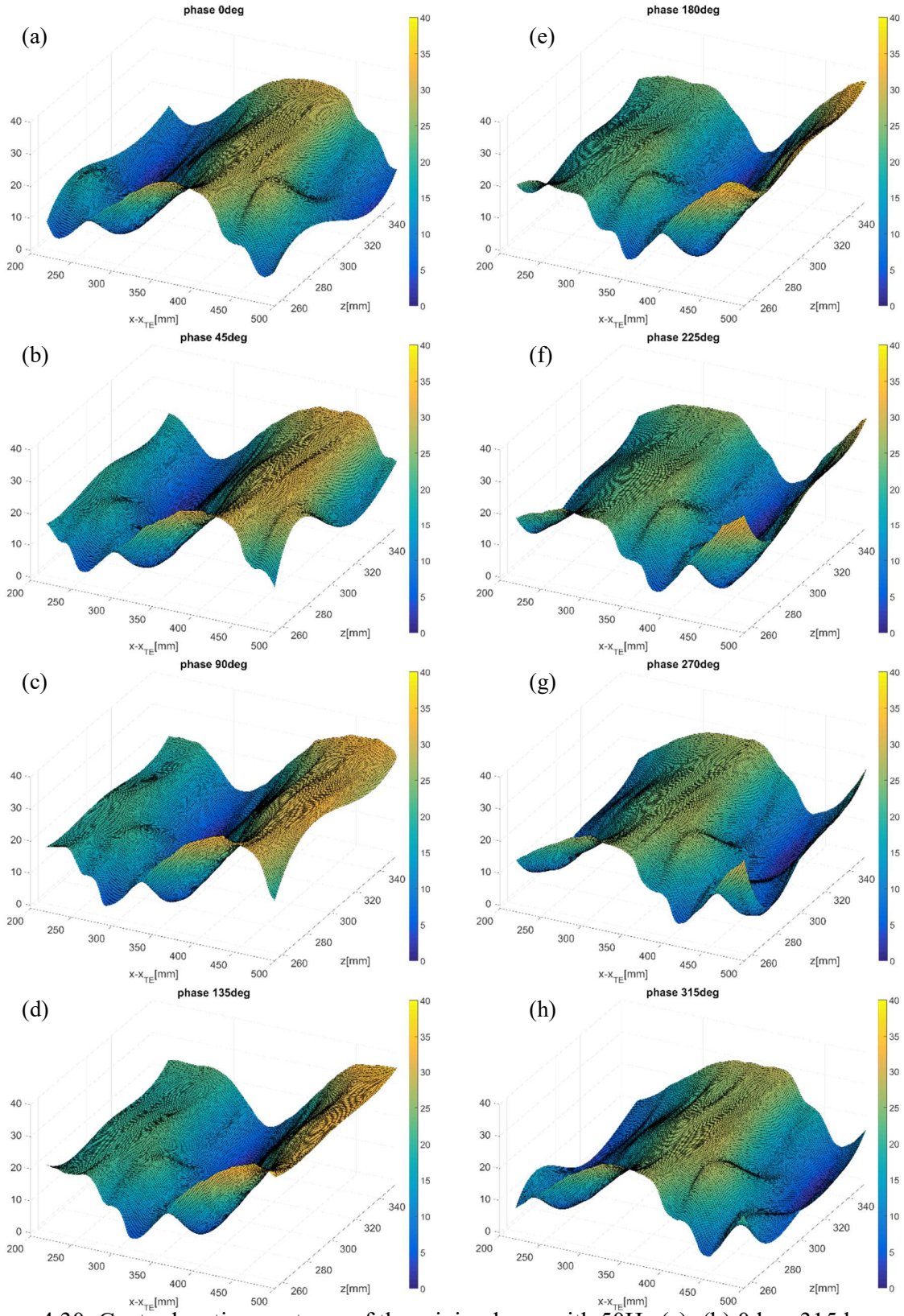

Figure 4.30: Center location contours of the mixing layer with 50Hz (a)~(h) 0deg~315deg

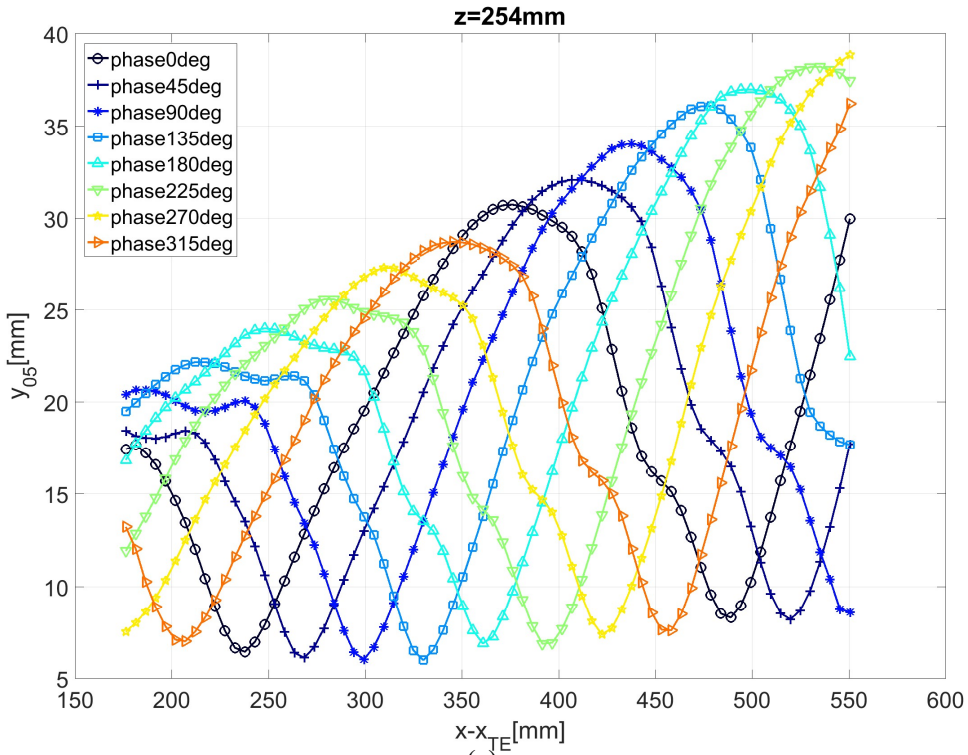
z=254mm
phase0deg
phase45deg
phase90deg
phase135deg
phase180deg
phase225deg
phase270deg
phase315deg
y05[mm]
x-xTE[mm]
40
35
30
25
20
15
10
5
150
200
250
300
350
400
450
500
550
600

(a)

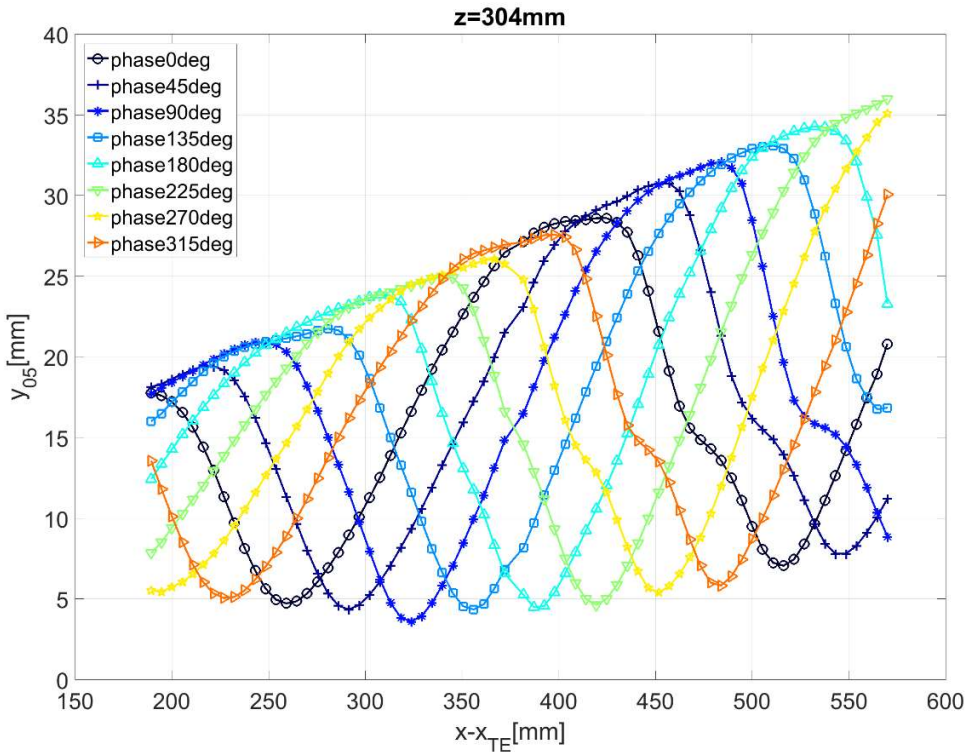
z=304mm
phase0deg
phase45deg
phase90deg
phase135deg
phase180deg
phase225deg
phase270deg
phase315deg
y05[mm]
x-xTE[mm]
40
35
30
25
20
15
10
5
0
150
200
250
300
350
400
450
500
550
600

(b)

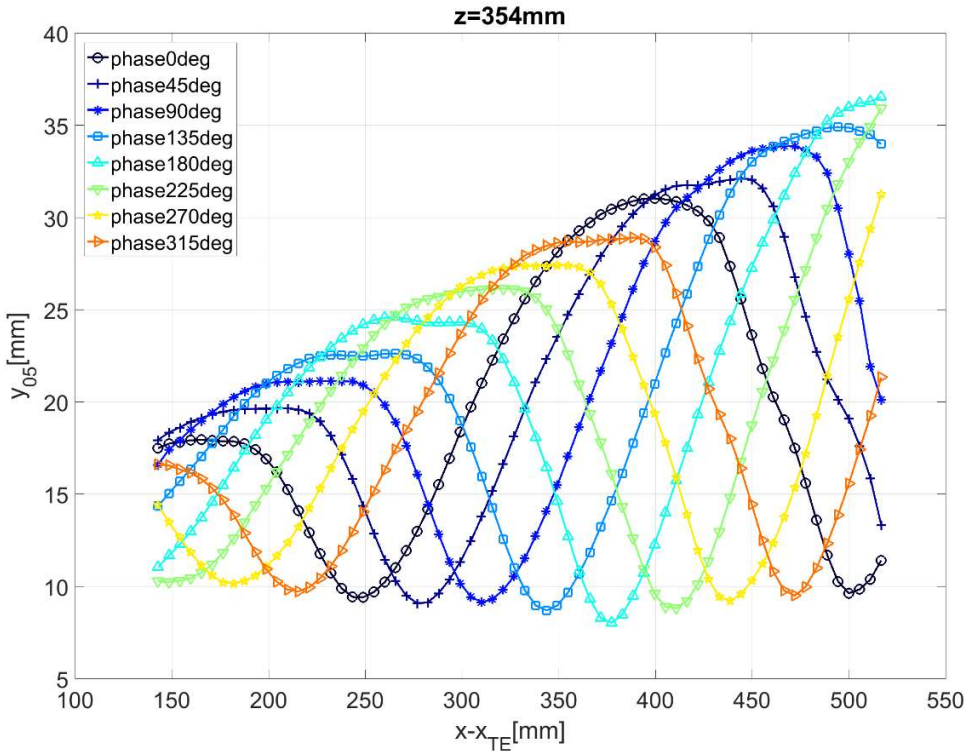

(c)

Figure 4.31: Center location of the mixing layer with 50Hz in time and in space (a) z=254mm (b) z=304mm (c) z=354mm

Figure 4.30 shows the center location contours and Figures 4.31 show the phase-locked center location profile of the mixing layer at three different spanwise locations for an excitation frequency of 50 Hz. From Figures 4.31 the center location profiles downstream can be seen as an expanding sinusoidal wave, indicating the mixing layer flow is dominated by a single frequency that can be traced back to excitation at the trailing edge.

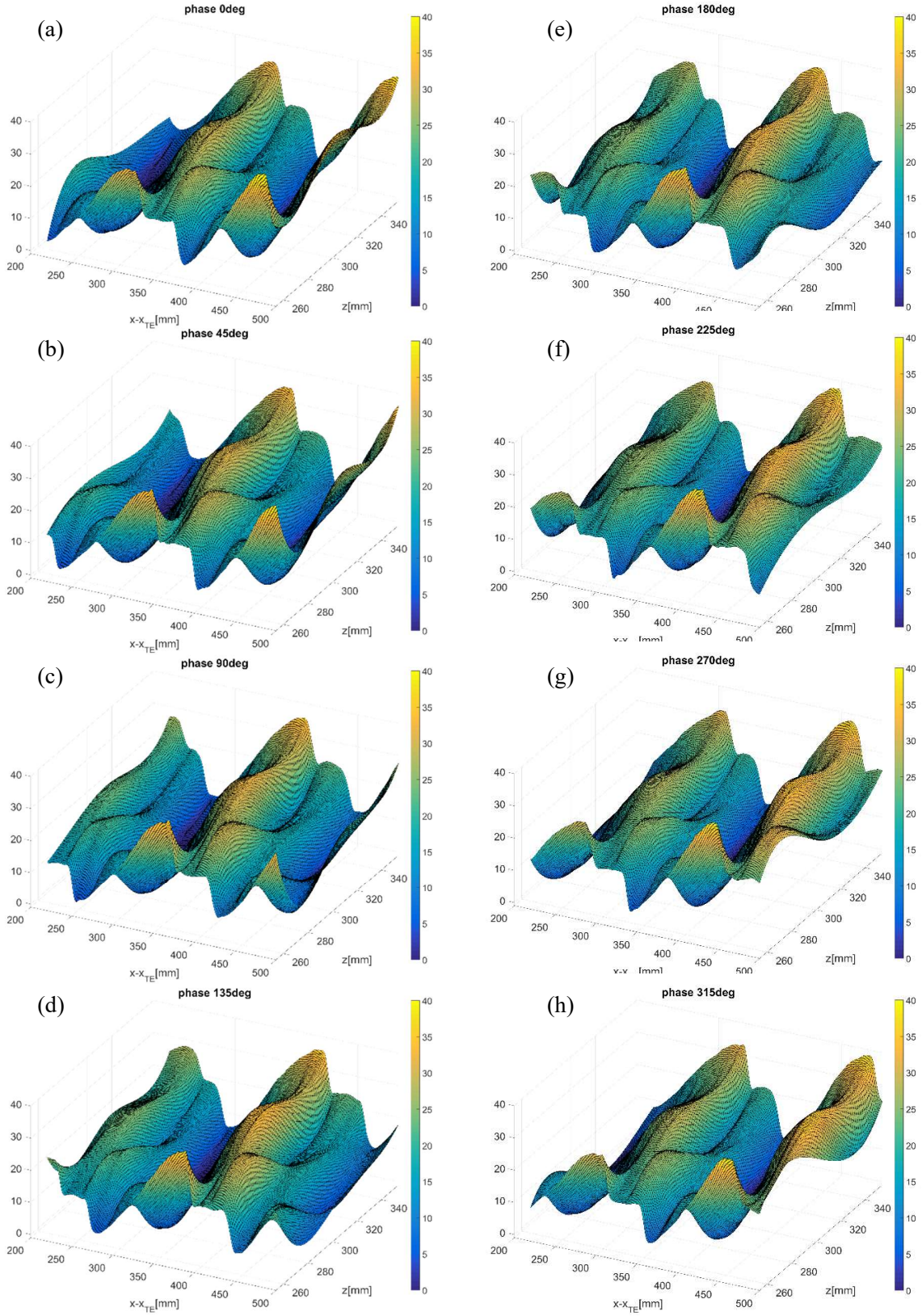

Figure 4.32: Center location contours of the mixing layer with 75Hz (a)~(h) 0deg ~315deg

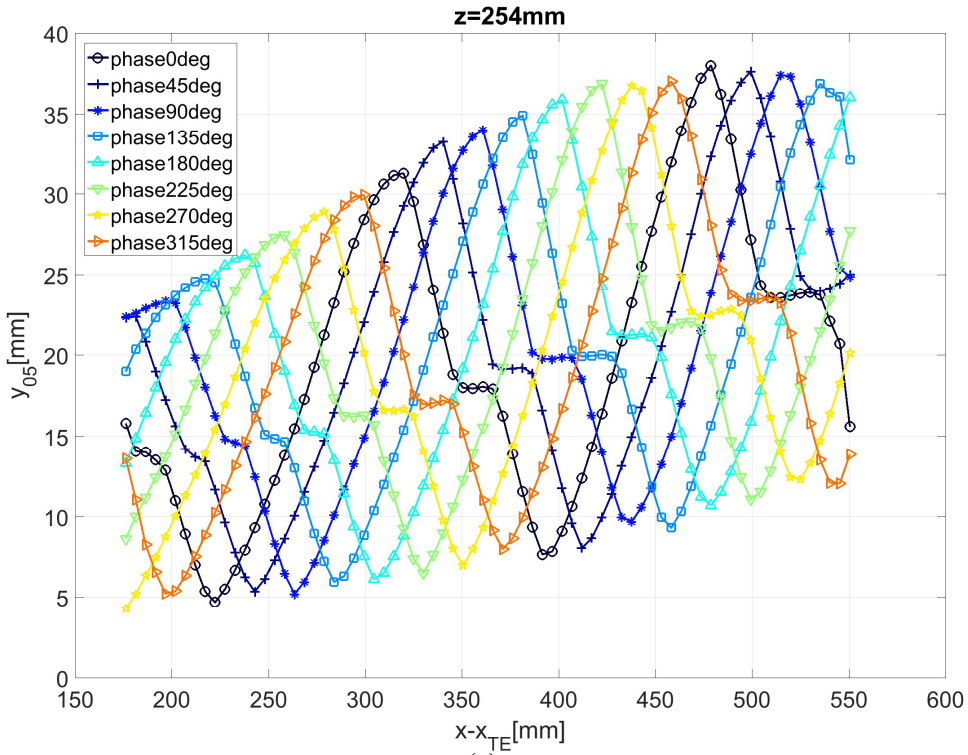
z=254mm
phase0deg
phase45deg
phase90deg
phase135deg
phase180deg
phase225deg
phase270deg
phase315deg
y05[mm]
x-xTE[mm]
0
5
10
15
20
25
30
35
40
150
200
250
300
350
400
450
500
550
600

(a)

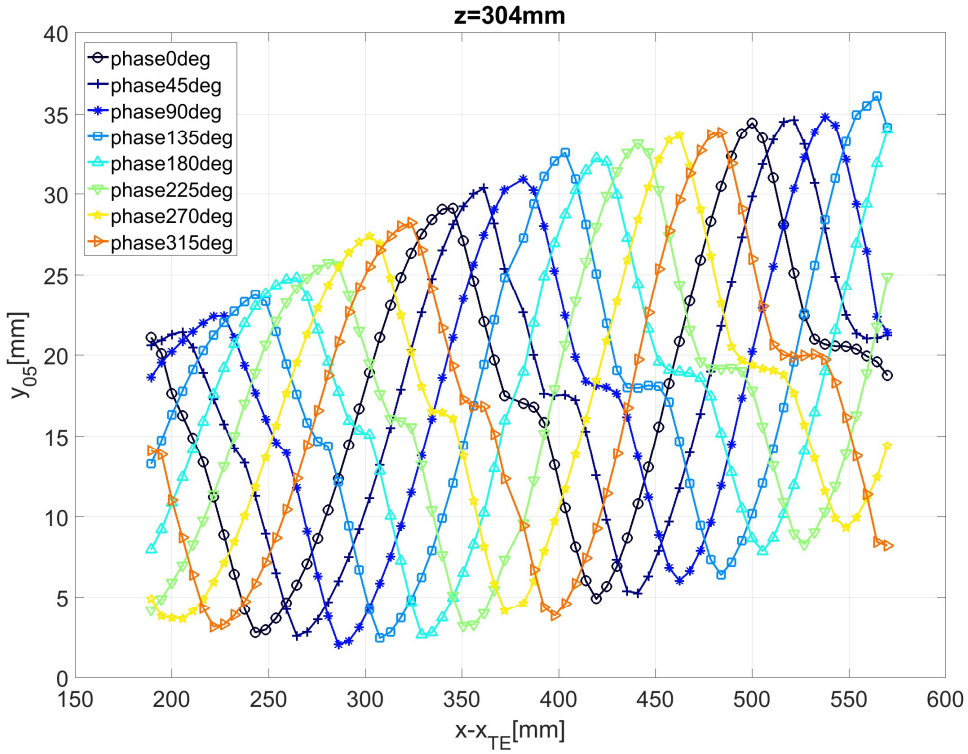
z=304mm
phase0deg
phase45deg
phase90deg
phase135deg
phase180deg
phase225deg
phase270deg
phase315deg
y05[mm]
x-xTE[mm]
0
5
10
15
20
25
30
35
40
150
200
250
300
350
400
450
500
550
600

(b)

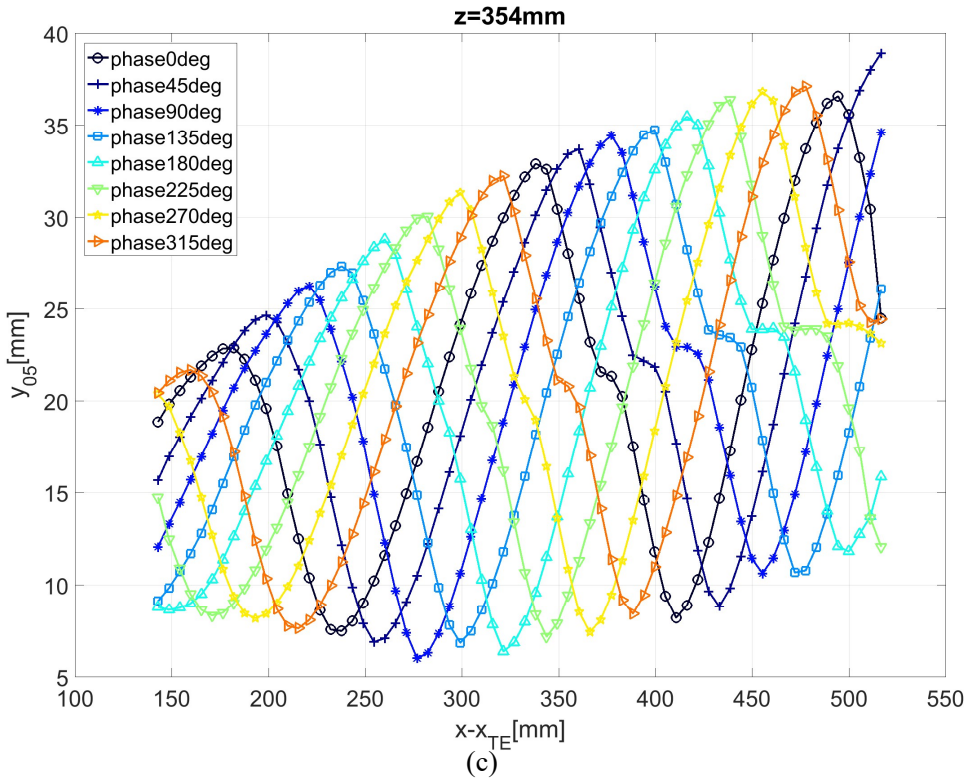

(c)

Figure 4.33: Center location of the mixing layer with 75Hz in time and in space (a) z=254mm (b) z=304mm (c) z=354mm

Figure 4.32 shows the center location contours and Figures 4.33 show the phase-locked center location profile of the mixing layer at three different spanwise locations for an excitation frequency of 75 Hz. From Figures 4.31 the center location profiles downstream are distorted especially at the center of y_{05} profiles. These distortion locations coincide with the characteristics of the phase-locked vorticity fields where there is a strong vortex present (Figures 4.25, 4.26, and 4.27).

4.2.6 Phase-locked velocity profile

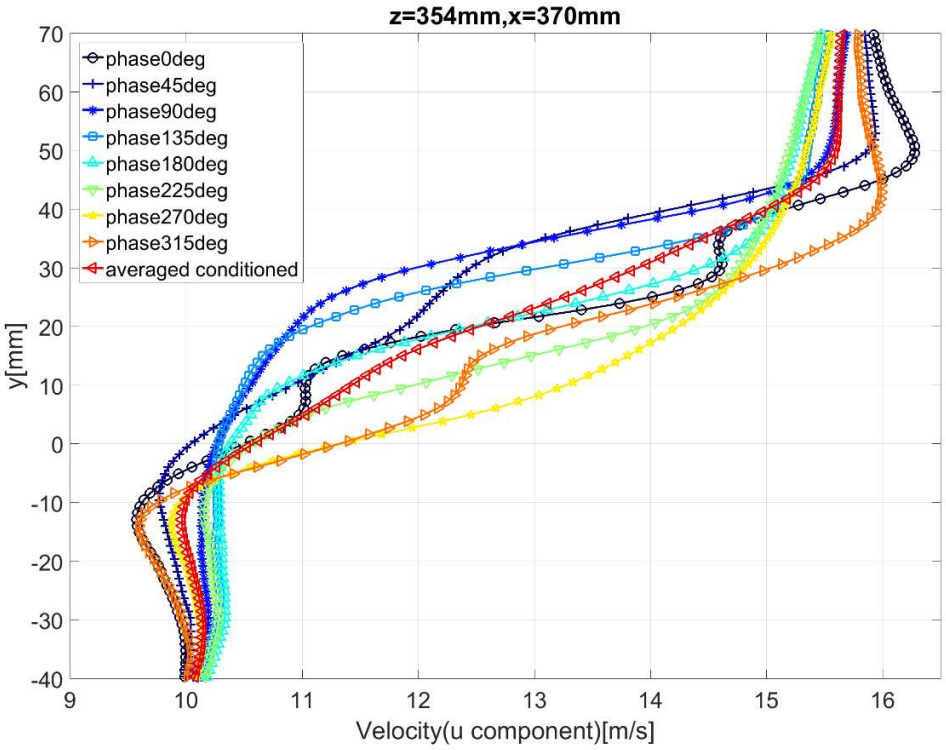

Figure 4.34: Phase-locked velocity profile at z=354mm and $x - x_{TE}$=370mm

Figures 4.34 to 4.37 focus on phase-locked velocity profiles for mixing layer flow with excitation frequency of 75 Hz. Figure 4.34 shows the phase-locked velocity profiles for fixed span and downstream positions which are z=354mm and $x - x_{TE}$=370mm. An observation can be made where multiple inflection points are present in the phase-locked velocity profiles. These inflection points are further highlighted for the velocity profile at phase of 0°, where 5 inflection points are present. Each inflection point corresponds to an instability mode present in the mixing layer flow as it travels at the specified coordinates. Further analysis will be discussed with Figure 4.35 when comparing the velocity profiles to vorticity field of the mixed layer flow.

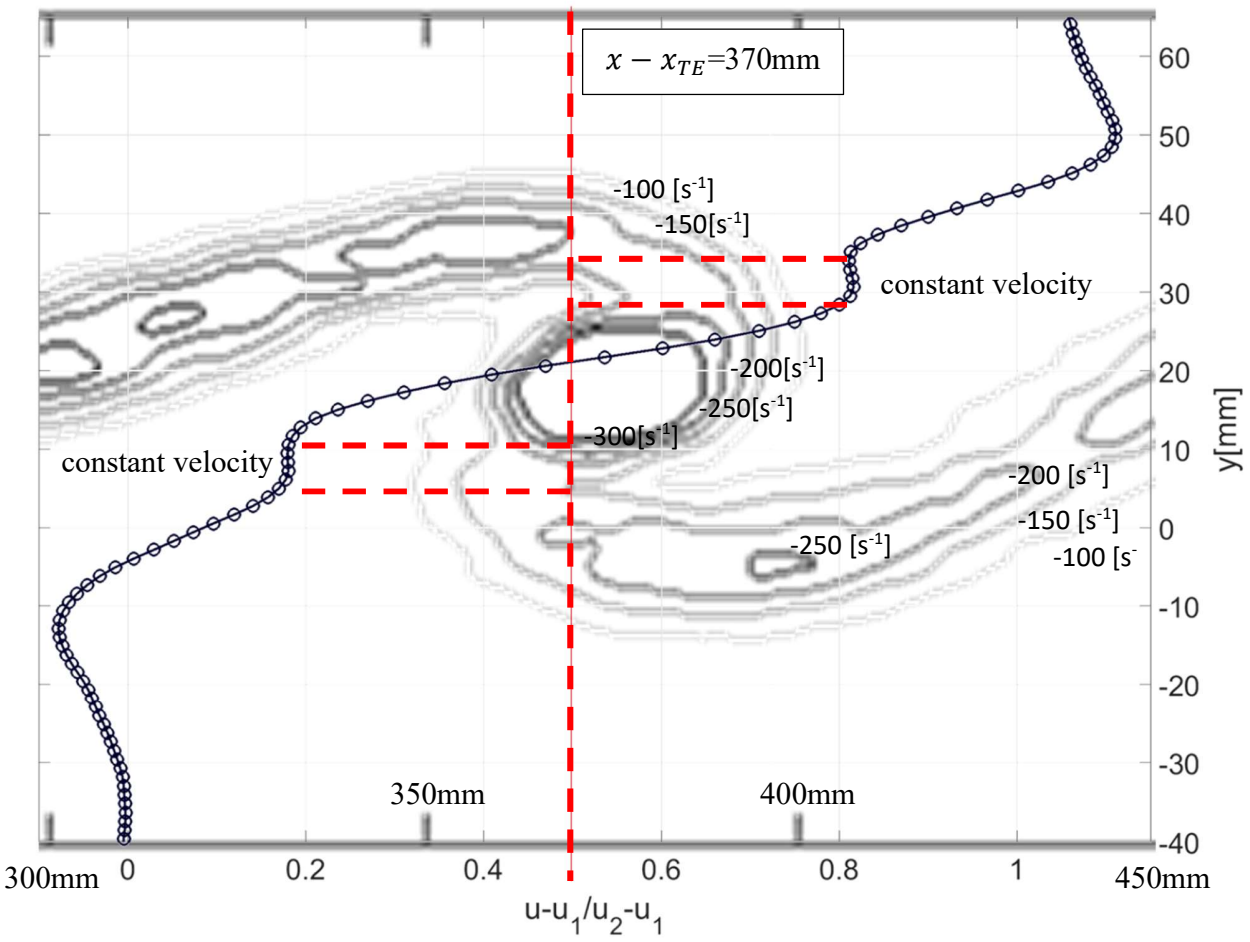

Figure 4.35: phase-locked velocity profile at phase 0deg and $x - x_{TE}$=370mm with the vorticity field

Figure 4.35 shows a 0° phase-locked velocity profile for fixed span and downstream location of z = 354 mm and $x - x_{TE}$=370 mm respectively. There are two instability modes at around vertical positions of y = 50 mm and -15 mm respectively. These instability modes are also overshoots where y = 50 mm represented as the overshoot for an increasing velocity while y= -15 mm is the overshoot for a decreasing velocity. These instability modes are induced by a combination of both potential vorticity and solid vorticity rotation. Furthermore, there are

additional two instability modes present at the upper side of the vortex from y=30mm to 50mm and lower side of the vortex from y=5mm to -15mm. Figure 4.35 shows multiple vorticity layers are present within the mixing layer flow. These vorticity fields are the very reason as to why the mixing layer flow with oscillation frequency of 75 Hz so complex. The final instability mode is located at the center of mixing layer flow.

This experiment demonstrates that an overamplified mixing layer flow undergoes two different regimes as it travels through space and time. One regime is where the mixing layer flow is affected by just vorticity layers that corresponds to a single instability mode which is also found for an excited flow at 50 Hz. Another regime is where the flow is affected by a combination of two wakes, two vorticity layers, and the vortex. As the flow undergoes these two distinct regimes, its vorticity and momentum thickness will vary in both time and space. That is why the velocity profiles in both downstream and trailing edge directions cannot attain self-similarities (Figures 4.5 and 4.6). This indicates that vorticity and momentum thickness profiles could not be used to determine where the flow deteriorates. In other words, if the flow is overamplified, then the behavior of the ensemble-averaged flow can neither be simplified by the vorticity nor momentum thickness due to the complexity of the mixing layer flow's interaction with time and space.

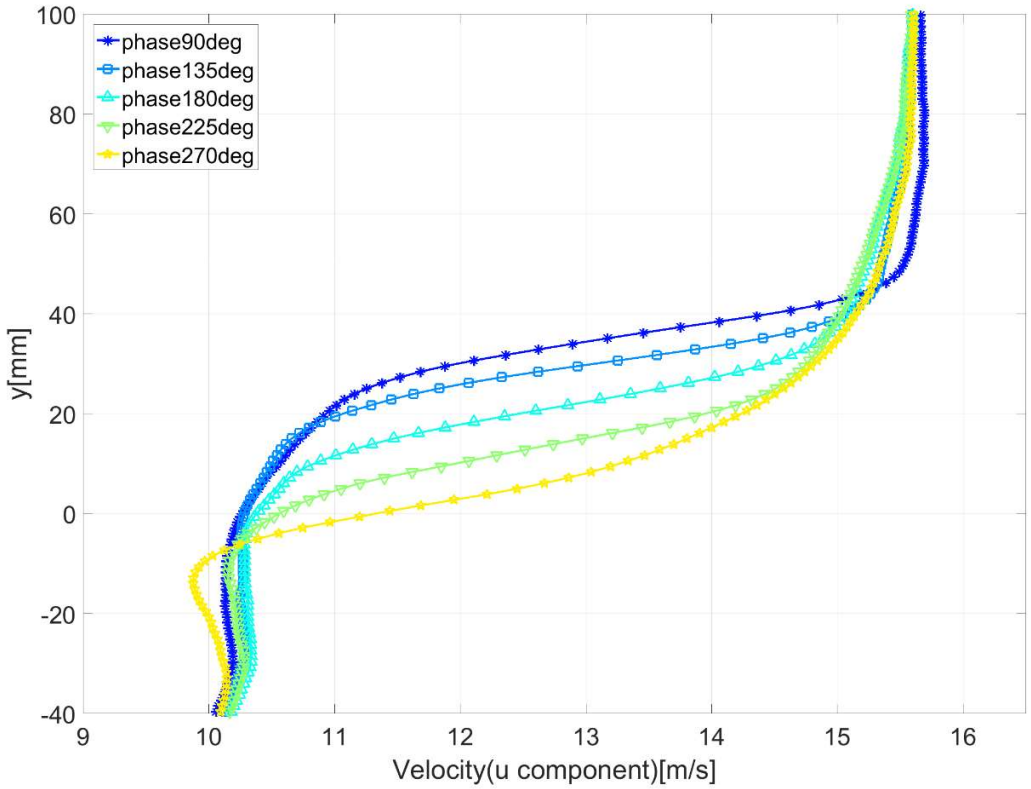

Figure 4.36: Phase-locked velocity profile with a single inflection point

Figure 4.36 shows the phase-locked velocity profile at 5 different phases for a fixed spanwise and downstream position of z=354mm and x=370mm respectively. The vorticity thickness of these phase-locked velocity profiles coincided with one another as they share the same maximum $\frac{du}{dy}$ value. The vorticity thickness does not develop within the range between phase 90° and phase 270°. On the other hand, the vorticity thickness between phase 315° and 45° varies in time. These are related with the nonlinearity that is caused by the overamplified flow.

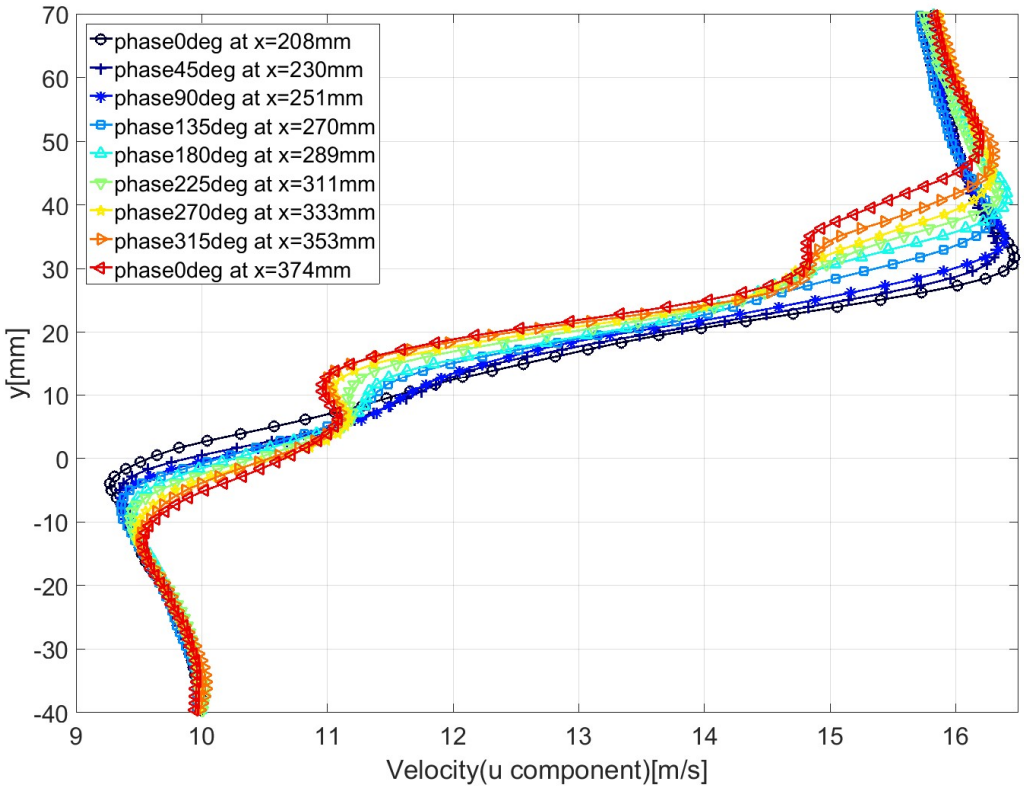

Figure 4.37: Phase-locked velocity profiles at the center of the vortex z=354mm

In order to investigate how the mixing layer grows spatially, Figure 4.37 shows the phase-locked velocity profiles at the center of the vortex. Figure 4.37 shows that the velocity profiles near the center of the trailing edge are affected by a combination of two wakes and the vortex itself. Furthermore, the velocity profile for phase 0° and $x - x_{TE}$=208mm shows that there are two inflection points generated by the wake and a single inflection point located at the center of the mixing layer. However, as the flow goes downstream, the number of inflection points increases. As seen in Figure 4.37, velocity profiles that are located at $x - x_{TE}$ >289 mm have five inflection points. In summary, an overamplified mixing layer flow will have two types of instability modes. These instability modes are generated from vortex and vorticity layers. The vortex generates instability modes on the flow regardless of space, while vorticity layers only generate instability modes as the flow continues downstream.

In a nutshell, studies of the mixing layer from both averaged random sampling and phase-locked sampling data agree that an overamplified flow field could not be normalized by just studying vorticity and momentum thickness.

4.3 Hotwire data

4.3.1 Power spectrum

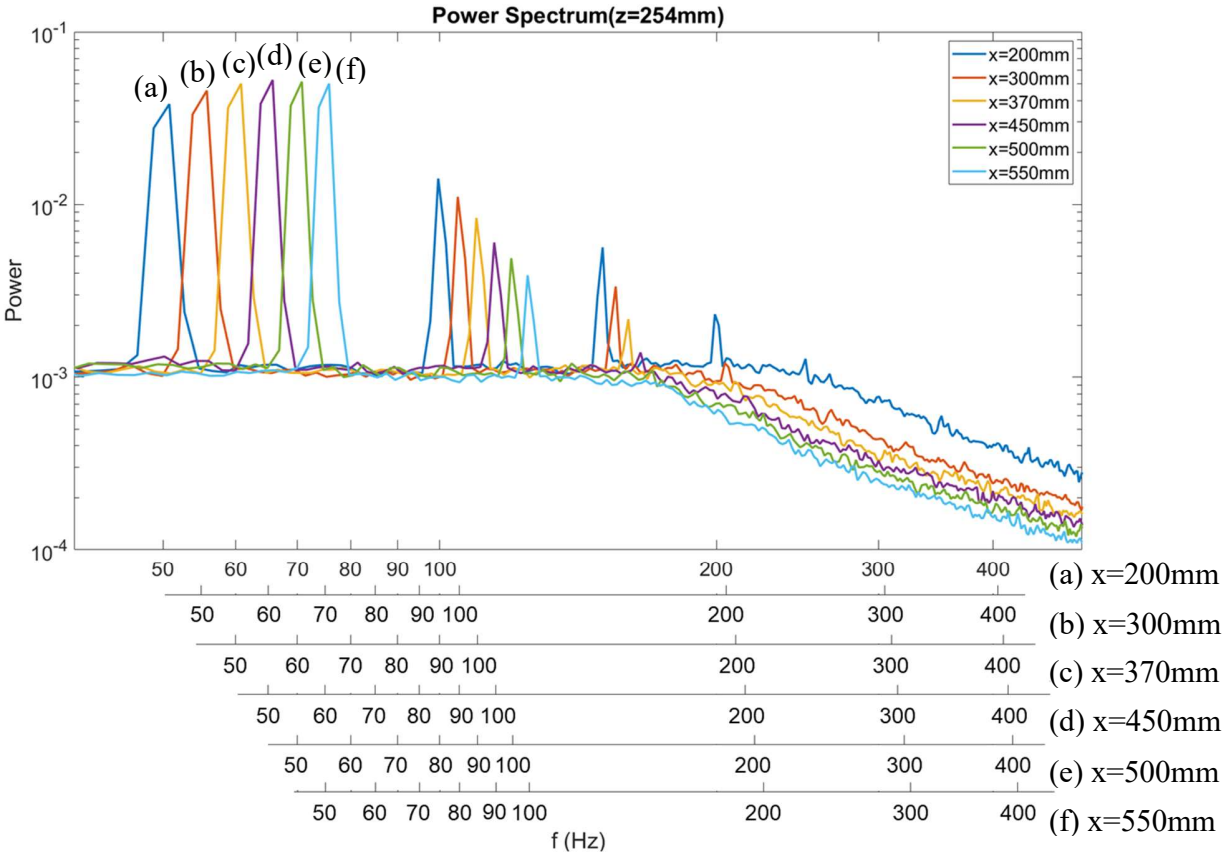

Figure 4.38: Power spectrum with forcing frequency of 50Hz at z=254mm (a) x=200mm (b) x=300m (c) x=370mm (d) x=450mm (e) x=500mm (f) x=550mm

Figure 4.38 shows the power spectrum plots of mixing layer at span location z = 254 mm and excitation frequency f = 50 Hz using a single hotwire. In order to compare the power spectrum plots for each location downstream, a horizontal axis offset of 5 Hz increment should be applied to each corresponding plot. When comparing the intensities of the first peaks at 50 Hz of all locations, the maximum intensity occurs between $x - x_{TE}$=450mm and 500mm. This location coincides well with the saturation point obtained from the vorticity thickness profile (Figure 4.2a). This data verifies that the flow expands until it reaches $x - x_{TE}$=450mm from which is transforms into a type Region II mixing flow. Across all power spectrum plots downstream, a general trend is noted whereby a forcing frequency of 50 Hz implements the largest amount of power into mixing layer.

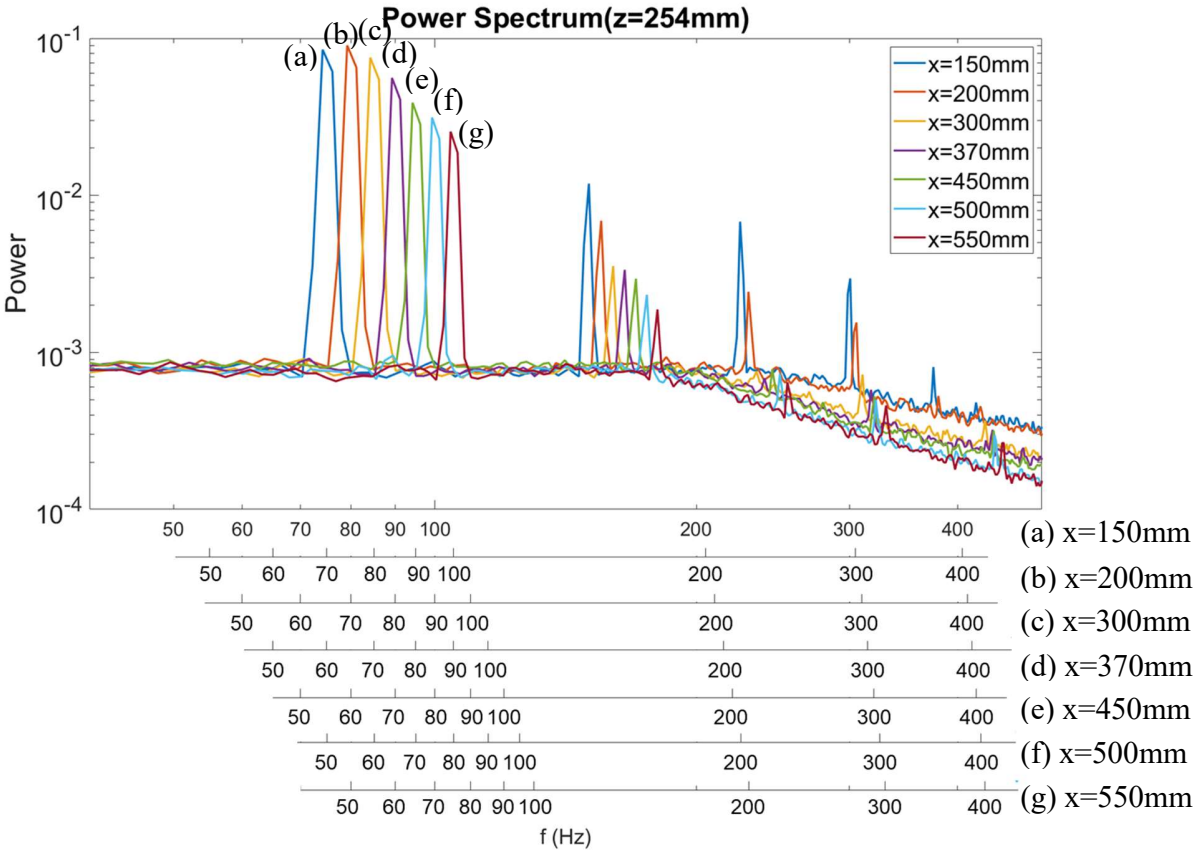

Figure 4.39: Power spectrum with forcing frequency of 75Hz at z=254mm (a) x=150mm (b) x=200mm (c) x=300m (d) x=370mm (e) x=450mm (f) x=500mm (g) x=550mm

Figure 4.39 shows the power spectrum plots of mixing layer at spanwise location z = 254 mm and excitation frequency f = 75 Hz using a single hotwire. When comparing the intensities of the first peaks at 75 Hz of all locations, the maximum intensity occurs at around $x - x_{TE}$=200mm. This location coincides well with the vertical vortex location obtained from the vorticity fields (Figure 4.25). This spectrum also reveals that the decaying rate decreases for higher harmonic frequency. Namely, these harmonic frequencies cause the distorted mean velocity profiles.

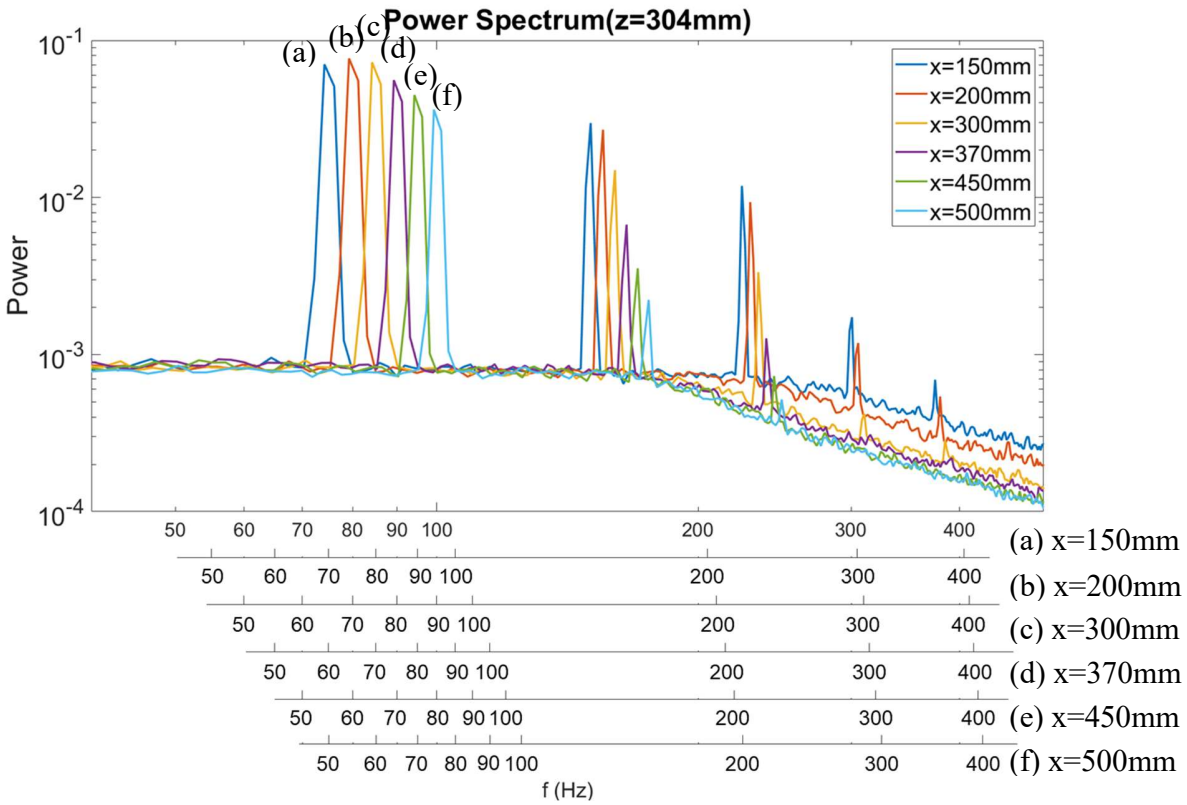

Figure 4.40: Power spectrum with forcing frequency of 75Hz at z=304mm (a) x=150mm (b) x=200mm (c) x=300m (d) x=370mm (e) x=450mm (f) x=500mm

Figure 4.40 shows the power spectrum plots of mixing layer at span location z = 304 mm and excitation frequency f = 75 Hz using a single hotwire. When comparing the intensities of the first peaks at 75 Hz of all locations, the maximum intensity occurs between $x - x_{TE}$=200mm and 300mm. This location coincides well with the vertical vortex location obtained from the vorticity fields (Figure 4.26). This spectrum also reveals that the decaying rate of the higher harmonic frequency is slow. As a result of the higher harmonic frequencies, there occur several instability modes.

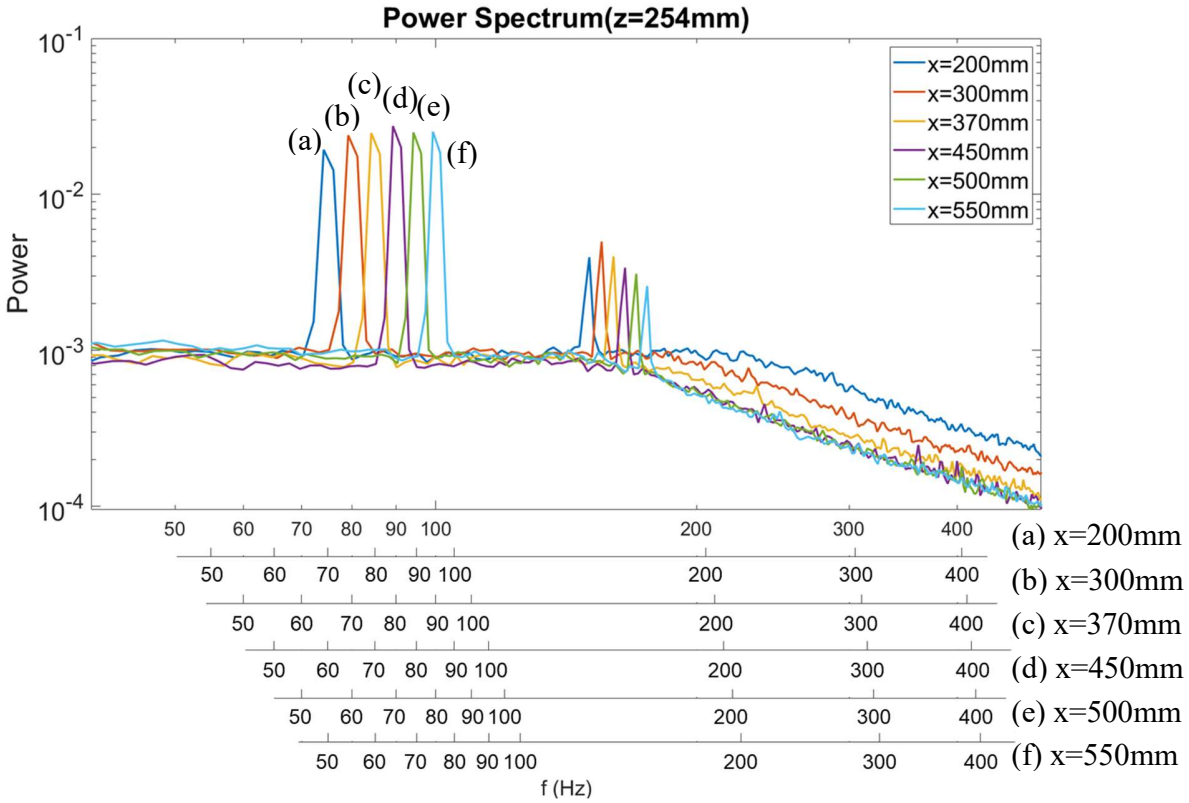

Figure 4.41: Power spectrum with forcing frequency of 75Hz and quarter amplitude at z=254mm (a) x=150mm (b) x=200mm (c) x=300m (d) x=370mm (e) x=450mm (f) x=500mm

Figure 4.41 shows the power spectrum plots of mixing layer at spanwise location z = 254 mm, excitation frequency f = 75 Hz, and quarter amplitude using a single hotwire. When comparing the intensities of the first peaks at 75 Hz of all locations, the maximum intensity occurs at $x - x_{TE}$=450mm ($R(x - x_{TE})/\lambda_x = 0.62$). The most significant feature is that there are no spikes of the higher harmonic frequencies.

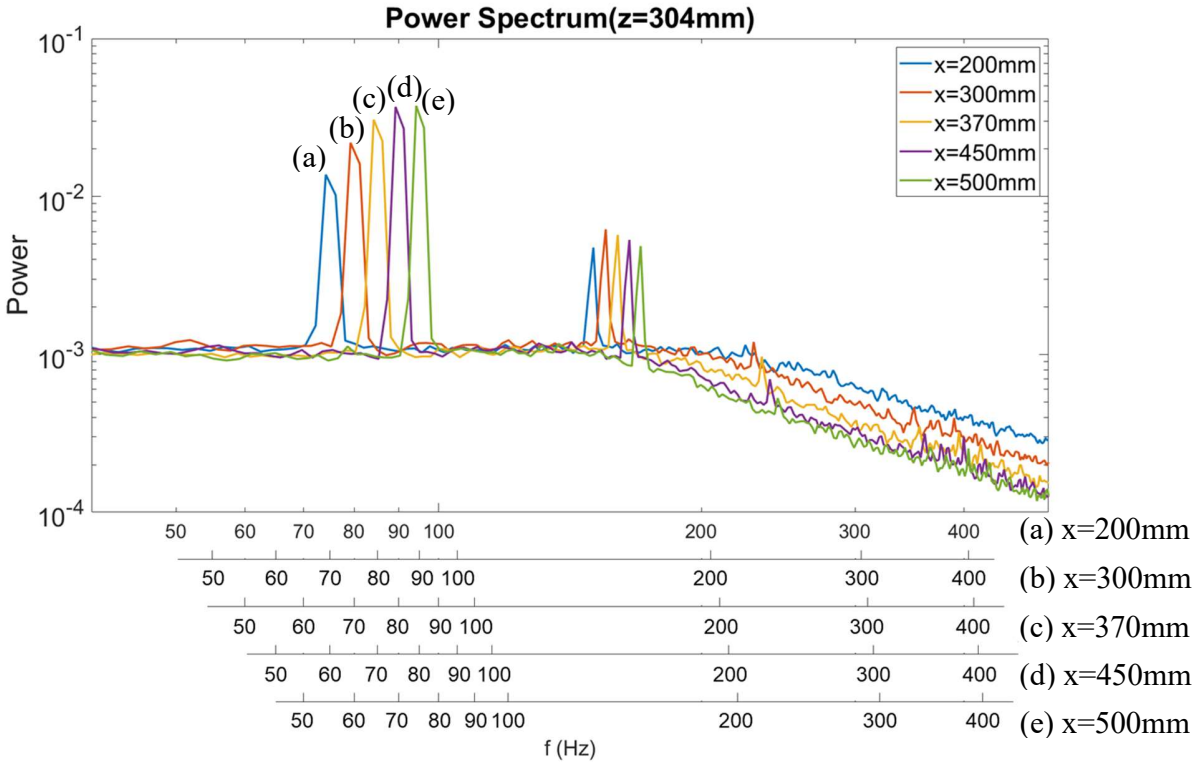

Figure 4.42: Power spectrum with forcing frequency of 75Hz and quarter amplitude at z=304mm (a) x=150mm (b) x=200mm (c) x=300m (d) x=370mm (e) z=404mm

Figure 4.42 shows the power spectrum plots of mixing layer at span location z = 304 mm, excitation frequency f = 75 Hz, and quarter amplitude using a single hotwire. When comparing the intensities of the first peaks at 75 Hz of all locations, the maximum intensity can be seen at $x - x_{TE}$=450mm ($R(x - x_{TE})/\lambda_x = 0.62$). The data also reveals that there are no spikes of the higher harmonic frequencies.

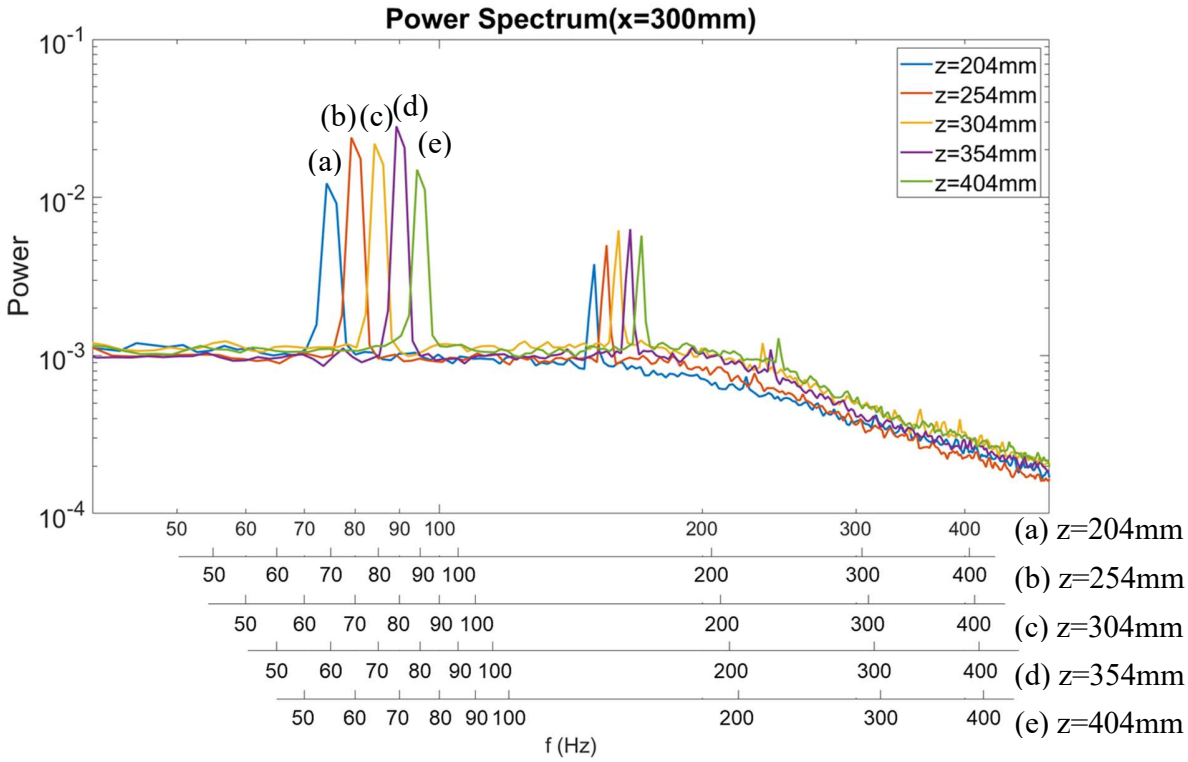

Figure 4.43: Power spectrum with forcing frequency of 75Hz and quarter amplitude in the direction parallel to the trailing edge at x=300mm (a) z=204mm (b) z=254mm (c) z=304mm (d) z=354mm (e) z=404mm

Figure 4.43 shows the power spectrum plots of mixing layer at streamwise location x = 300 mm, excitation frequency f = 75 Hz, and quarter amplitude using a single hotwire. When comparing the intensities of the first peaks at 75 Hz of all locations, the maximum intensity occurs at z=354mm. Even if the flow is limitedly amplified, the spectrum shows that the spanwise maximum intensities are not uniform.

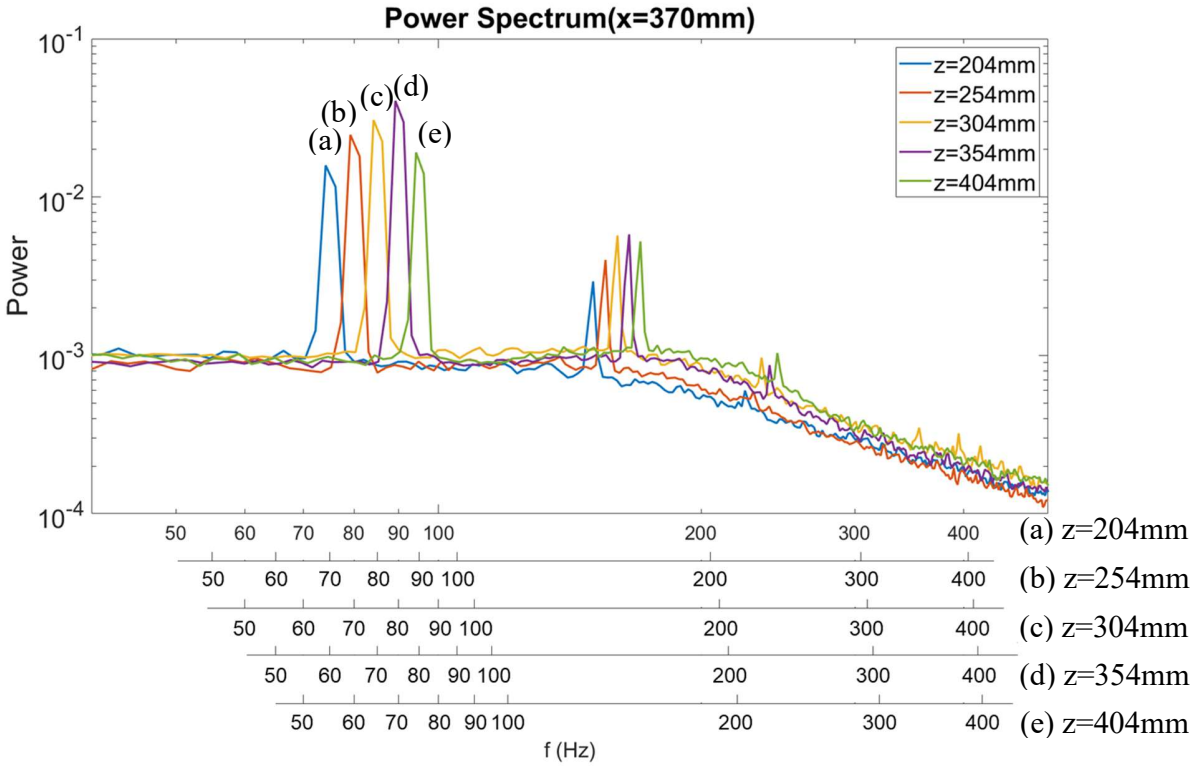

Figure 4.44: Power spectrum with forcing frequency of 75Hz and quarter amplitude in the direction parallel to the trailing edge at x=370mm (a) z=204mm (b) z=254mm (c) z=304mm (d) z=354mm (e) z=404mm

Figure 4.44 shows the power spectrum plots of mixing layer at streamwise location x = 370 mm, excitation frequency f = 75 Hz, and quarter amplitude using a single hotwire. When comparing the intensities of the first peaks at 75 Hz of all locations, the maximum intensity occurs at z=354mm. This location coincides with that in the spectrum at x=300mm (Figure 4.43).

5 CONCLUSIONS

A combination of a swept-back wing and a screen spanning half of the wind tunnel test section generates an oblique turbulent mixing layer of a prescribed velocity ratio that is determined by the solidity or the number of the screens used. In the current experiment, the velocity ratio between the two streams is 0.6. This is a simpler arrangement than the Λ shaped trailing edge of a splitter plate that attempted to emulate the flow emanating from a chevron nozzle. However, there were some complicated phenomena and this experiment demonstrated some of their important features. One is that the mean flow with a proper amplitude of the oscillations at the trailing edge can be decomposed into a non-divergent component parallel to the trailing edge and divergent component normal to it. This provides a good perspective toward the understanding of the skewed turbulent mixing layer.

On the other hand, this experiment with the forcing frequency of 75Hz demonstrated that the input amplitude of the imposed oscillations was too high, resulting in a premature rollup of the vorticity sheet separating the two streams. Consequently, an instantaneous velocity map of the flow over a distance that exceeded a single wavelength of the imposed perturbation revealed a possibility of numerous nonlinear instabilities. The flow spread out with increasing distance from the trailing edge, but the growth rate depended on time and space. Thus, there was not a single length scale even when one considered the vorticity sheet that characterized the flow over a fraction of the forcing cycle from the large rolled up eddy that prevailed over the other part of the forcing cycle. This is because the controlled instabilities evoked by the forcing evolved with distance from the origin of the flow (i.e. these were spatial instabilities).

The boundary layer independence principle cannot be applied to the distorted sheet determining the center of the flow due to the inadequacy of the boundary layer approximation that neglects pressure variations across the boundary layer. This is best seen in the case of 75Hz forced mixing layer where the high-speed free stream entrains fluid from the low speed side that is bending the streamlines toward it and creating a pressure gradient that is outside the boundary layer approximation. That is why the conventional vorticity thickness or momentum thickness based on the boundary layer independence principle cannot be applied to the flow which is excessively amplified.

For the future work, there are some ideas that I would like to suggest for the improvement of the experimental quality. The following idea could be tested.

1. Smaller velocity ratio (U_1/U_2) can be used. This idea gives a larger normalized distance so that the plateau may be confirmed clearly in the momentum thickness profile with the forcing frequency of 50Hz
2. Larger swept-back angle can be one of the options. This will give the same effect as the first one and be helpful to distinguish the saturation point which divides the flow into Region I and Region II.
3. I am considering the option of using a larger test section. This would aid to reduce the wall effect especially for the center location.
4. The way the test model is constructed could be also changed. The y_{05} profile variation in the z-direction will be improved by changing the aspect ratio of the test model. The further uniform flow in the z-direction could be expected in the future work.

APPENDIX A - MISCELLANEOUS DATA

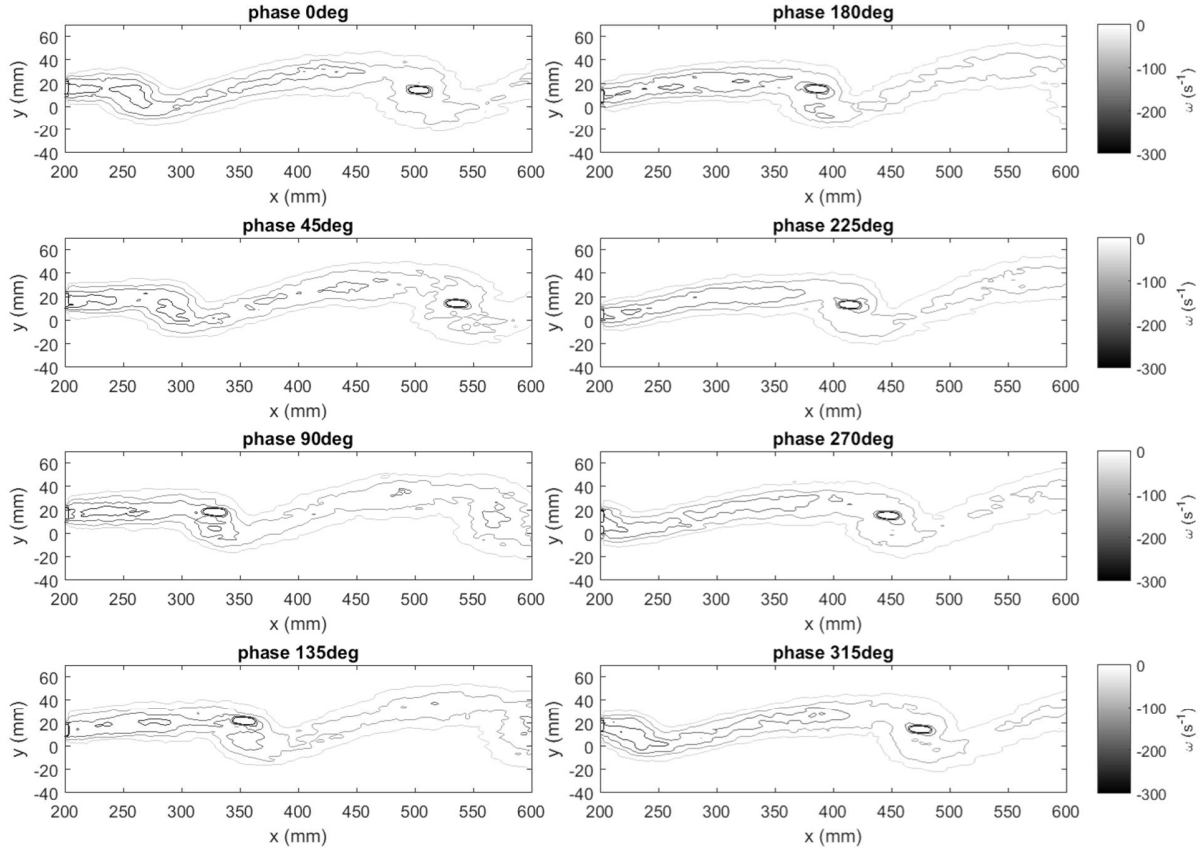

Figure A.1: Phase-locked vorticity fields at z=279mm with forcing frequency of f=50Hz

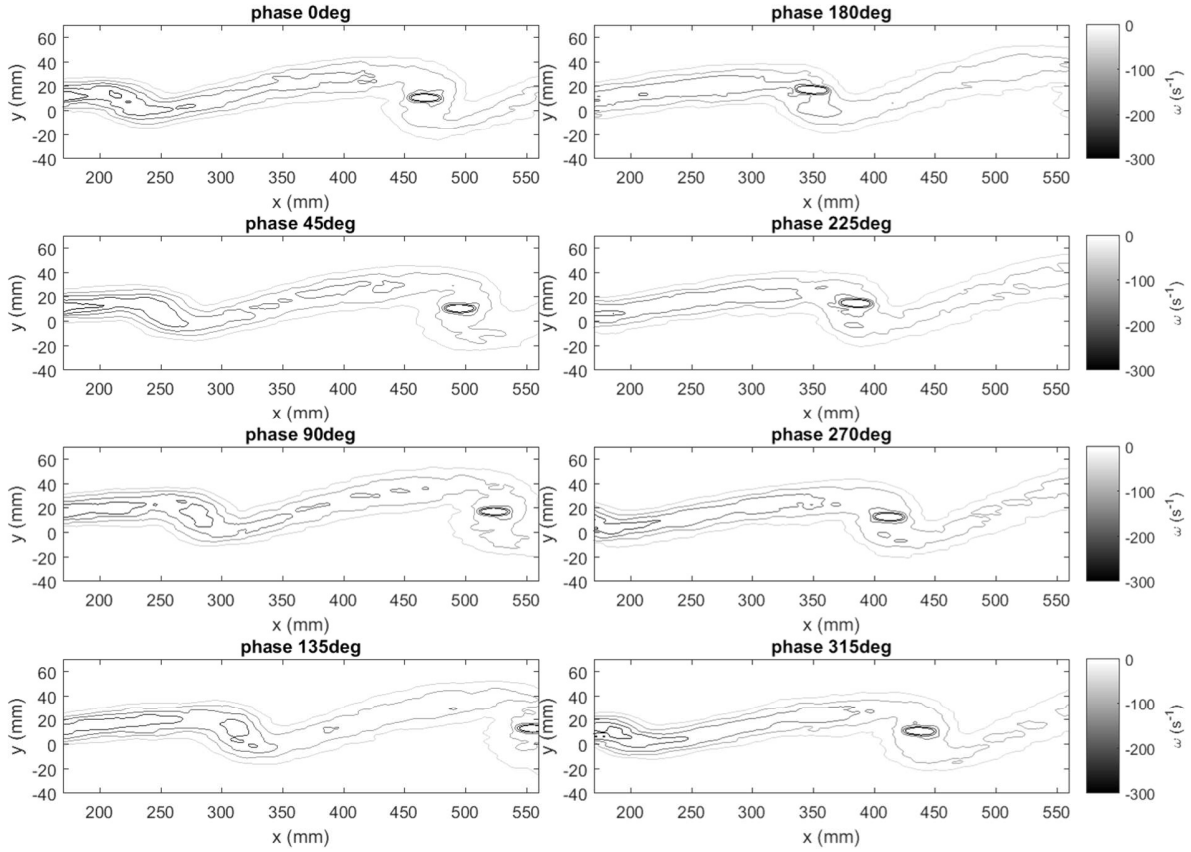

Figure A.2: Phase-locked vorticity fields at z=329mm with forcing frequency of f=50Hz

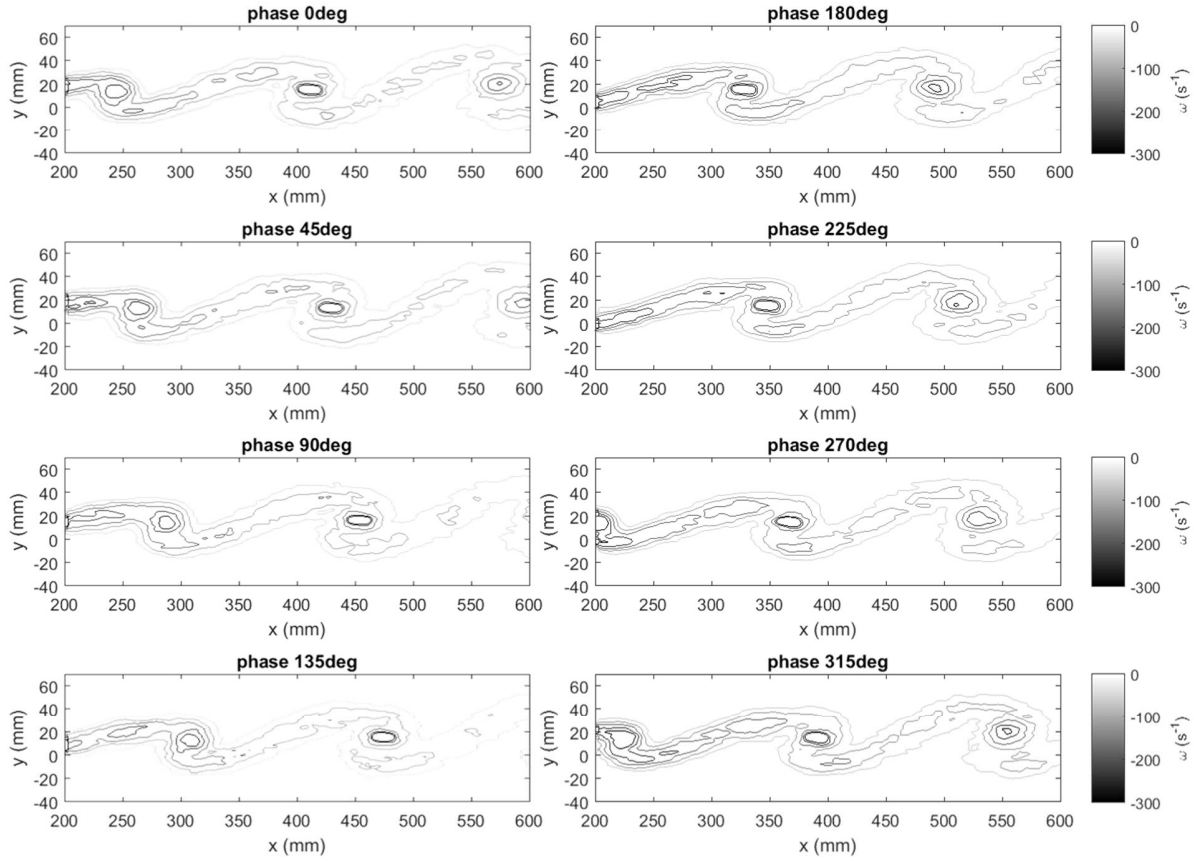

Figure A.3: Phase-locked vorticity fields at z=279mm with forcing frequency of f=75Hz

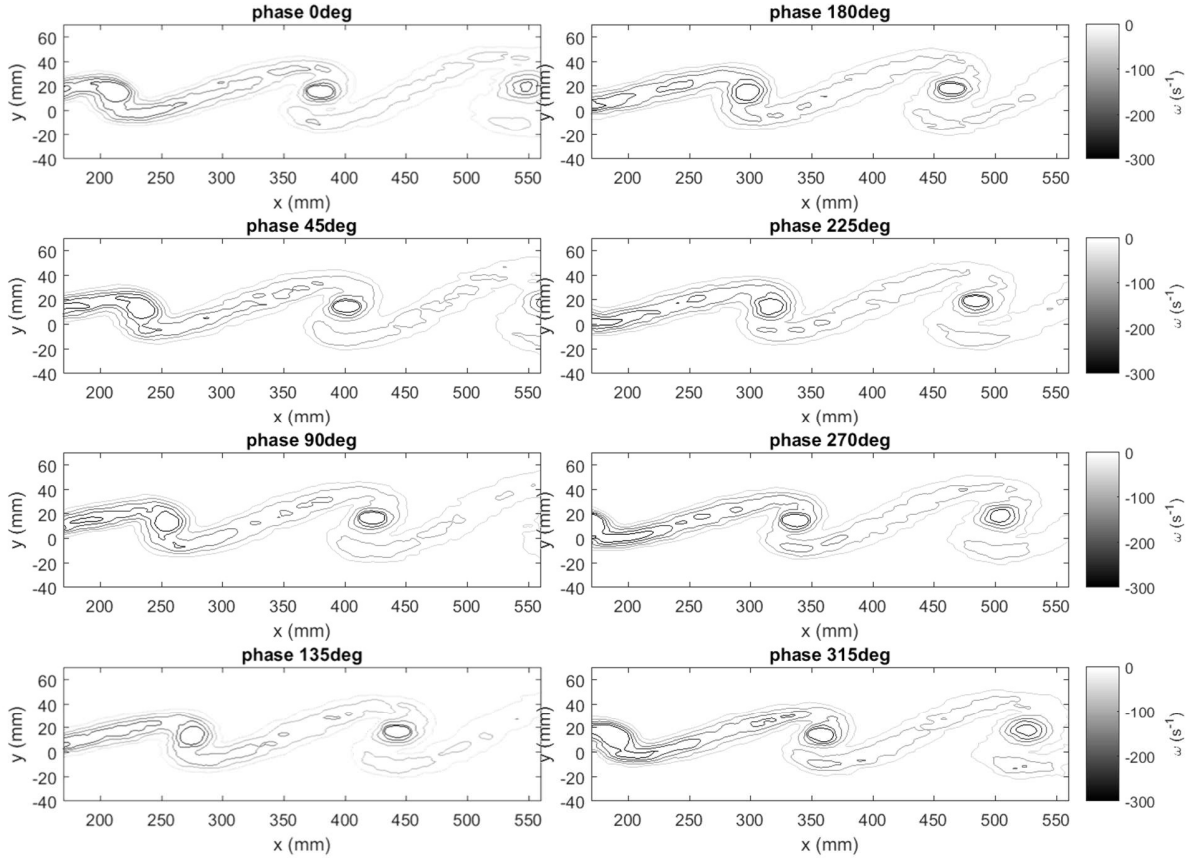

Figure A.4: Phase-locked vorticity fields at z=329mm with forcing frequency of f=75Hz

APPENDIX B – GOVERNING EQUATIONS USING TRIPLE DECOMPOSITION

Considering a flow holding coherent structures, an instantaneous variable, f, can be decomposed into three components: the time-independent component, $\bar{f}$, the coherent component, f_c, and the random component, f_r.

$$f = \bar{f} + f_c + f_r$$

and

$$\langle f \rangle = \bar{f} + f_c$$

where ⟨f⟩ is the phase average which is the ensemble average of points having the same phase with respect to the oscillator. This is applicable to the many fields such as velocity component and pressure component. Let u_i be the instantaneous velocity component for $i = 1, 2, 3$ corresponding to the velocity component in the x, y, and z-direction respectively. The following application example is the triple decomposition for the velocity field.

$$u_i = \overline{u_\imath} + u_{ci} + u_{ri}$$

u_i: instantaneous velocity field with forcing at a given frequency

$\overline{u_\imath}$: mean (time-averaged) velocity field with forcing at a given frequency

$\overline{u_\imath} + u_{ci}$: mean phase-locked velocity field with forcing at a given frequency

The momentum equation is

$$\frac{\overline{D}}{Dt}\overline{u_\imath} = -\frac{\partial \bar{p}}{\partial x_i} + \frac{1}{Re}\frac{\partial^2 \overline{u_\imath}}{\partial {x_j}^2} + \frac{\partial}{\partial x_j}\left(-\overline{u_{c\imath} u_{cJ}} - \overline{u_{r\imath} u_{rJ}}\right)$$

$$\frac{\overline{D}}{Dt}u_{ci} = -\frac{\partial p_c}{\partial x_i} + \frac{1}{Re}\frac{\partial^2 u_{ci}}{\partial {x_j}^2} - \frac{\partial}{\partial x_j}\left(\overline{u_\imath} u_{cj}\right) + \frac{\partial}{\partial x_j}\left(\overline{u_{c\imath} u_{cJ}} - u_{ci} u_{cj}\right) + \frac{\partial}{\partial x_j}\left(\overline{u_{r\imath} u_{rJ}} - \langle u_{ri} u_{rj} \rangle\right)$$

$$\frac{\overline{D}}{Dt}u_{ri} = -\frac{\partial p_r}{\partial x_i} + \frac{1}{Re}\frac{\partial^2 u_{ri}}{\partial {x_j}^2} - \frac{\partial}{\partial x_j}\left(u_{ci} u_{ri} + \overline{u_\imath} u_{rj} + u_{ci} u_{rj}\right) - \frac{\partial}{\partial x_j}\left(\overline{u_{r\imath} u_{rJ}} - \langle u_{ri} u_{rj} \rangle\right)$$

where $\overline{D}/Dt = \partial/\partial t + \overline{u_j}\partial/\partial x_j$ and x_i i=1,2,3, represents the coordinates in the x, y, z-direction, respectively.

The average kinetic energy per unit mass at a point is

$$\frac{1}{2}\overline{u_\imath u_\imath} = \frac{1}{2}\overline{u_\imath}\,\overline{u_\imath} + \frac{1}{2}\overline{u_{c\imath} u_{c\imath}} + \frac{1}{2}\overline{u_{r\imath} u_{r\imath}}$$

Equations for the triple decomposed total kinetic energy can be obtained by multiplying the three momentum equations for the time-independent, coherent, and random components by $\overline{u_\iota}$, u_{ci}, u_{ri}, respectively.

$$\frac{\overline{D}}{Dt}\left(\frac{1}{2}\overline{u_\iota}\overline{u_\iota}\right) = -\frac{\partial \overline{p u_\iota}}{\partial x_i} - \left(-\overline{u_{c\iota}u_{cJ}}\frac{\partial \overline{u_\iota}}{\partial x_j}\right) - \left(-\overline{u_{r\iota}u_{rJ}}\frac{\partial \overline{u_\iota}}{\partial x_j}\right) - \frac{\partial}{\partial x_j}\left[\overline{u_\iota}\left(\overline{u_{c\iota}u_{cJ}} + \overline{u_{r\iota}u_{rJ}}\right)\right]$$
$$-\frac{1}{Re}\frac{\partial}{\partial x_j}\left[\overline{u_\iota}\left(\frac{\partial \overline{u_\iota}}{\partial x_j} + \frac{\partial \overline{u_J}}{\partial x_i}\right)\right] - \frac{1}{2Re}\left(\frac{\partial \overline{u_\iota}}{\partial x_j} + \frac{\partial \overline{u_J}}{\partial x_i}\right)\left(\frac{\partial \overline{u_\iota}}{\partial x_j} + \frac{\partial \overline{u_J}}{\partial x_i}\right)$$

$$\frac{\overline{D}}{Dt}\left(\frac{1}{2}\overline{u_{c\iota}u_{c\iota}}\right) = -\frac{\partial}{\partial x_i}\overline{\left[u_{cJ}\left(p_c + \frac{1}{2}u_{c\iota}u_{c\iota}\right)\right]} + \left(-\overline{u_{c\iota}u_{cJ}}\frac{\partial \overline{u_\iota}}{\partial x_j}\right) - \overline{\left(-\langle u_{r\iota}u_{rJ}\rangle\frac{\partial u_{c\iota}}{\partial x_J}\right)}$$
$$-\frac{\partial}{\partial x_j}\left[\overline{u_{c\iota}\langle u_{r\iota}u_{rJ}\rangle}\right] + \frac{1}{Re}\frac{\partial}{\partial x_j}\overline{\left[u_{c\iota}\left(\frac{\partial u_{c\iota}}{\partial x_J} + \frac{\partial u_{cJ}}{\partial x_\iota}\right)\right]}$$
$$-\frac{1}{2Re}\overline{\left(\frac{\partial u_{c\iota}}{\partial x_J} + \frac{\partial u_{cJ}}{\partial x_\iota}\right)\left(\frac{\partial u_{c\iota}}{\partial x_J} + \frac{\partial u_{cJ}}{\partial x_\iota}\right)}$$

$$\frac{\overline{D}}{Dt}\left(\frac{1}{2}\overline{u_{r\iota}u_{r\iota}}\right) = -\frac{\partial}{\partial x_j}\overline{\left[u_{rJ}\left(p_r + \frac{1}{2}u_{r\iota}u_{r\iota}\right)\right]} + \left(-\overline{u_{r\iota}u_{rJ}}\frac{\partial \overline{u_\iota}}{\partial x_j}\right) + \overline{\left(-\langle u_{r\iota}u_{rJ}\rangle\frac{\partial u_{c\iota}}{\partial x_J}\right)}$$
$$-\overline{u_{cJ}\frac{\partial}{\partial x_J}\langle\frac{1}{2}u_{r\iota}u_{r\iota}\rangle} + \frac{1}{Re}\frac{\partial}{\partial x_j}\overline{\left[u_{r\iota}\left(\frac{\partial u_{r\iota}}{\partial x_J} + \frac{\partial u_{rJ}}{\partial x_\iota}\right)\right]}$$
$$-\frac{1}{2Re}\overline{\left(\frac{\partial u_{r\iota}}{\partial x_J} + \frac{\partial u_{rJ}}{\partial x_\iota}\right)\left(\frac{\partial u_{r\iota}}{\partial x_J} + \frac{\partial u_{rJ}}{\partial x_\iota}\right)}$$

$$P_1 = -\overline{u_{c\iota}u_{cJ}}\frac{\partial \overline{u_\iota}}{\partial x_j}$$

$$P_2 = -\overline{u_{r\iota}u_{rJ}}\frac{\partial \overline{u_\iota}}{\partial x_j}$$

$$P_3 = \overline{(-\langle u_{r\iota}u_{rJ}\rangle)\frac{\partial u_{c\iota}}{\partial x_J}}$$

These three terms can be seen as common terms in two equations. This shows that the energy transfer occurs between the mean fields to the coherent fields, from the mean fields to the random fields, and from the coherent fields to the random fields.

Energy extracted from mean: P_1

Energy transfer to random: P_3

Net coherent energy production: $P_1 - P_3$

REFERENCES

[1] N. H. Saiyed, K. L. Mikkelsen and J. E. Bridges, "Acoustics and Thrust of Quiet Separate-Flow High-Bypass-Ratio Nozzles," AIAA JOURNAL, vol. 41, No. 3, 2003.

[2] LOCKHEED MARTIN (2019, Oct 25), Retrieved from http://www.codeonemagazine.com/images/media/2010_001AFF_091119_0012_SM_12678 28237_2127.jpg

[3] D. Oster and I. Wygnanski, “The forced mixing layer between parallel streams,” Journal of Fluid Mechanics, vol. 123, pp. 9-130, 1982.

[4] I. Wygnanski and R. Petersen, "Coherent Motion in Excited Free Shear Layers," AIAA Journal, vol. 25, no. 2, pp. 201-213, 1987.

[5] G. Brown and A. Roshko, "On density effects and large structure in turbulent mixing layers,” Journal of Fluid Mechanics, vol. 64, pp. 775-816, 1974.

[6] I. Weisbrot and I. Wygnanski, "On coherent structures in a highly excited mixing layer,” Journal of Fluid Mechanics, vol. 195, p. 137–159, 1988.

[7] D. Oster, I. Wygnanski, B. Dziomba, and H. Fiedler, "On the Effect of Initial Conditions on the Two-Dimensional Turbulent Mixing Layer,” Lecture Notes in Physics, vol. 75, pp. 48-65, 1978.

[8] A. Michalke, "On spatially growing disturbances in an inviscid shear layer,” Journal of Fluid Mechanics, vol. 23, pp. 521-544, 1965.

[9] H. Schlichting and K. Gersten, Boundary-Layer Theory, 8th Edition, Springer, 2001.

[10] B. Zakharin, K. E. and I Wygnanski, “On a Turbulent Mixing Layer Created Downstream of a “Λ” Notch Simulating One Wavelength of a Chevron Nozzle,” Journal of Flow Turbulence & Combustion, vol. 83, pp. 371-388, 2009.

[11] E. Suehiro, On Controlling the Flow in a Turbulent Mixing Layer Created Downstream of a “Λ” Notch (Dissertation), University of Arizona, Tucson, 2017.

[12] L. P. Bernal and A. Roshko, "Streamwise Vortex Structure in Plane Mixing Layers," Journal of Fluid Mechanics Vol 170, pp. 499-525, 1986.

[13] W. Schoppa, F. Hussain and R. W. Metcalfe, "A New Mechanism of Small-Scale Transition in a Plane Mixing Layer: Core Dynamics of Spacewise Vortices," Journal of Fluid Mechanics, vol. 298, pp. 23-80, 1995.

[14] E. Kit, I. Wygnanski, D. Friedman, O. Krivonosova and D. Zhilenko, "On the Periodically Excited, Plane Turbulent Mixing Layer Emanating from a Jagged Partition," Journal of Fluid Mechanics, vol. 589, pp. 479-507, 2007.

[15] I. Wygnanski and I. Weisbrot, “On the pairing process in an excited plane turbulent mixing layer,” Journal of Fluid Mechanics, vol. 195, pp. 161-173, 1988.

[16] J. B. Barlow, W. H. Rae, and A. Pope, Low-Speed Wind Tunnel Testing 3rd Edition, John Wiley and Sons, Inc, 1999.

[17] I. Wygnanski, D. Oster, H. Fiedler and B. Dziomba, "On the Perseverance of a Quasi-two-dimensional Eddy-Structure in a Turbulent Mixing Layer," Journal of Fluid Mechanics, vol. 93, pp. 325-335, 1979.

[18] I. Wygnanski, P. Tewes, H. Kurz, L. Taubert and C. and Chen, "The Application of Boundary Layer Independence Principle to Three-dimensional Turbulent Mixing Layers," Journal of Fluid Mechanics, vol. 675, p. 336–346, 2011.

[19] C. M. Ho and P. Huerre, "Perturbed Free Shear Layers," Annual Review in Fluid Mechanics, vol. 16, pp. 365-424, 1984.